3D diffusion of water in melt inclusion-bearing olivine phenocrysts

Euan J. F. Mutch[1,2,3,4], Megan E. Newcombe[1], John F. Rudge[5]

[1]Department of Geology, University of Maryland, 8000 Regents Dr, College Park, Maryland, 20742, United States
[2]Lamont Doherty Earth Observatory, Columbia University, 61 Route 9W, Palisades, New York, 10964, United States
[3]Earth Observatory of Singapore, Nanyang Technological University, 50 Nanyang Avenue, Block N2-01A-15, 639798, Singapore
[4]Asian School of the Environment, Nanyang Technological University, 50 Nanyang Avenue, Block N2-01C-63, 639798, Singapore
[5]Bullard Laboratories, Department of Earth Sciences, University of Cambridge, Cambridge, UK

Corresponding Author: Euan J. F. Mutch (euan.mutch@ntu.edu.sg)

3D diffusion of water in melt inclusion-bearing olivine phenocrysts

Euan J. F. Mutch[1,2,3,4]**, Megan E. Newcombe**[1]**, John F. Rudge**[5]

[1]Department of Geology, University of Maryland, 8000 Regents Dr, College Park, Maryland, 20742, United States

[2]Lamont Doherty Earth Observatory, Columbia University, 61 Route 9W, Palisades, New York, 10964, United States

[3]Earth Observatory of Singapore, Nanyang Technological University, 50 Nanyang Avenue, Block N2-01A-15, 639798, Singapore

[4]Asian School of the Environment, Nanyang Technological University, 50 Nanyang Avenue, Block N2-01C-63, 639798, Singapore

[5]Bullard Laboratories, Department of Earth Sciences, University of Cambridge, Cambridge, UK

Key Points:

- New 3D multiphase finite element diffusion model and anisotropic analytical solution for water loss from melt inclusions.
- 1D and 2D numerical models underestimate magma decompression rates compared to 3D models. The analytical solution performs well.
- Shielding effect from multiple melt inclusions may limit water loss.

Corresponding author: Euan J. F. Mutch, `euan.mutch@ntu.edu.sg`

Abstract

Olivine-hosted melt inclusions are an important archive of pre-eruptive processes such as magma storage, mixing and subsequent ascent through the crust. However, this record can be modified by post entrapment diffusion of H^+ through the olivine lattice. Existing studies often use spherical or 1D models to track melt inclusion dehydration that fail to account for complexities in geometry, diffusive anisotropy and sectioning effects. Here we develop a finite element 3D multiphase diffusion model for the dehydration of olivine-hosted melt inclusions that includes natural crystal geometries and multiple melt inclusions. We use our 3D model to test the reliability of simplified analytical and numerical models (1D and 2D) using magma ascent conditions from the 1977 eruption of Seguam volcano, Alaska. We find that 1D models underestimate melt inclusion water loss, typically by 30 %, and thus underestimate magma decompression rates, by up to a factor of 5, when compared to the 3D models. An anisotropic analytical solution that we present performs well and recovers decompression rates within a factor of 2, in the situations in which it is valid. 3D models that include multiple melt inclusions show that inclusions can shield each other and reduce the amount of water loss upon ascent. This shielding effect depends on decompression rate, melt inclusion size, and crystallographic direction. Our modelling approach shows that factors such as 3D crystal geometry and melt inclusion configuration can play an important role in constraining accurate decompression rates and recovering water contents in natural magmatic systems.

Plain Language Summary

The water content of olivine-hosted melt inclusions can reveal important information about the generation and storage of magma beneath basaltic volcanoes. Diffusion of hydrogen (as H^+) through the olivine host crystal, however, can modify the water content of melt inclusions over minutes to hours. Here we develop a new 3D diffusion model for water loss from olivine-hosted melt inclusions which includes natural crystal shapes and multiple melt inclusions. We use our model to test the reliability of different types of analytical and numerical models using conditions of magma ascent from the 1977 eruption of Seguam volcano, Alaska. We find that 1D and 2D numerical models underestimate water loss and magma decompression rates because they do not account for additional water loss from all directions. An anisotropic analytical solution that we present compares well with the 3D model giving decompression rates within a factor of 2. Multiple melt inclusions can also shield each other and help to reduce water loss. Our modelling approach shows that factors such 3D crystal geometry and melt inclusion configuration can play an important role in constraining accurate decompression rates, and recovering water contents in natural magmatic systems.

1 Introduction

Water plays a significant role in the formation and physico-chemical evolution of magma. The addition of water can induce melting in the sub-arc mantle wedge by suppressing the solidus (Grove et al., 2006; Till et al., 2012), and is ultimately responsible for volcanism in subduction zone settings (Grove et al., 2012). Water can act as a network modifier in silicate melts meaning it can exert an important control on the rheological properties of magma such as viscosity and yield strength (Dingwell, 1996; Russell et al., 2002; Gonnermann & Manga, 2007), which in turn may exert first order controls on the storage depths of arc magmas (Rasmussen et al., 2022). The exsolution of water and other volatiles into a vapour phase can also affect magma compressibility (McCormick-Kilbride et al., 2016), eruptibility (Stock et al., 2016), and ultimately eruptive style (Cassidy et al., 2016). Furthermore, the addition of water to crystallising magma can have a large influence on mineral stability and subsequently chemical differentiation (Gaetani et al.,

68 1993); a notable example being the differences in the tholeiitic and calc-alkaline trends
69 (Zimmer et al., 2010).

70   Measuring reliable water contents in magmas is therefore of great importance for
71 understanding volcanic systems, but has proven challenging. As magma ascends to the
72 surface, the solubility of water in the melt decreases meaning it exsolves into a vapour
73 phase once kinetic and physical barriers to bubble nucleation are overcome (Gonnermann
74 & Manga, 2007). Degassing can further drive the buoyant ascent of magma and lead to
75 fragmentation and explosive eruptions; however, it means initial water contents cannot
76 be recovered from the erupted matrix glass. Petrologists have subsequently turned to
77 olivine-hosted melt inclusions in order to measure pre-eruptive volatile contents in basaltic
78 magmas to understand primary mantle melt compositions (Sobolev & Chaussidon, 1996)
79 and storage conditions at the time of entrapment (Ruth et al., 2018; Wieser et al., 2021).
80 This approach has been facilitated by advances in microanalytical techniques such as sec-
81 ondary ion mass spectrometry (SIMS) and Fourier transform infrared spectroscopy (FTIR),
82 but assumes that post-entrapment modification such as crystallisation (Steele-Macinnis
83 et al., 2011), decrepitation (Maclennan, 2017), or diffusive loss through the crystal host
84 (Gaetani et al., 2012) are minimal or can be corrected for. The water content of olivine-
85 hosted melt inclusions can be dominantly modified by diffusive loss or gain of hydrogen
86 (as H^+) through the olivine lattice (Gaetani et al., 2012; Hartley et al., 2015; Barth et
87 al., 2019; Barth & Plank, 2021). The ability of melt inclusions to retain their water con-
88 tent depends on a combination of geometrical factors (e.g., crystal size, melt inclusion
89 size and melt inclusion position), physico-chemical parameters (e.g., magma decompres-
90 sion rate, temperature, degassing style, diffusivity, and olivine-melt partitioning behaviour).
91 The diffusion of H^+, which can involve multiple mechanisms (Ferriss et al., 2018; Barth
92 et al., 2019) and inter-site reaction (Jollands et al., 2019), is typically very rapid mean-
93 ing most melt inclusions rarely preserve their initial water contents even for ascent timescales
94 on the order of hours (Gaetani et al., 2012; Barth & Plank, 2021). Consequently, initial
95 water contents typically have to be reconstructed using relationships between water and
96 incompatible major elements (e.g., K) or trace elements (e.g., Ce) across the melt inclu-
97 sion population (Hartley et al., 2015; Barth et al., 2019).

98   While rapid diffusive loss of water through the olivine lattice hinders initial water
99 content estimation, it does offer considerable promise as a chronometer to track decom-
100 pression rates during final magma ascent (Peslier & Luhr, 2006; Le Voyer et al., 2014;
101 Barth et al., 2019; Newcombe, Plank, Barth, et al., 2020). Popular olivine geospeedome-
102 ters (e.g., Fe–Mg interdiffusion, Ni, Ca) used to time pre-eruptive magma mixing and
103 ascent (Rae et al., 2016; Rasmussen et al., 2018; Mutch, Maclennan, Shorttle, et al., 2019;
104 Couperthwaite et al., 2020; Kahl et al., 2023) typically respond to chemical changes in-
105 duced at depth and do not have the temporal resolution with current microanalytical
106 techniques to track processes over timescales of minutes to hours (Bradshaw & Kent, 2017).
107 Fluid-mobile monovalent cations, such as hydrogen and lithium, can produce resolvable
108 diffusion profiles over minutes to hours at magmatic temperatures (Lynn et al., 2018;
109 Newcombe, Plank, Barth, et al., 2020). Their composition in the melt responds directly
110 to the degassing process meaning diffusion gradients can provide high resolution tem-
111 poral information about final magma ascent (Lynn et al., 2018; Neukampf et al., 2021).
112 These chronometers typically provide an average estimate of magma decompression from
113 vapour saturation, but can be combined with other complementary methods such as volatile
114 diffusion in melt embayments (Ferguson et al., 2016; Moussallam et al., 2019; Myers et
115 al., 2019; deGraffenried & Shea, 2021), crystal size distributions (Cashman & Blundy,
116 2000; Gurioli et al., 2005), mineral growth or dissolution (Neave & Maclennan, 2020),
117 or bubble number densities (Shea et al., 2010; Myers et al., 2021; Hajimirza et al., 2021)
118 to obtain a more complete picture of a magma's ascent history. Extracting this kind of
119 information about magma ascent opens up the exciting possibility to link magma decom-
120 pression rates to physico-chemical parameters and the predictions of conduit models (Barth
121 et al., 2019). In fact, correlations between magma decompression rate and eruption style

have recently been established, with basaltic eruptions with higher mass eruption rates being associated with faster decompression rates (Barth et al., 2019).

Diffusive loss of hydrogen through olivine has subsequently become a popular chronometer and has been used in two main ways: measuring and modelling water loss from a population of olivine hosted melt inclusions (Barth et al., 2019) or measuring water gradients directly in olivine (Newcombe, Plank, Barth, et al., 2020). The former offers the advantage that the water content of melt inclusions can be precisely measured by SIMS, whilst the latter can be used in olivine crystals that do not contain melt inclusions. Both of these modelling approaches have used assumptions either about crystal geometry or diffusion in multiple phases. 3D spherical approximations that assume infinite diffusivity in the melt inclusion and isotropic diffusion in the olivine host have been commonly used (Cottrell et al., 2002; Chen et al., 2011; Gaetani et al., 2012; Chen et al., 2013). 1D approximations along the [100] axis have since become favoured due to the high anisotropy measured for H^+ in Fe-bearing olivines with diffusion along the [100] potentially being more than 10 times faster than the [010] or [001] axes (Barth et al., 2019). The melt inclusion approach of Barth et al. (2019) assumes that diffusive loss dominantly occurs along the [100] axis, diffusivity in the melt inclusion is infinite and constant, and that the crystal is symmetric about the centre of the melt inclusion (reflective boundary condition in the centre of the melt inclusion). Likewise, Newcombe, Plank, Barth, et al. (2020) apply a 1D approximation along [100], but do not formally incorporate any complexities associated with melt inclusions. In addition, both modelling approaches fail to account for the interaction of multiple melt inclusions in a single crystal and how that could influence water loss.

In this study, we have developed a multi-phase finite element model for the concurrent diffusion of water in the melt inclusion and the surrounding host olivine. This approach facilitates the use of complex 3D geometries associated with idealised olivine crystal morphologies and has allowed us to assess the uncertainties associated with 1D and 2D approximations. Furthermore, we have also developed models to simulate the diffusive loss of water from olivine phenocrysts that contain more than one melt inclusion. This has allowed us to assess how the interaction of multiple melt inclusions can influence water loss in olivine phenocrysts akin to those observed in natural volcanic systems.

2 1977 Eruption of Seguam, Aleutian Arc

Application of geospeedometers based on the dehydration of melt inclusion and olivine macrocryst populations has the greatest potential in water-rich arc magmas, where the water contents of melt inclusions and gradients in the host crystals can be easily resolved using current microanalytical methods. In this study, we shall focus on erupted products from the March 1977 eruption of Seguam volcano to provide a framework for modelling water loss in olivine crystals from arc systems.

Seguam Island is an $\sim$200 km^3 volcanic complex in the central Aleutian Island arc, with a measured eruption chronology dating back to 318 k.y. in the Pleistocene (Jicha & Singer, 2006). The volcano has been historically active with eight eruptions over the past 200 years: notably two basaltic and basaltic-andesite fissure eruptions occurring in 1977 and 1992–1993 (Miller et al., 1998; Jicha & Singer, 2006). The 1977 eruption took place between the 6th and 8th of March, and was associated with 8 lava fountains erupting from a $\sim$1 km long radial rift on Pyre Peak (Miller et al., 1998). The lava fountains reached heights of up to 90 m, culminating in a maximum volcanic explosivity index (VEI) estimate of 1 for the eruption. The estimated volume of erupted basaltic material, including lava flows and pyroclastic deposits, is $\sim$0.06 km^3 based on stratigraphic analysis of present day deposits. The crystal cargo contains olivine, clinopyroxene and plagioclase (Zimmer et al., 2010; Lloyd et al., 2016). The olivine crystals are melt inclusion

rich (Figure 1). Attempts to characterise the pre-eruptive water content of the 1977 Seguam magma were made by Zimmer et al. (2010), who found that melt inclusion suites in forsteritic olivines (Fo$_{80\text{-}85}$) from basaltic tephra have been modified the least by degassing and preserve water contents up to 3.7 wt%. Plagioclase and clinopyroxene melt inclusions from more evolved samples have much lower water contents (< 2.5 wt%), which have been attributed to degassing (Zimmer et al., 2010). Comparison of the water content of clinopyroxene-hosted melt inclusions in lava flow and tephra samples show diffusive loss of water in the lava flow in less than 1 hour (Lloyd et al., 2016). Syneruptive decompression rates have recently been estimated by Newcombe, Plank, Barth, et al. (2020) using a combination of volatile diffusion in olivine-hosted melt embayments and modelling of water concentration gradients across melt inclusion free olivine phenocrysts. Newcombe, Plank, Barth, et al. (2020) found that decompression rate estimates for the 1977 Seguam eruption from both of these methods were fairly consistent and ranged from 0.02 to 0.23 MPa s^{-1}. The well-characterised decompression history of this eruption based on multiple petrological methods makes it an ideal candidate to compare decompression rates based on our new modelling approach, and provides a well constrained natural example to explore uncertainties associated with assumptions based on geometry and dimensionality.

3 Methods

3.1 Measurement of water concentration gradients in olivine phenocrysts by SIMS

Concentrations of volatiles (H$_2$O, CO$_2$, S, Cl, F) and P were characterized using the Cameca IMS 6f ion microprobe at Carnegie Earth and Planets Laboratory, following previously developed analytical protocols (E. Hauri, 2002; Koga et al., 2003; Mosenfelder et al., 2011; Kumamoto et al., 2017; Newcombe, Plank, Barth, et al., 2020). The analytical protocol is described in detail by Newcombe, Plank, Barth, et al. (2020) and is summarized here. Samples were gold coated and placed into the sample exchange chamber of the SIMS one to three days prior to the beginning of the analytical session. A Cs$^+$ primary beam with a current of $\sim$15–20 nA was tuned to achieve an approximate beam diameter of $\sim$20 μm, and charge compensation was provided by an electron flood gun. The sample was pre-sputtered for 120 s with the rastered primary beam in order to remove surface contamination, and a field aperture was used to ensure the collection of ions from the central $\sim$10 μm of the measurement area. Negatively charged ^{12}C$^-$, ^{16}O^{1}H$^-$, ^{19}F$^-$, ^{30}Si$^-$, ^{31}P$^-$, ^{32}S$^-$ and ^{35}Cl$^-$ ions were detected using an electron multiplier. Five cycles of data were collected at each point. Electrical glitches occasionally produced 'empty' cycles in which no counts were recorded; these cycles were deleted prior to data reduction. The mass resolving power was sufficient to resolve ^{16}O^{1}H$^-$ from ^{17}O.

Data reduction was approached following a protocol similar to that described by Kumamoto et al. (2017). Basaltic glasses and grains of olivine and orthopyroxene with well-characterized volatile contents were used as standards (see Supplementary data). The calibrations of water concentration in olivine used in this study are based on absolute water concentrations of olivine and orthopyroxene standards determined by Bell et al. (2003). Counts of volatile and ^{31}P$^-$ ions were divided by counts of ^{30}Si$^-$ in order to account for instrumental drift and multiplied by SiO$_2$/50 (where SiO$_2$ is the independently measured silica concentration of the sample in wt%). Drift in the H$_2$O analyses was further monitored and corrected for using frequent analyses of "Herasil 102" silica glass and basaltic glass ALV-519-4-1. The detection limit (Long & Winefordner, 1983) was calculated using replicate analyses of "Suprasil 3002" silica glass, and was found to be <4 ppm H$_2$O (this estimate is an upper bound, given the non-zero water concentration of Suprasil glass and the fact that the quality of the vacuum improved over the course of each session).

3.2 Measurement of major element compositions by electron microprobe

Olivines were analyzed for major, minor, and trace elements using a Cameca SX100 electron microprobe at the American Museum of Natural History (AMNH) and a JEOL JXA 8900R electron mricroprobe at the University of Maryland (UMD). The AMNH data were previously published by Newcombe, Plank, Barth, et al. (2020), whilst the UMD profiles are shown the in Supplementary data. AMNH analyses were conducted using a 15 kV accelerating potential, a 10 nA beam current and a focused beam (with nominal diameter ∼1 μm). UMD analyses were conducted using a 20 kV accelerating potential, a 20 nA beam current and a focused 1 μm beam. On-peak counting times at AMNH varied between 20s (Mg, Si, Ca, Mn, Al, Fe), and 40s (Ti and P). At UMD, on-peak counting times varied between 20s (Mg, Si, Fe) and 40s (Ca, Ni). Background counting times were set to 50% of the on-peak counting times. Analyses were corrected for inter-run calibration offsets using factors determined by replicate analyses of San Carlos olivine. Replicate analyses of San Carlos olivine yielded average 2 RSDs of <3% for SiO_2, MgO and FeO.

3.3 3D numerical modeling of water diffusion in olivine phenocrysts during syn-eruptive magma decompression

Modelling diffusive loss of water from olivine-hosted melt inclusions has typically involved using 1D analytical solutions of the diffusion equation, either using spherical approximations (Cottrell et al., 2002; Chen et al., 2013), or assuming diffusion along a 1D plane where diffusion along the [100] axis is dominant (Barth et al., 2019). 3D finite difference models have also been used, in which the geometry of the olivine crystal was approximated as a cuboid (Le Voyer et al., 2014). Spherical diffusion models fail to properly account for diffusive anisotropy, whilst more recent numerical attempts do not fully encapsulate the complex geometry of natural or idealised olivine crystals (Welsch et al., 2012; Shea et al., 2015). Furthermore, previous modelling attempts assumed that diffusivity of water in the melt inclusion was infinitely faster than diffusion in the olivine, meaning any changes in diffusivity in the melt inclusion due to changes in composition or intensive parameters were not fully accounted for.

Solving partial differential equations using finite elements has started to gain prominence in diffusion chronometry applications in igneous petrology (Mutch, Maclennan, Shorttle, et al., 2019; Mutch, Maclennan, Holland, & Buisman, 2019; Mutch et al., 2021). This is because finite elements offer an efficient way of solving the diffusion equation for complex geometries, such as those observed in natural crystals. In this study, we use FEniCS (Alnæs et al., 2015), a free open-source Python-based software, to develop a new 3D finite element diffusion model that can track the diffusive loss of water from olivine-hosted melt inclusions. This model includes two separate domains meaning it can be used to track changes in water concentration across the melt inclusion and the host olivine crystal. Diffusion across two domains was modelled as follows:

$$\rho_{MI}\frac{\partial C_{MI}}{\partial t} = \nabla \cdot (\rho_{MI}D_{MI}\nabla C_{MI}) \ \text{in} \ \Omega_{MI} \tag{1}$$

$$\rho_{Ol}\frac{\partial C_{Ol}}{\partial t} = \nabla \cdot (\rho_{Ol}D_{Ol}\nabla C_{Ol}) \ \text{in} \ \Omega_{Ol} \tag{2}$$

where C, D and ρ denote the concentration of water, the bulk diffusivity of water, and the density of the melt inclusion (Ω_{MI}) and olivine (Ω_{Ol}) domains as marked by the respective subscripts.

The two domains are separated by a boundary Γ. On this boundary we have the conditions

$$C_{Ol} = KC_{MI} \tag{3}$$

$$-\rho_{MI}D_{MI}\frac{\partial C_{MI}}{\partial n} = -\rho_{Ol}D_{Ol}\frac{\partial C_{Ol}}{\partial n} \tag{4}$$

255 where the first of these conditions represents the partitioning of an element with par-
256 tition coefficient K, and the second represents conservation of mass across the interface.
257 To avoid confusion with the diffusion coefficient, D, we opted to use K to represent the
258 partition coefficent, however we appreciate that this has traditionally been used to rep-
259 resent equilibrium constants and exchange coefficients. The olivine-melt partition coef-
260 ficient for water can range from 0.0005 (Le Voyer et al., 2014; Newcombe, Plank, Barth,
261 et al., 2020) to 0.003 (Koga et al., 2003; E. H. Hauri et al., 2006; Towbin et al., 2023).

We can the introduce the following rescaling:

$$\tilde{C} = \begin{cases} C_{\mathrm{MI}} & \text{in } \Omega_{\mathrm{MI}} \\ \dfrac{C_{\mathrm{Ol}}}{K} & \text{in } \Omega_{\mathrm{Ol}} \end{cases} \tag{5}$$

$$\tilde{D} = \begin{cases} D_{\mathrm{MI}} & \text{in } \Omega_{\mathrm{MI}} \\ D_{\mathrm{Ol}} & \text{in } \Omega_{\mathrm{Ol}} \end{cases} \tag{6}$$

$$\tilde{\rho} = \begin{cases} \rho_{\mathrm{MI}} & \text{in } \Omega_{\mathrm{MI}} \\ \rho_{\mathrm{Ol}}K & \text{in } \Omega_{\mathrm{Ol}} \end{cases} \tag{7}$$

With this scaling the system, we can represent the problem with a single diffusion equation in both domains,

$$\tilde{\rho}\frac{\partial \tilde{C}}{\partial t} = \nabla \cdot \left(\tilde{\rho}\tilde{D}\nabla\tilde{C} \right) \tag{8}$$

with standard continuity relationships across the interface Γ,

$$\left[\tilde{C} \right]_{-}^{+} = 0 \tag{9}$$

$$\left[-\tilde{\rho}\tilde{D}\frac{\partial \tilde{C}}{\partial n} \right]_{-}^{+} = 0 \tag{10}$$

262 We can then solve Equation (8) by standard methods with a spatially varying $\tilde{\rho}$ and $\tilde{D}$,
263 without needing to treat the interface in a special manner. This kind of approach, in which
264 there is a mass balance at the interface is also applied in multiphase exchange thermom-
265 etry in igneous and metamorphic systems (Müller et al., 2013). Like previous studies (Cottrell
266 et al., 2002), we assumed that the density ratio of olivine to melt was equal to 1.2. We
267 verified our model against 1D analytical solutions from Zhang (2009), which is shown
268 in the Supplementary Material.

269 Linear continuous Galerkin finite elements were used to represent concentration,
270 whilst a discontinuous Galerkin functional space (DG0) was used for the spatially-variable
271 $\tilde{\rho}$ and $\tilde{D}$ fields. A fixed Dirichlet boundary condition was maintained at the exterior bound-
272 ary of the crystal and was modified based on the composition of olivine in equilibrium
273 with the exterior melt as calculated by the basalt version of VolatileCalc (Newman &
274 Lowenstern, 2002; Rasmussen et al., 2020). Across both domains, olivine equilibrium com-
275 positions were calculated. The composition in the melt inclusion was then calculated us-
276 ing the partition coefficient at the end of each time step. The diffusion equation was solved
277 at each time step using an iterative Newton solver. A Crank-Nicholson (2nd order) time-
278 stepping scheme was used in the models. The number of time steps was typically set to
279 300, with the size of the time step being adjusted according to decompression rate. An
280 efficient algebraic multigrid preconditioned conjugate gradient solver was used to solve
281 the resulting systems of linear equations in 3D (Balay et al., 2019).

282 Finite element meshes were generated using Pygmsh and Gmsh version 3.0.0. (Geuzaine
283 & Remacle, 2017) An idealised morphology of the olivine crystal structure was based on
284 Welsch et al. (2012). We refined the mesh at the boundary between the olivine and the

285 melt inclusion. Meshes typically had 400,000 vertices. This was to balance spatial res-
286 olution with computational efficiency. The effect of spatial resolution on model accuracy
287 is shown in the Supplementary material. Once the mesh was defined, we then labelled
288 the separate domains and boundaries accordingly.

3.4 Selection of diffusion coefficients

290 There have been many experimental studies that have tried to characterise the dif-
291 fusion mechanisms of H^+ through the olivine lattice during either hydration or dehyr-
292 dration (Mackwell & Kohlstedt, 1990; Kohlstedt & Mackwell, 1998; Padrón-Navarta et
293 al., 2014; Peslier et al., 2015; Barth et al., 2019; Jollands et al., 2019; Barth et al., 2023).
294 Multiple diffusion mechanisms have been observed, which explains the six orders of mag-
295 nitude variation in experimentally derived diffusion coefficients at magmatic tempera-
296 tures ($\sim 1000\,°C$). The fastest mechanism measured in pure forsterite, called proton-polaron
297 exchange, is associated with a flux of H^+ being charge-balanced by a flux of electrons
298 from Fe^{2+} to Fe^{3+} (Mackwell & Kohlstedt, 1990; Kohlstedt & Mackwell, 1998). This re-
299 dox process progressively reduces Fe^{3+}. A slower mechanism associated with M-site va-
300 cancies has also been measured where a vacant M-site charge balanced by $2H^+$ exchanges
301 with either Fe^{2+} or Mg^{2+} parallel to the main H^+ gradient. The slowest mechanism is
302 associated with T-site vacancies, where a tetrahedral vacancy charge balanced by $4H^+$
303 exchanges with Si^{4+} (Padrón-Navarta et al., 2014; Jollands et al., 2019). Recently, it has
304 been shown that H^+ may migrate via a coupled reaction-diffusion process which could
305 involve exchange between different sites and subsequent diffusion via the different mech-
306 anisms (Jollands et al., 2019). Despite this complexity, dehydration experiments on nat-
307 ural olivines can describe bulk loss of H^+ with simple Arrhenius relationships (Ferriss
308 et al., 2018; Barth et al., 2019; Wallace et al., 2021). Dehydration experiments conducted
309 by Barth et al. (2019) and Barth et al. (2023) on Fe-bearing olivines from Cerro Negro
310 (Fo_{79-81}) and Etna (Fo_{90}) show significantly higher diffusivities for bulk H^+ than those
311 observed in pure synthetic forsterite. They found that diffusion was considerably faster
312 along the [100] direction, which is consistent with the proton-polaron mechanism. Barth
313 et al. (2019) attribute their higher diffusivities to the higher Fe content of their olivines.

314 Given the wide range in recorded diffusivities, it is therefore important to select
315 the appropriate diffusion mechanism and diffusion coefficient for the system of interest.
316 In this study, we are interested in modelling dehydration in Fe-bearing olivines analogous
317 to the crystal cargo observed at Seguam (Fo_{80-85}). We have opted to use the diffusion
318 coefficient of Barth et al. (2019), which was derived from experimental dehydration of
319 $\sim Fo_{80}$ olivines:

$$D_{Ol}^{[100]}(m^2 s^{-1}) = 9.6 \times 10^{-6} \exp\left(\frac{-125(\text{kJ/mol})}{RT}\right) \tag{11}$$

320 This diffusion coefficient was calibrated using 2 experiments run at 800 and $1000\,°C$,
321 and subsequently requires a small extrapolation up to temperatures appropriate for Seguam
322 magma ($\sim 1070\,°C$).

323 Diffusivity of water in the melt inclusion was calculated using the diffusion coef-
324 ficient of Ni and Zhang (2018). Here the diffusivity of total water is dependent on tem-
325 perature, pressure, melt composition. Most importantly, there is a dependence of dif-
326 fusivity on water content, which adds extra complexity that affects the efficiency of the
327 computational model. This is because the diffusion equation now takes a non-linear form
328 and has to be solved using iterative solvers at each time step. The expression of Ni and
329 Zhang (2018) involves a lot of input parameters, which can also slow down the models.
330 For 3D models with a high number of mesh points we used an empirical polynomial ex-
331 pression derived from solutions to the Ni and Zhang (2018) parameterisations at con-
332 ditions suitable for the 1977 eruption of Seguam (T $\sim 1070\,°C$, $H_2O \sim 0.3$-4.2 wt %):

$$D_{\mathrm{MI}}(m^2 s^{-1}) = 1.546 \times 10^{-12} C_{\mathrm{MI}}^3 - 1.302 \times 10^{-12} C_{\mathrm{MI}}^2 + 7.442 \times 10^{-12} C_{\mathrm{MI}} + 1.522 \times 10^{-12} \quad (12)$$

This parameterisation makes computation of D_{MI} much faster given the smaller number of variables, however it can only account for the effect of water content and is only applicable to melt compositions similar to Seguam melt inclusion Seg1-MI1 (Newcombe, Plank, Zhang, et al., 2020) at a temperature of 1070 °C. In this study we assume isothermal ascent (Newcombe, Plank, Zhang, et al., 2020) and that the major element composition of the melt inclusions do not change during ascent. Seguam melt inclusions suffered very little post-entrapment melting or crystallization during ascent: Rasmussen et al. (2020) calculate the extent of post-entrapment crystallization to be –1 to 4 wt% (where negative values indicate post-entrapment melting). Compositional changes in response to such small quantities of post entrapment crystallisation or melting are unlikely to significantly affect total water diffusivity. For models with fewer mesh points and which were run at different sets of temperatures (e.g., 2D inversions, see below) we used the original parameterisation of Ni and Zhang (2018).

3.5 2D inversions of natural melt inclusion-bearing olivine phenocrysts from Seguam

There are still some uncertainties associated with parameters that control water loss from olivine crystals and their associated melt inclusions. The most important parameters that have first order experimental approximations, but have yet to be widely applied to natural samples, are the diffusive anisotropy and the olivine-melt partition coefficient for water. In order to select parameters that are representative of the 1977 Seguam eruption for our 3D modelling, we ran 2D inversions on the selected crystals which were measured by SIMS. Bulk water measurements were made in the melt inclusion and in profiles close to the [100] and [001] direction. We generated 2D finite element meshes of the crystals using Gmsh (Geuzaine & Remacle, 2017) and crystal outlines generated in ImageJ (Schindelin et al., 2012). The melt inclusions and the host olivine crystal were flagged as different domains in the mesh. We used electron backscatter diffraction (EBSD) measurements of the crystals to calculate the angles between the [100] and [001] axes of the mesh with the main crystallographic axes, which was then used to adjust the diffusion coefficients in olivine down these directions.

The 2D inversions were conducted using DFENS (Mutch, Maclennan, Holland, & Buisman, 2019; Mutch et al., 2021), which employs a Monte Carlo Bayesian method using Nested Sampling (Feroz et al., 2009; Buchner et al., 2014). This approach allows for parameter estimation as well as a means to characterise the associated uncertainties. We inverted for 7 different parameters including: decompression rate, H^+ in olivine diffusive anisotropy, the olivine-melt partition coefficient, the initial water content, temperature, and the underlying parameters that are in the diffusion coefficient of H^+ in olivine (e.g., the exponent of D_0 and the activation energy). We used log uniform prior distributions for decompression rate (0.01 – 0.5 MPa s^{-1}), diffusive anisotropy (1–100) and the olivine-melt partition coefficient (0.0001 – 0.002) to get better representation of smaller values over multiple orders of magnitude. The decompression rate prior encapsulates the range of decompression rates already measured in the 1977 Seguam eruption (Newcombe, Plank, Barth, et al., 2020). The anisotropy and partition coefficient priors cover the range of values observed from natural and experimental studies (E. H. Hauri et al., 2006; Le Voyer et al., 2014; Newcombe, Plank, Barth, et al., 2020; Barth & Plank, 2021; Towbin et al., 2023). A uniform prior was used for initial water content (measured melt inclusion content to 6 wt%), which captures the variability observed in the melt inclusion population and also accounts for considerable water loss upon ascent. A Gaussian prior was used for temperature (1070 ± 20 °C) using an estimate based on melt thermometry and the 1σ uncertainties conducted on Seguam matrix glass using the Sugawara (2000) thermome-

ter (Newcombe, Plank, Zhang, et al., 2020). Mutivariate Gaussian priors were used for $\log_{10} D_0$ (-5.0 ± 0.4)and E_a (125 ± 10 kJ mol^{-1}), which were obtained from the experimental results of Barth et al. (2019) and error propagation by Barth and Plank (2021). To account for the covariance in uncertainty structure of the parameters contributing to the diffusion coefficient (Mutch et al., 2021), we generated a covariance matrix which was used in the modelling. Given the lack of experimental data available for dehydration in Fe-bearing olivines, this covariance is just a basic estimate.

In each simulation we generated a H_2O solubility curve which was used as the degassing boundary condition during decompression. These were calculated using a python version of VolatileCalc (Newman & Lowenstern, 2002; Rasmussen et al., 2020) using the major element content of Seguam tephra glass, the initial water content generated from the prior and a CO_2 content of 900 ppm (Moore et al., 2015). We used the basalt version of VolatileCalc and set the SiO_2 content of the Seguam melt to the maximum accepted value of 49 wt%, given that the Seguam tephra glass slightly exceeds this value (50.55 wt%). We assumed that there was closed system and equilibrium degassing with 2 wt% excess CO_2 at the start of each run to fit with the observations made by Newcombe, Plank, Barth, et al. (2020) and Rasmussen et al. (2020). Each model had 5000 steps, and the degassing curve terminated at the pressure that corresponded to 0.3 wt% water, which is the water content of glass measured at the edge of Seguam embayments (Newcombe, Plank, Barth, et al., 2020). To ensure that the inversions were completed in a timely manner, each model realisation was run with 100 time steps, with the size of the time step being controlled by the corresponding decompression rate. Mesh resolution was maintained at 10 -15 μm in the olivine and 7 -10 μm in the melt inclusion.

4 Results

4.1 Seguam crystal cargo

Seguam olivines show prominent zoning in bulk water content, which decreases away from the large central melt inclusions towards the crystal edge (Figure 2). Water concentrations are typically 13 – 24 ppm next to the melt inclusion and are 4 – 6 ppm next to the crystal edge. Analyses measured directly next to the melt inclusions may be elevated in water content due to contamination from the melt inclusion itself. The zoning profiles are most prominent along [100] (the a axis) and gradually decrease from the melt inclusion to the crystal edge. Profiles measured along [001] (the c axis) show sinusoidal profile shapes with steep gradients close to the melt inclusion and crystal edge and a plateau in between. This is most prominently shown in Seg1-MI1. Melt inclusion water compositions range from 3.5 – 3.84 wt%. Zoning in forsterite content is relatively minor with crystal cores of Fo_{83} and thin normal zones extending to Fo_{81-82} at the crystal edge. Seg4-MI1 is the exception, with reverse zoning from the crystal centre (Fo_{82}) to a mantle of Fo_{83} which in turn is surround by a normally zoned outer rim.

4.2 Seguam 2D inversion results

We performed 2D inversions on three melt inclusion-bearing phenocrysts from Seguam (Seg1-MI1, Seg4-MI1, Seg13-MI1). The models that occupy the maximum likelihood space fit the data well (Figure 2), with the general exception of points adjacent to the melt inclusions. These analyses may have been contaminated by the melt inclusion giving them their elevated water concentration, or they may be the product of a partitioning mechanism that is not incorporated in the current model framework (Lynn & Warren, 2021).

Each crystal generally required 10,000 to 40,000 Monte Carlo realizations to reach convergence. Trade-offs in the posterior distributions of the seven inverted parameters for one of the crystals (Seg13-MI1) can be observed in Figure 3. Strong trade-offs can be observed between decompression rate, temperature and the diffusion coefficient pa-

rameters. Minor trade-offs between the decompression rate, the partition coefficient and initial water content have also been observed, with weak negative correlations between initial water content and partition coefficient, and decompression rate and the partition coefficient. Given all of these parameters play a major role in controlling water loss from the melt inclusion, changes in one parameter can come at the expense of the others. For example, higher temperatures are associated with faster diffusivities and thus require a higher decompression rate to match any potential water loss. Conversely, correlations with the partition coefficient likely reflect the models ability to fit the SIMS profile data.

Inversion results for all three crystals are shown in Figure 4. Posterior distributions for temperature and the diffusion parameters (D_0 and E_a) typically agree with their Gaussian priors, and thus reflect their initial uncertainties. Decompression rate, anisotropy and partition coefficient posteriors fall within their respective priors and show the greatest inter-crystal variability which indicates they are being controlled by the data.

Estimated linear decompression rates show some agreement with the range estimated by Newcombe, Plank, Barth, et al. (2020) by volatile diffusion in embayments (0.02 – 0.13 MPa s^{-1}) and water gradients in olivine phenocrysts (0.04 – 0.23 MPa s^{-1}). Seg13-MI1 falls within this range with a median decompression rate of 0.07 MPa s^{-1} with a 1σ uncertainty of 0.01 MPa s^{-1}. Seg1-MI1 and Seg4-MI1 have faster decompression rates than those measured by Newcombe, Plank, Barth, et al. (2020), with medians of 0.36 and 0.32 MPa s^{-1}. Each has a typical 1σ uncertainty of 0.04 MPa s^{-1}. Differences between crystals are also apparent in the partition coefficient and anisotropy posterior distributions. All modelled crystals require much lower partition coefficients (0.0004 – 0.0007) than those that have been measured experimentally (> 0.001), but do broadly agree with values measured in natural systems (Le Voyer et al., 2014; Newcombe, Plank, Barth, et al., 2020). Seg4-MI1 requires a higher partition coefficient to fit the profile dataset (0.00067) than for Seg1-MI1 and Seg13-MI1 (0.00043 to 0.00048). The best fit profile for Seg4-MI1 requires no diffusive anisotropy between the [100] and [001] directions. Seg1-MI1 and Seg13-MI1 require much higher anisotropies with median values of 21 $\pm$ 15 and 35 $\pm$ 15 respectively. These agree with the high anisotropies observed experimentally by Ferriss et al. (2018) and Barth et al. (2019). These anisotropy distributions have long tails that extend to higher anisotropies. This likely reflects the model's lack of sensitivity to high anisotropies given the spatial resolution of the SIMS profiles. Finally, initial water contents generally converged towards the melt inclusion value, which reside at the lower end of the priors and is below the estimated maximum for Seguam (4.2 wt%). This suggests that the melt inclusions lost nearly no water during magma ascent. The models, however, may be preferentially converging to lower initial water content values given the large uncertainties in other free-floating parameters such as the partition coefficient, diffusion coefficient and anisotropy. If these parameters can be associated with tighter priors, then initial water may be more accurately constrained by these type of inversions.

5 Discussion

5.1 Variability in inverted parameters at the 1977 eruption of Seguam

Of the three olivine crystals from the 1977 eruption of Seguam that we conducted 2D inversions, we have identified two distinct populations based on inverted decompression rates and geochemical parameters associated with diffusion, notably diffusive anisotropy and the partition coefficient. Seg1-MI1 and Seg4-MI1 show consistent decompression rates, which are a factor of 5 greater than the rate determined by Seg13-MI1. Seg13-MI1 and Seg1-MI1 show consistent partition coefficients and to a lesser degree diffusive anisotropy, which differ to those estimated for Seg4-MI1. In the case of anisotropy, our inversions suggest that H$^+$ diffusion in Seg4-MI1 is almost isotropic, which conflicts with recent experimental observations (Ferriss et al., 2018; Barth et al., 2019). However, other low aniso-topy examples have also been found in the Seguam crystal cargo by Newcombe, Plank,

Barth, et al. (2020). The discrepancies in inverted parameters that we observe across the Seguam crystal cargo could be due to several different reasons. They could relate to the underlying major and minor element chemistry of the olivines. Forsterite profiles measured across each crystal parallel to the SIMS profiles show that Seg1-MI1 and Seg13-MI1 have relatively flat cores between Fo_{83} and Fo_{84} and a simple outer rim, whilst Seg4-MI1 contains an inner core of Fo_{82} surrounded by a reversely zoned mantle (Fo_{83}) and then an outer rim (Figure 2). These different zoning patterns not only suggest that these crystals may have undergone slightly different magma ascent histories, but also they may have different defect populations that could affect the diffusion of H^+ (Jollands et al., 2019). These discrepancies could then be associated with caveats in our diffusion modelling methods which are discussed in more detail below.

Variations in decompression rate observed across the modelled crystal population could also be the result of limitations in the diffusion modelling, or could reflect natural physical processes. Magma may undergo complex ascent histories in which velocity may change across the width of the conduit, conduit flow regime may change, turbulence might be induced by rough conduit walls, or the magma may stall at different points in the conduit (Gonnermann & Manga, 2007; Myers et al., 2019). Water in olivine crystal chronometry is sensitive to changes in the local environment, meaning individual crystals may be recording different aspects of these complexities. For example, entrained crystals that ascended in different parts of the conduit may record different decompression rates. Alternatively, crystals erupted at different points during a single eruption may record changes in ascent histories. Due to the large uncertainties associated with individual decompression rates of each crystal, these individual histories may be difficult to disentangle. Improving the uncertainties on the diffusion coefficients by further understanding the associated diffusion mechanisms could help to resolve this issue.

5.2 Monte Carlo simulation of magma ascent

Crystal geometry and diffusive anisotropy have been shown to play an important role in diffusion modelling of major (e.g., Fe–Mg interdiffusion) and minor elements (Ni, Mn, Ca) in olivine (Shea et al., 2015). Given the very high diffusivity of H^+ in olivine, which can be up to 8 orders of magnitude faster than Fe–Mg interdiffusion (Dohmen & Chakraborty, 2007), multi-dimensional and geometrical considerations may become even more important for water loss or gain during magmatic processes. Recent work has argued that 1D models of diffusive loss of water from melt inclusions and the host olivine along the [100] direction are the best approximations given the very high diffusive anisotropy observed in dehydration experiments of Fe-bearing olivines (Ferriss et al., 2018; Barth et al., 2019; Barth & Plank, 2021). The modelling framework proposed by Barth et al. (2019) for water loss from olivine-hosted melt inclusions is a 1D model from the centre of the melt inclusion to the nearest crystal edge along the [100] crystallographic axis. This model applies a reflective Neumann boundary condition at the centre of the melt inclusion and a fixed Dirichlet boundary condition at the edge of the crystal. The model therefore assumes that crystal is symmetrical about the melt inclusion (i.e. the melt inclusion is at the centre of the crystal) and that the flux out of the crystal is dominated by the shortest [100] direction along the ascent pathway. Here we applied a Monte Carlo approach with the aim to understand the the role of 3D crystal geometry and melt inclusion configuration on estimates of water loss from melt inclusions during magma ascent. This approach was then used to test the efficacy of 1D and 2D numerical models as well as analytical solutions at constraining melt inclusion water loss and thus retrieving decompression rates.

5.2.1 Model set up

We based our models on physical and chemical observations of the 1977 Seguam eruption. Temperature ($1070\,°C$), the final melt water content (0.3 wt%), initial CO_2 con-

tent (900 ppm), degassing style (closed system with 2wt% excess CO_2), and the major element content of the melt were fixed for all simulations. Given the broad range of olivine-melt partition coefficients and diffusive anisotropies observed in the Seguam samples, along with the large uncertainties associated with experimental values, we ran model subsets with different selected partition coefficients and anisotropies. For the partition coefficent, we ran a subset with a fixed value of 0.000459, which was based on the median value of the 2D inversion results from crystals SegMI1 and Seg13-MI1 (Figure 4), a subset with a fixed value of 0.001 which is approximately equal to the refined experimental value (0.0009 ± 0.0003) from Towbin et al. (2023), and a subset in which the partition coefficient was randomly selected from a uniform prior spanning the full range of natural and experimental measurements (0.0004 – 0.002). We then used three different anisotropies in which diffusion along the [100] direction is 3, 15.6 or 35 times faster than [010] and [001]. These anisotropies encapsulate the range retrieved from the 2D Seguam inversions in addition to the experimental observations (Barth et al., 2019). The anisotropy of 15.6 was selected by fitting a log-normal distribution to the combined anisotropy distributions of crystals Seg1-MI1 and Seg13-MI1, and then taking the mode value. Other physico-chemical and geometrical parameters were varied in different model realisations in order to simulate a natural crystal population. Distributions of these parameters are presented in Figure 5. A log uniform prior was used for decompression rate, which encompasses linear decompression rates for basaltic eruptions presented by Barth et al. (2019) (0.0001 – 0.5 MPa s^{-1}). A uniform prior was used to determine the crystal size, which was based on the [001] axis length (250 – 750 μm) from the centre of the crystal. Uniform priors were used for melt inclusion configuration and geometry including the melt inclusion radius (10 – 100 μm) and the position of the melt inclusion centre along the main crystallographic axes. To make sure that the melt inclusions were not too close to the crystal edge, we set the maximum distance along each crystallographic axes to be crystal axis length minus the melt inclusion radius plus a tolerance. The tolerance was one quarter of the melt inclusion radius. We then implemented an algorithm to ensure that the mesh generation failed if the melt inclusion intersected any crystal edge. This explains the non-uniform distributions associated with the melt inclusion position, particularly along the [001] and [001] directions. The smaller length of the [010] axis means that most meshes were successfully generated if the melt inclusion was positioned towards the centre of the [010] axis. This was particularly true if the melt inclusion radius was large with respect to the [010] axis length. Olivine crystals are typically tapered towards the ends of the [001] and [100] axes. This means there is a higher chance for larger melt inclusions to intersect crystal edges, and that meshes in which the melt inclusions were closer to the centre of the crystal pass the edge intersection criteria and are thus successfully generated. A uniform prior was also used for the initial water content (3.5 – 5.0 wt%), which influenced the starting depth and degassing path of the ascending magma. This is because the initial and excess CO_2 values were kept constant meaning the changes in H_2O would cause changes in entrapment pressure and the degassing curve. In reality, the Seguam magma may have only resided on a single degassing curve upon ascent with the CO_2 and H_2O content in each melt inclusion covarying. In total, 1015 simulations were run using the three different anisotropies. A subset of 463 models were run using the Seguam derived partition coefficient (0.000459), a subset of 265 models were run using a partition coefficient of 0.001, and 287 models were run with a randomly selected partition coefficient.

In each Monte Carlo simulation a 3D forward model was run and the composition at the centre of the melt inclusion was tracked through time. The water content at the end of the decompression path was recorded. The mesh resolution was determined by both the crystal size and melt inclusion radius in order to balance accuracy and computational efficiency. The mesh point spacing was determined to be 60 times smaller than the length of the [001] axis from the centre of the crystal. This resulted in mesh resolutions of 4 to 12.5 μm, which is comparable to other 3D modelling efforts that have explored H^+ diffusion in olivine (Lynn & Warren, 2021). The mesh resolution in the melt inclusion was determined to be one twelfth of the melt inclusion radius, which resulted

588 in mesh resolutions of 0.8 to 8.3 μm. The melt inclusion was surrounded by a mesh of
589 the same resolution, which extended to a distance based on the melt inclusion radius.
590 This then transitioned to the mesh resolution of the host olivine over the lenghscale of
591 the melt inclusion radius. In each model a constant number of 300 time steps were used,
592 which would result in individual time steps varying from 2.1 seconds to 3.8 hours depend-
593 ing on the decompression rate and starting pressure.

594 We then ran equivalent 1D and 2D models using the same physico-chemical param-
595 eters in each 3D Monte Carlo model. The same mesh resolutions and time steps were
596 used to maintain consistency with the 3D models. We use two types of 1D model termed
597 here the symmetric and asymmetric models. For the symmetric models, we generated
598 a mesh that extends from the centre of the melt inclusion to the closest edge of the crys-
599 tal along the [100] direction. In this instance it is assumed that the crystal along the [100]
600 axis is completely symmetric around the centre of the melt inclusion, which is implemented
601 using a Nuemann or no-flux boundary condition at the centre of the melt inclusion. This
602 is to simulate the approach recently adopted by Barth et al. (2019). For the asymmet-
603 ric models (Figure 6), we generated a mesh that extends from one crystal face to the other
604 along the [100] axis, and which goes through the centre of the melt inclusion. For mod-
605 els in which the melt inclusion is not in the centre of the crystal, this creates an asym-
606 metric 1D arrangement along [100]. In this model type, Dirichlet boundary conditions
607 were applied at the edges of the crystal. We also generated two types of 2D model, the
608 first uses a 2D section of the crystal that includes the centre of the melt inclusion us-
609 ing the (010) plane, whilst the second uses the (001) plane (Figure 6). In these 2D mod-
610 els, the corresponding anisotropy was used.

611 The 1D and 2D models were run under the same conditions as the 3D models, and
612 the water content at the centre of the melt inclusion at the end of the decompression path-
613 way was recorded for comparison. We also ran Nested Sampling Bayesian inversions in
614 order to extract magma decompression rates. In this case we used the the final melt in-
615 clusion water content of the 3D models for each anisotropy to fit the 1D and 2D mod-
616 els. The inversions were conducted using PyMultinest (Feroz et al., 2009; Buchner et al.,
617 2014) with the only invertible parameter being decompression rate. All other physico-
618 chemical parameters were fixed to the values used in the 3D forward models. We used
619 a log uniform prior for decompression rate which encapsulated a much wider range than
620 was used in the Monte Carlo forward models ($0.00001 - 0.5$ MPa s^{-1}). The decompres-
621 sion rate that maximised the log likelihood function was then used as the inverted de-
622 compression rate.

5.3 Model comparison

5.3.1 Comparing 1D and 3D numerical models

625 In general, the 1D models underestimate the amount of water loss when compared
626 to the 3D models (Figure 7). The differences in the 3D versus 1D models are lowest at
627 low or high percentages of water loss. The former are likely to be associated with high
628 decompression rates or large melt inclusions meaning there is insufficient time for dis-
629 cernible water loss between the two types of models. The latter, is most likely associ-
630 ated with smaller inclusion sizes and low decompression rates where the melt inclusion
631 is approaching equilibrium. This discrepancy between model types is greatest when the
632 1D models are compared to 3D models conducted at low anisotropy (3.0), but dimin-
633 ishes for 3D models conducted at higher anisotropy (15.6 and 35). For example, the 1D
634 models typically under predict melt inclusion water loss by up to $40 - 50$ % when com-
635 pared to 3D models that use an anisotropy of 3.0, whereas this typically falls within 30
636 % for the 15.6 and 35 anisotropy models. This effect can simply be explained by the ex-
637 tra amount of water loss along the extra dimensions in the crystal. The effect would be

greatest at lower anisotropies as faster diffusion along these extra dimensions would not be properly accounted for in the 1D models.

A similar effect can be observed in inverted decompression rates, where 1D models underestimate decompression rates relative to the 3D models (Figure 8). This is because the 1D models lose less water than their 3D counterparts, therefore lower decompression rates are required by these models to match the final water content of the 3D models. At high diffusive anisotropies (15.6 and 35) nearly all of the inverted decompression rates from both sets of 1D models falls within a factor of 10 of the 3D model decompression rates. For the 1D symmetric models 88–94 % of inversion results were within a factor of 5 of the 3D decompression rates, whilst 78–90 % of the 1D asymmetric models fell within a similar range. Only 40–56% of 1D symmetric models and 14–26% of 1D asymmetric models gave inverted decompression rates within a factor of 2 of the 3D decompression rates. At low diffusive anisotropies (3.0), the 1D models generally performed more poorly with 47% of 1D symmetric and 27% of 1D asymmetric decompression rates falling within a factor of 5 of the 3D results.

Geometrical effects on inverted decompression rates are summarised in Figure 9 which shows how the ratio of predicted decompression rates based on 1D and 3D models ($R_{1D/3D}$) changes based on the shortest distance from the edge of the melt inclusion to the edge of the crystal along the [100] axis ($MI_{[100]}$) with respect to the length of the [100] direction from the crystal centre ($L_{[100]}$). For melt inclusions situated close to the centre of the crystal ($MI_{[100]}/L_{[100]}$ is close to 1), the $R_{1D/3D}$ of both asymmetric and symmetric models is similar. For models with low anisotropy (3.0), $R_{1D/3D}$ is approximately 0.1–0.2. At higher anisotropies (15.6 and 35), $R_{1D/3D}$ is 0.3–0.5. In this geometrical configuration, the symmetric and asymmetric models are almost identical. As the melt inclusion is moved closer to the crystal edge ($MI_{[100]}/L_{[100]}$ approaches 0), the $R_{1D/3D}$ of the asymmetric models approaches 0.75 for the low anisotropy configuration and approaches 1.0 for the high anisotropy configurations. This is because the the diffusive flux along the short dimension of [100] becomes dominant and diffusive loss from other directions becomes less significant. In this geometrical configuration, the 1D approximation can create a more accurate result.

The 1D symmetric models actually overpredict decompression rate as the melt inclusion moves closer to the crystal edge along [100] (i.e., the $R_{1D/3D}$ approaches values above 1.0). This effect is likely due to the trade-off between the water loss associated with extra dimensions and the artificial increase in the flux out of the melt inclusion in symmetric models by assuming that the crystal is symmetrical about the melt inclusion. If the melt inclusion is positioned off-centre and close to the edge of the crystal (i.e. the 1D profile is highly asymmetrical), the symmetric model will significantly underestimate the distance from the centre of the melt inclusion to the furthest crystal edge. This means that more water will be lost over the same time period because the length scale of diffusion is shorter in the symmetric model.

Melt inclusion size relative to the crystal size also affects 1D models ability to replicate the 3D decompression rates (Figure 9). Smaller melt inclusions tend to underpredict decompression rates to a greater degree than larger inclusions when compared to the 3D models. This is the case for both 1D symmetric and asymmertric models, and is because smaller melt inclusions are more sensitive to water loss from the other dimensions. Furthermore, larger melt inclusions are more likely to have a shorter distance between the edge of the inclusion and the edge of the crystal along the [100] axis, which would increase the validity of a 1D approximation. To try and account for geometrical effects, such as melt inclusion location and size, on 1D inverted decompression rates we fitted empirical models to the distributions shown in Figure 9 using the form:

$$R_{1D/3D} = a_1 \cdot \exp\left(-a_2 \cdot \frac{MI_{[100]}}{L_{[100]}}\right) + a_3 \cdot \left(\frac{r_{MI}}{L_{[100]}}\right) + a_4 \tag{13}$$

678 where the coefficients $(a_1 - a_4)$ for each parameter and anisotropy are shown in Table
679 1, $MI_{[100]}$ is the location of the melt inclusion along [100], r_{MI} is the radius of the melt
680 inclusion, and $L_{[100]}$ is the length of the [100] axis from the centre of the olivine to the
681 edge. This empirical fit generates a scaling factor ($R_{1D/3D}$) that could potentially cor-
682 rect decompression rates calculated by the 1D symmetric (Barth et al., 2019) and asym-
683 metric methods, which may help to reduce the amount of scatter in decompression rates
684 estimated by 1D symmetric and asymmetric melt inclusion models.

685 ### 5.3.2 Comparing 2D and 3D numerical models

686 Two dimensional models also consistently underestimate water loss (Figure 7) and
687 decompression rates (Figure 8) compared to 3D models. Given the computationally in-
688 tensive nature of the 2D inversions, only 49 were completed. Overall, the 2D models pro-
689 duce predictions that are closer to the 3D models and are associated with tighter dis-
690 tributions than the corresponding 1D models. For example, nearly all of the 2D mod-
691 els return water loss values within 20 % of the 3D values regardless of diffusive anisotropy,
692 decompression rate and melt inclusion configuration. Meanwhile, 60–70% of the 2D in-
693 verted decompression rates are within a factor of 2 of the 3D decompression rates, al-
694 beit with a much smaller sample size. This is because the 2D models provide a more ac-
695 curate representation of crystal and melt inclusion geometry than 1D models, and can
696 also account for water loss in two dimensions rather than one. The ability of 2D mod-
697 els to faithfully capture water loss from a melt inclusion therefore depends on the flux
698 of water along the additional unconstrained dimension. This will largely depend on the
699 location of the section in which the 2D model is conducted, and its distance from ad-
700 ditional edges of the crystal in the third dimension. It is therefore more crucial for the
701 2D models to capture the water loss along the shorter dimensions and those with higher
702 diffusivities. In a typical idealised olivine crystal, this would be the (001) sections.

703 ### 5.3.3 Comparing anisotropic analytical solution and 3D numerical mod-
704   els

Analytical solutions offer the most efficient means for calculating diffusive water
loss from olivine-hosted melt inclusions (Gaetani et al., 2012; Bucholz et al., 2013). These
methods are, however limited by simplifying assumptions about geometry and diffusive
anisotropy. For example, many studies have used the analytical solution of Qin et al. (1992),
which assumes isotropic diffusion in a spherical host mineral. Given the potentially highly
anisotropic nature of H^+ diffusion in olivine, analytical solutions that capture this be-
haviour may be more appropriate. Analytical solutions for the diffusive equilibration of
an elliptical inclusion in an unbounded host mineral can be adapted to solve diffusive
equilibration of a spherical melt inclusion in an anisotropic host. The equilibration timescale,
τ, can be expressed as:

$$\tau = \frac{\rho_{\mathrm{MI}} a^2 R_F \left(D_{[100]}^{-1}, D_{[010]}^{-1}, D_{[001]}^{-1} \right)}{3\rho_{\mathrm{Ol}} \sqrt{D_{[100]} D_{[010]} D_{[001]}}} \tag{14}$$

where ρ_{Ol} and ρ_{MI} are the densities of olivine and the melt inclusion respectively. $D_{[100]}$,
$D_{[010]}$ and $D_{[001]}$ are the olivine diffusivities along the [100], [010] and [001] directions.
R_F is a Carlson completely-symmetric elliptic integral of the first kind, and a is the melt
inclusion radius. The derivation of this solution is available in the Supplementary Ma-
terial. This analytical solution assumes that the melt inclusion was sufficiently small that
it sees the crystal as an effectively infinite domain, and that diffusion in the inclusion
is rapid, such that the diffusivity of H^+ in the crystal sets the rate of equilibration. We
can use the estimate of equilibration time scale to approximate the behaviour of water
in the melt inclusion when the boundary conditions change over time. If C_i is the melt
inclusion water concentration and C_0 is the concentration of water in the surrounding
melt, the equilibration on a time scale τ can be represented by the simple ordinary dif-

ferential equation:

$$\frac{\mathrm{d}C_i(t)}{\mathrm{d}t} = \frac{C_0(t) - C_i(t)}{\tau} \tag{15}$$

If $C_0(t)$ were constant, this would be exponential decay. The solution of the above ordinary differential equation can be written in integral form as

$$C_i(t) = \mathrm{e}^{-t/\tau}\left(C_i(0) + \int_0^t C_0(s)\frac{\mathrm{e}^{s/\tau}}{\tau}\,\mathrm{d}s\right) \tag{16}$$

and the integral can be approximated by the trapezoidal rule if $C_0(t)$ is given, as would be the case for a water solubility model.

In terms of melt inclusion water loss, the analytical solution presented in Equation (14) also underestimates water loss relative to the 3D numerical models. It performs relatively well with over 90 % of the water loss estimates from the analytical solution falling within 10 % of the 3D models regardless of the degree of equilibration and the diffusive anisotropy (Figure 8). These underestimations also translate into decompression rates for the same reasons as the 1D and 2D numerical models as discussed above. Over 90 % of inverted decompression rates fell within a factor of 5 of the 3D values, whilst 50–80% fell within a factor of 2. The performance of the analytical solution appeared to improve with decreasing anisotropy. Like the 1D numerical models, we can then compare the ratio of inverted decompression rates from the analytical models and original 3D decompression rates ($R_{A/3D}$) to parameters related to melt inclusion size and configuration (Figure 9). Melt inclusion position along the [100] axis and melt inclusion radius play a major role in determining the accuracy of the inverted decompression rate from the analytical solution. The reason the analytical solution underestimates water loss is likely related to the assumption that the olivine crystal is an infinite domain, which requires the melt inclusion to be sufficiently small not to feel far field effects. If the inclusion is large relative to the crystal, and it is situated close to the edge along the [100] axis, then the analytical model will underestimate water loss.

The anisotropic analytical solution and 1D numerical models could offer complementary ways to obtain magma decompression rates for different olivine-melt inclusion configurations that retain some fidelity to the 3D numerical solution but are also computationally more efficient. If the melt inclusion is close to the centre of the crystal and is small relative to the the compahost then the analytical solution (Equation (14)) could be used to extract decompression rates within a factor of 2. Conversely, if the melt inclusion is situated close to the crystal edge along the [100] axis, then the 1D approximations (with our empirical correction) could offer an accurate solution. 2D inversions could offer a solution that could be applied over a much wider range of geometrical configurations, provided the effects of diffusion along the third dimension can be mitigated. However, 2D models are more computationally intensive.

5.4 The role of multiple melt inclusions in controlling water loss or gain

Most attempts to model water loss from melt inclusions assume that the olivine contains a single melt inclusion located in the centre of the crystal (Qin et al., 1992; Chen et al., 2013; Bucholz et al., 2013). This has primarily been done to simplify the modelling (e.g., radial analytical or numerical solutions), and could reliably be applied to natural systems in some instances (Gaetani et al., 2012; Chen et al., 2013; Barth et al., 2019). Many natural olivine crystals, however, can contain multiple melt inclusions with different sizes and configurations (Wallace et al., 2021). This depends on the growth history of the olivine, which may undergo periods of crystal growth, resorption and regrowth (Wallace et al., 2021). Rapid dendritic growth induced by high degrees of undercooling to form skeletal or hopper crystals followed by slow maturation of crystal faces can cause melt inclusion entrapment (Faure et al., 2003; Welsch et al., 2014; Mourey & Shea, 2019). Alternatively, melt inclusions can form as a result of irregular growth due to the attachment of small phases (e.g., spinel) to the surface of the crystal, or from the sealing off

of melt embayments formed by partial resorption (Roedder, 1979). Combinations of these processes mean that some crystals can contain hundreds of melt and fluid inclusions (Métrich & Wallace, 2008; Wallace et al., 2021).

Given the diversity of melt inclusion configurations observed in the crystal cargoes of single eruptions (Wallace et al., 2021), it is therefore important to be able to understand water loss or gain from olivine crystals that contain multiple melt inclusions. This may be critical for getting a representative view of the crystallisation and decompression history of a given magma or volcanic system. The 3D multi-phase finite element model that we have developed as part of this study allows us to incorporate multiple melt inclusions in order to understand their interaction during magma ascent. Here, we ran additional forward models to compare water loss from olivine crystals that contained a single central spherical melt inclusion with models in which this central inclusion is surrounded by 18 other spherical melt inclusions (Figure 10). Three variations of the models were run where we varied the size of central melt inclusion (radius of 25, 50 and 75 µm). The size of the surrounding melt inclusions were fixed with a radius of 50 µm. The crystal size (695 µm along the [001] axis from the centre of the crystal), the olivine-melt parition coefficient (0.000459), initial water content (4.2 wt%), final matrix glass water content (0.3 wt%) were fixed for representative values for the 1977 eruption of Seguam. Decompression rate was varied from 0.001 to 0.8 MPa s^{-1}. To assess the role of diffusive anisotropy in olivine on melt inclusion interaction, we ran additional models that compare water loss from a single 25 µm single central melt inclusion with models in which there is an additional 75 µm inclusion positioned along one of the principle crystallographic ([100], [010] and [001]). All of these model configurations were run with different anisotropies (3.0, 15.6, 35.0) and decompression rates.

Our models show that the addition of multiple melt inclusions could have a large effect on melt inclusion water loss during magma decompression. Isolated melt inclusions (i.e. a single melt inclusion in a crystal) can lose more water during magma ascent than melt inclusions that are adjacent to or are surrounded by neighbouring inclusions (Figure 12). This difference can range from 0.5 wt% to over 1.5 wt% depending on melt inclusion size and configuration. 3D model results show that the 'haloes' of elevated water content surrounding the melt inclusions overlap and interact (Figures 10 and 11). Our results demonstrate that large melt inclusions are able to buffer water loss from adjacent small melt inclusions, and clusters of melt inclusions are able to 'shield' each other from the effects of diffusive water loss in response to degassing of the host magma. Furthermore as the water content of the melt inclusions drop (particularly for low decompression rates), the diffusivity of water in the melt could potentially decrease to below that of the olivine along the fast [100] direction. Hence the melt inclusions could act as a slower pathway for water to escape.

The effect that multiple melt inclusions have on water loss appears to also depend on both decompression rate and melt inclusion size (Figure 12). Figure 12a shows that the difference in water loss from the central melt inclusion between models that contain single and multiple melt inclusions for a given crystal size has a near-Gaussian distribution with a peak at decompression rates around 0.001 to 0.01 MPa s^{-1}. This likely relates to the amount of time in which diffusion is allowed to operate. At high decompression rates, there is insufficient time for diffusion to remove water from the central melt inclusion in either model scenario (i.e. the diffusion fronts have not approached the centre of the crystal). Meanwhile at low decompression rates, there is plenty of time for diffusion to occur meaning the central melt inclusion is close to equilibrium for both model scenarios upon eruption. For melt inclusion shielding to reach full effect, the magma needs to be ascending at a rate in which diffusion has sufficient time to operate, but also for disequilibrium to maintained. This would occupy the speedometer domain described by Barth and Plank (2021).

The size of the shielding effect is sensitive to melt inclusion size (Figure 12). The difference in water loss from the central melt inclusion is greater if it has a smaller radius. This is because smaller melt inclusions are more sensitive to water loss. The shielding effect is more pronounced in larger central melt inclusion models (50-75 μm radius) that were run using low anistropies (3.0). This is because in these models the crystal loses more water because diffusivity along the [010] and [001] is faster meaning the larger melt inclusions can be more sensitive to water loss. Given the greater utility of smaller melt inclusions in ascent rate speedometry, knowing about potential shielding effects from nearby melt inclusions is even more important.

The position of melt inclusions can also have a major impact on water loss or gain via the shielding effect, particularly with regards to diffusive anisotropy in olivine. This is highlighted in Figure 12b, which shows how 75 μm melt inclusions positioned along different crystallograpic axes influence water loss from a 25 μm central melt inclusion. This effect is also considered for different anisotropies (3.0, 15.6 and 35.0). The larger melt inclusion inhibits water loss along the direction in which it is positioned. The shielding effect is therefore most pronounced when the melt inclusion is situated along the [100] axes, where diffusion is fastest. Differences in water loss based on inclusion location along crystalloraphic axes is further accentuated by diffusive anisotropy. In models with low diffusive anisotropy (3.0), the difference in water loss when the large inclusion is situated along [100] is lower, whilst the differences are higher when the large inclusion is situated along the [010] and [001] axes when compared to higher anisotropy models. This is because water can diffuse faster along the other directions that do not contain the melt inclusion, and thus diffusive flux out of the crystal is less dependent on a single crystallographic direction. In the high anisotropy models (15.6, 35.0), the size of the shielding effect along [100] is significantly greater than along [010] and [001]. The peak shielding effect associated with [100] is on the order of 1.0 wt%, whilst the effect along [010] and [001] is almost negligible. This is because water loss in these models will dominantly take place along [100]. Therefore shielding melt inclusions situated along [100] will have a larger impact on total flux. Differences in the shielding effect along [010] and [001] are difficult to resolve given the uncertainties in the model.

Our models may be extreme examples, particularly with regards to melt inclusion sizes, but they do highlight the importance of considering multiple melt inclusions for magmatic applications. For hygrometry, melt inclusions that are surrounded by other melt inclusions, particularly along the [100] direction, may provide more faithful estimates of initial water content provided the crystal has not undergone complete equilibration. For speedometry, it may be crucial to incorporate multiple melt inclusions in modelling if they are situated in the same plane along the fast direction.

5.5 Caveats and Complexities

The diffusion models in this study are simplified and based on a series of approximations and assumptions. This approach may be sufficient for understanding how melt inclusion interaction and geometry may impact water loss or gain during simple ascent histories, however it may not completely capture complexities that are observed in natural systems.

Firstly, we assume that the water content of the melt inclusion is solely controlled by diffusive loss through the host olivine during decompression. Furthermore, the melt inclusion maintains a fixed volume. Our models predict that there should be water zoning within the melt inclusion that occurs in response to this process. In reality, there are additional processes that can modify melt inclusion water content and volume upon ascent including vapour bubble growth and post entrapment crystallisation. Water may partition into a growing vapour bubble during the final stages of decompression, meaning it may be unaccounted for if the bubble composition is not measured. Water gra-

dients may develop around vapour bubbles and likely mark the complexities associated with water diffusing into the host crystal and the vapour bubble, which maybe further be compounded by the bubble moving around in the inclusion. As the magma ascends to the surface, changes in P-T conditions may affect phase stability and cause crystallisation or dissolution on the melt inclusion walls, which may in turn cause the size of the inclusion to change and for the concentration of water in the melt inclusion to increase or decrease. This process will depend highly on the magma composition and the ascent history, and could potentially be reconstructed by looking at cooling histories of melt inclusions (Newcombe, Plank, Zhang, et al., 2020). Thermal history modelling applied to MgO profiles measured in Seguam olivine hosted melt inclusions suggests they did not undergo any net cooling upon ascent and that any growth on the inclusion walls was likely quench crystallisation (Newcombe, Plank, Zhang, et al., 2020).

Secondly, the choice of H-in-olivine diffusion coefficient is also associated with significant caveats. We applied the diffusion coefficient of Barth et al. (2019) in our models because their experiments were conducted on olivine compositions that most closely resemble those from the 1977 Seguam eruption. The Arrhenius relationship of Barth et al. (2019) is based on two data points, and needs to be characterised at more temperatures. Extrapolation beyond these conditions introduces further uncertainty given that the exact dependence of bulk H^+ diffusivity on olivine composition has yet to be properly quantified (Barth & Plank, 2021). Iron content has been shown to play a major role (Barth et al., 2019, 2023), but the concentration of trace elements and water itself could be important (Tollan et al., 2018; Jollands et al., 2019). Lithium has shown the potential to couple with trace element zoning patterns, most notably phosphorus (Lynn et al., 2020); H^+ could show similar behaviour. Consideration of intersite reaction and the changing availability of defects may also be important despite simple Arrhenius approximations for bulk H^+ diffusion (Ferriss et al., 2018; Jollands et al., 2019). Reaction rates and site availability for defects can change over time, meaning diffusivity could change as dehydration progresses (Ferriss et al., 2018). There is also still considerable uncertainty associated with diffusive anisotropy, due to discrepancies observed between dehydration experiments (Ferriss et al., 2018; Barth et al., 2019) and observations made in some natural crystals. Experimental observations, and some of our 2D inversions indicate high anisotropies (10–40) whilst melt inclusion-free crystals from Seguam do not appear to show evidence of high anisotropy, with estimated values of 2–3 (Newcombe, Plank, Barth, et al., 2020). It is unclear what could cause this discrepancy. Barth and Plank (2021) suggest that the conditions under which dehydration experiments are conducted may not fully replicate the processes that occur in nature. Alternatively, limitations in analytical precision, drift and spatial resolution (particularly along the slow directions), along with trace element coupling may generate profiles with apparent high or low anisotropy. It is clear, that to improve the accuracy of our modelling methods to a wider range of applications, considerations of the appropriate diffusion mechanism and defect structure need to be made.

Thirdly, the partition coefficient of water between the melt and olivine can exert a large control on water loss and the shape of diffusion of bulk H^+ profiles in olivine. We have assumed a constant partition coefficient based on measured profiles in natural Seguam crystals. Different incorporation mechanisms have been suggested for H^+ in olivine that may dominate under different P-T conditions and mineral compositions (Danyushevsky et al., 2002; Gaetani et al., 2012; Portnyagin et al., 2019; Barth & Plank, 2021). If this were indeed the case, the partition coefficient would be continually changing along the decompression pathway.

Fourthly, assumptions have been made in the modelling about the style of magma ascent and degassing which may not be appropriate to some natural systems. We assumed a linear decompression rate and equilibrium closed-system degassing as an external boundary condition. Linear decompression is considered to be a good first pass approximation

for constraining average decompression rates for different eruptions (Barth & Plank, 2021), however magma decompression is expected to be highly non-linear (Gonnermann & Manga, 2007; Su & Huber, 2017; Barth et al., 2019; Hajimirza et al., 2021). Exsolution of water and subsequent nucleation and growth of bubbles at shallow depth increases the buoyancy of the magma and drives acceleration (Gonnermann & Manga, 2007). Further changes in magma viscosity due to crystallisation and water loss, in addition to friction along the conduit wall may need to be considered. Models that assume a constant decompression rate can underestimate the total ascent time because more time has to be spent at depth in order to compensate for the reduced amount of time in at shallow depths where most water loss takes place (Barth et al., 2019; Barth & Plank, 2021; Hajimirza et al., 2021). The degree of non-linearity would need to be known *a priori*, potentially from the predictions of conduit models, in order to constrain faithful ascent timescales. The assumption of equilibrium degassing may be acceptable for basaltic systems, where bubble nucleation is not necessarily inhibited by the low viscosities. For systems with higher viscosities, such as andesites and rhyolites, consideration of disequilibrium degassing may be more important. deGraffenried and Shea (2021) showed that this is the case for modelling decompression rates from melt embayments in quartz crytals in rhyolitic systems. For simple decompression histories in basaltic systems, the assumption of closed system degassing is also reasonable because the growing vapour bubbles are unlikely to segregate from the ascending melt unless they they reach a critical radius (Vergniolle & Jaupart, 1986). If the ascent history includes minor stalling periods, then there may be sufficient time for bubbles to segregate from the magma. These stalling periods, however are also likely to be recorded by re-equilibration of water in the crystal and melt inclusion record.

Finally, some of our modelling approach makes some simplifying geometrical assumptions. For our 3D models, we have assumed that the melt inclusions are spherical and that the host olivine has an idealised morphology based on the forms of Welsch et al. (2014). Even though these approximations are better than previous modelling efforts (Le Voyer et al., 2014; Newcombe, Plank, Barth, et al., 2020), natural melt inclusions and olivine crystals can take different morphologies, which will depend on the mechanisms of entrapment and crystal growth (Wallace et al., 2021). Olivine crystals can take a range of forms from blocky, to skeletal and hopper crystals, which depends on the degree of undercooling and growth rates (Mourey & Shea, 2019). Melt inclusions can also take ellipsoidal forms, which could depend on the minimisation of surface tension (Wallace et al., 2021). Our models also assume that crystal and melt inclusion morphology remain constant during ascent. This may not necessarily be the case due to crystal growth, resorption, attrition and fracture.

6 Conclusions

Measuring and modelling water loss from olivine hosted melt inclusions play a crucial role in understanding the evolution of magmatic systems from the mantle to the surface. This includes estimating the water content of primary mantle melts, estimating magma storage depths in combination with other volatile species (e.g., CO_2), and understanding and timing processes associated with final magma ascent. Most attempts at modelling water loss from olivine melt inclusions apply simplifying assumptions associated with crystal and melt inclusion geometrical configurations, such as spherical or 1D models.

Here we have developed a new finite element 3D multiphase diffusion model that accounts for water loss from both olivine and melt inclusion. This model uses an idealised olivine crystal morphology and can include multiple melt inclusions. We used this model to assess the accuracy of simplified model configurations including 1D models with symmetric and asymmetric crystal geometries around the melt inclusion, 2D models sectioned through (010) and (001), and an anisotropic analytical solution that can be applied in

an infinite domain. We find that the 1D, 2D and analytical models generally underestimate the amount of water loss from melt inclusions compared to the 3D models. These models also underestimate decompression rates compared to the 3D models. This is because additional water is lost along the additional dimensions that are not accounted for, or in the case of the analytical solution, the melt inclusion geometry falls outside the limits in which the solution is valid. The amount in which these models underestimate water loss and decompression rate depend on the position of the melt inclusion along the [100] axes, inclusion size and the sectional cut of the crystal. If the melt inclusion is located close to the crystal edge along [100], water loss and decompression rate predictions from 1D models closely match those from the 3D models, because overestimations in diffusive flux out of the melt inclusion counter balance the extra water loss from the unaccounted dimensions. We developed an empirical correction that aligns predictions from 1D models closer to those from the 3D models. If the inclusion is small relative to the host and is situated away from the edge of the crystal, the anisotropic analytical solutions that we present provide an accurate and computationally efficient way of determining water loss and decompression rate.

We also developed 3D models that include multiple melt inclusions in order to replicate some crystals found in nature. We find that melt inclusions shield each other and reduce the amount of water loss when compared to crystals that only contain a single melt inclusion. This shielding effect depends on decompression rate, the size of the melt inclusions, and is enhanced if the melt inclusions are situated along the [100] direction. Crystals with dense populations of melt inclusions may therefore provide a more reliable estimate of magmatic water contents prior to ascent driven degassing.

Two dimensional models may offer a compromise for providing accurate solutions at a wider range of crystal shape and melt inclusion configurations. This approach can also account for multiple melt inclusions if they are in the same 2D plane. We applied 2D inversion models to measured water profiles in olivine crystals from the 1977 eruption of Seguam. This approach generates median decompression rates of $0.07 - 0.36 \pm 0.04$ MPa s^{-1}, which is consistent with previous estimates, and likely represents natural variability in final magma ascent rates. Our modelling approach has shown that factors such 3D crystal geometry and the configuration of melt inclusion populations can play an important role in constraining accurate decompression rates, and for recovering water contents in natural magmatic systems.

Open Research Section

Acknowledgments

References

Alnæs, M., Blechta, J., Hake, J., Johansson, A., Kehlet, B., Logg, A., . . . Wells, G. N. (2015). The FEniCS project version 1.5. *Archive of Numerical Software*, *3*(100), 9–23.

Balay, S., Abhyankar, S., Adams, M., Brown, J., Brune, P., Buschelman, K., . . . others (2019). Petsc users manual.

Barth, A., Newcombe, M., Plank, T., Gonnermann, H., Hajimirza, S., Soto, G. J., . . . Hauri, E. (2019). Magma decompression rate correlates with explosivity at basaltic volcanoes—constraints from water diffusion in olivine. *Journal of Volcanology and Geothermal Research*, *387*, 106664.

Barth, A., & Plank, T. (2021). The Ins and Outs of Water in Olivine-Hosted Melt Inclusions: Hygrometer vs. Speedometer. *Frontiers in Earth Science*, *9*, 343.

Barth, A., Plank, T., & Towbin, H. (2023). Rates of dehydration in hydrous, high-fo, magmatic olivines. *Geochimica et Cosmochimica Acta*, *342*, 62–73.

Bell, D. R., Rossman, G. R., Maldener, J., Endisch, D., & Rauch, F. (2003). Hydroxide in olivine: A quantitative determination of the absolute amount and calibration of the IR spectrum. *Journal of Geophysical Research: Solid Earth*, *108*(B2).

Bradshaw, R. W., & Kent, A. J. (2017). The analytical limits of modeling short diffusion timescales. *Chemical Geology*, *466*, 667–677.

Buchner, J., Georgakakis, A., Nandra, K., Hsu, L., Rangel, C., Brightman, M., . . . Kocevski, D. (2014). X-ray spectral modelling of the AGN obscuring region in the CDFS: Bayesian model selection and catalogue. *Astronomy & Astrophysics*, *564*, A125.

Bucholz, C. E., Gaetani, G. A., Behn, M. D., & Shimizu, N. (2013). Post-entrapment modification of volatiles and oxygen fugacity in olivine-hosted melt inclusions. *Earth and Planetary Science Letters*, *374*, 145–155.

Cashman, K., & Blundy, J. (2000). Degassing and crystallization of ascending andesite and dacite. *Philosophical Transactions of the Royal Society of London. Series A: Mathematical, Physical and Engineering Sciences*, *358*(1770), 1487–1513.

Cassidy, M., Castro, J. M., Helo, C., Troll, V. R., Deegan, F. M., Muir, D., . . . Mueller, S. P. (2016). Volatile dilution during magma injections and implications for volcano explosivity. *Geology*, *44*(12), 1027–1030.

Chen, Y., Provost, A., Schiano, P., & Cluzel, N. (2011). The rate of water loss from olivine-hosted melt inclusions. *Contributions to Mineralogy and Petrology*, *162*(3), 625–636.

Chen, Y., Provost, A., Schiano, P., & Cluzel, N. (2013). Magma ascent rate and initial water concentration inferred from diffusive water loss from olivine-hosted melt inclusions. *Contributions to Mineralogy and Petrology*, *165*(3), 525–541.

Cottrell, E., Spiegelman, M., & Langmuir, C. (2002). Consequences of diffusive reequilibration for the interpretation of melt inclusions. *Geochemistry, Geophysics, Geosystems*, *3*(4), 1–26.

Couperthwaite, F., Thordarson, T., Morgan, D., Harvey, J., & Wilson, M. (2020). Diffusion timescales of magmatic processes in the moinui lava eruption at mauna loa, hawaii, as inferred from bimodal olivine populations. *Journal of Petrology*, *61*(7), egaa058.

Danyushevsky, L. V., Sokolov, S., & Falloon, T. J. (2002). Melt inclusions in olivine phenocrysts: using diffusive re-equilibration to determine the cooling history of a crystal, with implications for the origin of olivine-phyric volcanic rocks. *Journal of Petrology*, *43*(9), 1651–1671.

deGraffenried, R., & Shea, T. (2021). Using Volatile Element Concentration Profiles in Crystal-Hosted Melt Embayments to Estimate Magma Decompression Rate: Assumptions and Inherited Errors. *Geochemistry, Geophysics, Geosystems*, *22*(5), e2021GC009672.

Dingwell, D. B. (1996). Volcanic Dilemma–Flow or Blow? *Science*, *273*(5278), 1054–1055.

Dohmen, R., & Chakraborty, S. (2007). Fe–Mg diffusion in olivine II: point defect chemistry, change of diffusion mechanisms and a model for calculation of diffusion coefficients in natural olivine. *Physics and Chemistry of Minerals*, *34*(6), 409–430.

Faure, F., Trolliard, G., Nicollet, C., & Montel, J.-M. (2003). A developmental model of olivine morphology as a function of the cooling rate and the degree of undercooling. *Contributions to Mineralogy and Petrology*, *145*(2), 251–263.

Ferguson, D. J., Gonnermann, H. M., Ruprecht, P., Plank, T., Hauri, E. H., Houghton, B. F., & Swanson, D. A. (2016). Magma decompression rates during explosive eruptions of Kīlauea volcano, Hawaii, recorded by melt embayments. *Bulletin of Volcanology*, *78*(10), 71.

Feroz, F., Hobson, M., & Bridges, M. (2009). MultiNest: an efficient and robust Bayesian inference tool for cosmology and particle physics. *Monthly Notices of the Royal Astronomical Society*, *398*(4), 1601–1614.

Ferriss, E., Plank, T., Newcombe, M., Walker, D., & Hauri, E. (2018). Rates of dehydration of olivines from San Carlos and Kilauea Iki. *Geochimica et Cosmochimica Acta*, *242*, 165–190.

Gaetani, G. A., Grove, T. L., & Bryan, W. B. (1993). The influence of water on the petrogenesis of subductionrelated igneous rocks. *Nature*, *365*(6444), 332–334.

Gaetani, G. A., O'Leary, J. A., Shimizu, N., Bucholz, C. E., & Newville, M. (2012). Rapid reequilibration of H_2O and oxygen fugacity in olivine-hosted melt inclusions. *Geology*, *40*(10), 915–918.

Geuzaine, C., & Remacle, J.-F. (2017). *Gmsh.* Retrieved from `http://http://gmsh.info/`

Gonnermann, H. M., & Manga, M. (2007). The fluid mechanics inside a volcano. *Annu. Rev. Fluid Mech.*, *39*, 321–356.

Grove, T. L., Chatterjee, N., Parman, S. W., & Médard, E. (2006). The influence of H_2O on mantle wedge melting. *Earth and Planetary Science Letters*, *249*(1-2), 74–89.

Grove, T. L., Till, C. B., & Krawczynski, M. J. (2012). The role of H_2O in subduction zone magmatism. *Annual Review of Earth and Planetary Sciences*, *40*, 413–439.

Gurioli, L., Houghton, B. F., Cashman, K. V., & Cioni, R. (2005). Complex changes in eruption dynamics during the 79 AD eruption of Vesuvius. *Bulletin of Volcanology*, *67*(2), 144–159.

Hajimirza, S., Gonnermann, H. M., & Gardner, J. E. (2021). Reconciling bubble nucleation in explosive eruptions with geospeedometers. *Nature communications*, *12*(1), 1–8.

Hartley, M. E., Neave, D. A., Maclennan, J., Edmonds, M., & Thordarson, T. (2015). Diffusive over-hydration of olivine-hosted melt inclusions. *Earth and Planetary Science Letters*, *425*, 168–178.

Hauri, E. (2002). SIMS analysis of volatiles in silicate glasses, 2: isotopes and abundances in hawaiian melt inclusions. *Chemical Geology*, *183*(1-4), 115–141.

Hauri, E. H., Gaetani, G. A., & Green, T. H. (2006). Partitioning of water during melting of the Earth's upper mantle at H_2O-undersaturated conditions. *Earth and Planetary Science Letters*, *248*(3-4), 715–734.

Jicha, B. R., & Singer, B. S. (2006). Volcanic history and magmatic evolution of Seguam Island, Aleutian Island arc, Alaska. *Geological Society of America Bulletin*, *118*(7-8), 805–822.

Jollands, M. C., Kempf, E., Hermann, J., & Müntener, O. (2019). Coupled inter-site reaction and diffusion: Rapid dehydrogenation of silicon vacancies in natural olivine. *Geochimica et Cosmochimica Acta*, *262*, 220–242.

Kahl, M., Mutch, E., Maclennan, J., Morgan, D., Couperthwaite, F., Bali, E., . . .

others (2023). Deep magma mobilization years before the 2021 ce fagradalsfjall eruption, iceland. *Geology*, *51*(2), 184–188.

Koga, K., Hauri, E., Hirschmann, M., & Bell, D. (2003). Hydrogen concentration analyses using SIMS and FTIR: comparison and calibration for nominally anhydrous minerals. *Geochemistry, Geophysics, Geosystems*, *4*(2).

Kohlstedt, D. L., & Mackwell, S. J. (1998). Diffusion of hydrogen and intrinsic point defects in olivine. *Zeitschrift für physikalische Chemie*, *207*(1-2), 147–162.

Kumamoto, K. M., Warren, J. M., & Hauri, E. H. (2017). New SIMS reference materials for measuring water in upper mantle minerals. *American Mineralogist*, *102*(3), 537–547.

Le Voyer, M., Asimow, P. D., Mosenfelder, J. L., Guan, Y., Wallace, P. J., Schiano, P., . . . Eiler, J. M. (2014). Zonation of H_2o and F concentrations around melt inclusions in olivines. *Journal of Petrology*, *55*(4), 685–707.

Lloyd, A. S., Ferriss, E., Ruprecht, P., Hauri, E. H., Jicha, B. R., & Plank, T. (2016). An assessment of clinopyroxene as a recorder of magmatic water and magma ascent rate. *Journal of Petrology*, *57*(10), 1865–1886.

Long, G. L., & Winefordner, J. D. (1983). Limit of detection. A closer look at the IUPAC definition. *Analytical chemistry*, *55*(7), 712A–724A.

Lynn, K. J., Garcia, M. O., & Shea, T. (2020). Phosphorus coupling obfuscates lithium geospeedometry in olivine. *Frontiers in Earth Science*, *8*, 135.

Lynn, K. J., Shea, T., Garcia, M. O., Costa, F., & Norman, M. D. (2018). Lithium diffusion in olivine records magmatic priming of explosive basaltic eruptions. *Earth and Planetary Science Letters*, *500*, 127–135.

Lynn, K. J., & Warren, J. M. (2021). The potential for aqueous fluid-rock and silicate melt-rock interactions to re-equilibrate hydrogen in peridotite nominally anhydrous minerals. *American Mineralogist: Journal of Earth and Planetary Materials*, *106*(5), 701–714.

Mackwell, S. J., & Kohlstedt, D. L. (1990). Diffusion of hydrogen in olivine: implications for water in the mantle. *Journal of Geophysical Research: Solid Earth*, *95*(B4), 5079–5088.

Maclennan, J. (2017). Bubble formation and decrepitation control the CO_2 content of olivine-hosted melt inclusions. *Geochemistry, Geophysics, Geosystems*, *18*(2), 597–616.

McCormick-Kilbride, B., Edmonds, M., & Biggs, J. (2016). Observing eruptions of gas-rich compressible magmas from space. *Nature Communications*, *7*(1), 1–8.

Métrich, N., & Wallace, P. J. (2008). Volatile abundances in basaltic magmas and their degassing paths tracked by melt inclusions. *Reviews in mineralogy and geochemistry*, *69*(1), 363–402.

Miller, T. P., McGimsey, R., Richter, D., Riehle, J., Nye, C., Yount, M., & Dumoulin, J. A. (1998). *Catalog of the historically active volcanoes of Alaska*. United States Department of the Interior, United States Geological Survey.

Moore, L. R., Gazel, E., Tuohy, R., Lloyd, A. S., Esposito, R., Steele-MacInnis, M., . . . Bodnar, R. J. (2015). Bubbles matter: An assessment of the contribution of vapor bubbles to melt inclusion volatile budgets. *American Mineralogist*, *100*(4), 806–823.

Mosenfelder, J. L., Le Voyer, M., Rossman, G. R., Guan, Y., Bell, D. R., Asimow, P. D., & Eiler, J. M. (2011). Analysis of hydrogen in olivine by SIMS: Evaluation of standards and protocol. *American Mineralogist*, *96*(11-12), 1725–1741.

Mourey, A. J., & Shea, T. (2019). Forming olivine phenocrysts in basalt: a 3D characterization of growth rates in laboratory experiments. *Frontiers in Earth Science*, 300.

Moussallam, Y., Rose-Koga, E. F., Koga, K. T., Médard, E., Bani, P., Devidal, J.-L., & Tari, D. (2019). Fast ascent rate during the 2017–2018 Plinian eruption of Ambae (Aoba) volcano: a petrological investigation. *Contributions to Mineralogy and Petrology*, *174*(11), 1–24.

Müller, T., Dohmen, R., Becker, H., Ter Heege, J. H., & Chakraborty, S. (2013). Fe–Mg interdiffusion rates in clinopyroxene: experimental data and implications for Fe–Mg exchange geothermometers. *Contributions to Mineralogy and Petrology*, *166*(6), 1563–1576.

Mutch, E. J. F., Maclennan, J., Holland, T. J. B., & Buisman, I. (2019). Millennial storage of near-moho magma. *Science*, *365*(6450), 260-264. Retrieved from https://www.science.org/doi/abs/10.1126/science.aax4092 doi: http://dx.doi.org/10.1126/science.aax4092doi:10.1126/science.aax4092

Mutch, E. J. F., Maclennan, J., Shorttle, O., Edmonds, M., & Rudge, J. F. (2019). Rapid transcrustal magma movement under Iceland. *Nature Geoscience*, *12*(7), 569–574. Retrieved from https://doi.org/10.1038/s41561-019-0376-9 doi: http://dx.doi.org/10.1038/s41561-019-0376-9doi:10.1038/s41561-019-0376-9

Mutch, E. J. F., Maclennan, J., Shorttle, O., Rudge, J. F., & Neave, D. A. (2021). DFENS: Diffusion Chronometry Using Finite Elements and Nested Sampling. *Geochemistry, Geophysics, Geosystems*, *22*(4), e2020GC009303. Retrieved from https://agupubs.onlinelibrary.wiley.com/doi/abs/10.1029/2020GC009303 (e2020GC009303 2020GC009303) doi: http://dx.doi.org/https://doi.org/10.1029/2020GC009303doi:https://doi.org/10.1029/2020GC009303

Myers, M. L., Druitt, T. H., Schiavi, F., Gurioli, L., & Flaherty, T. (2021). Evolution of magma decompression and discharge during a Plinian event (Late Bronze-Age eruption, Santorini) from multiple eruption-intensity proxies. *Bulletin of Volcanology*, *83*(3), 1–17.

Myers, M. L., Wallace, P. J., & Wilson, C. J. (2019). Inferring magma ascent timescales and reconstructing conduit processes in explosive rhyolitic eruptions using diffusive losses of hydrogen from melt inclusions. *Journal of Volcanology and Geothermal Research*, *369*, 95–112.

Neave, D. A., & Maclennan, J. (2020). Clinopyroxene dissolution records rapid magma ascent. *Frontiers in Earth Science*, *8*, 188.

Neukampf, J., Ellis, B., Laurent, O., Steinmann, L., Ubide, T., Oeser, M., ... Bachmann, O. (2021). Time scales of syneruptive volatile loss in silicic magmas quantified by Li isotopes. *Geology*, *49*(2), 125–129.

Newcombe, M. E., Plank, T., Barth, A., Asimow, P. D., & Hauri, E. (2020). Water-in-olivine magma ascent chronometry: every crystal is a clock. *Journal of Volcanology and Geothermal Research*, *398*, 106872.

Newcombe, M. E., Plank, T., Zhang, Y., Holycross, M., Barth, A., Lloyd, A. S., ... Hauri, E. (2020). Magma pressure-temperature-time paths during mafic explosive eruptions. *Frontiers in Earth Science*, *8*, 378.

Newman, S., & Lowenstern, J. B. (2002). VolatileCalc: a silicate melt–H_2O–CO_2 solution model written in Visual Basic for excel. *Computers & Geosciences*, *28*(5), 597–604.

Ni, H., & Zhang, L. (2018). A general model of water diffusivity in calc-alkaline silicate melts and glasses. *Chemical Geology*, *478*, 60–68.

Padrón-Navarta, J. A., Hermann, J., & O'Neill, H. S. C. (2014). Site-specific hydrogen diffusion rates in forsterite. *Earth and Planetary Science Letters*, *392*, 100–112.

Peslier, A. H., Bizimis, M., & Matney, M. (2015). Water disequilibrium in olivines from Hawaiian peridotites: Recent metasomatism, H diffusion and magma ascent rates. *Geochimica et Cosmochimica Acta*, *154*, 98–117.

Peslier, A. H., & Luhr, J. F. (2006). Hydrogen loss from olivines in mantle xenoliths from Simcoe (USA) and Mexico: Mafic alkalic magma ascent rates and water budget of the sub-continental lithosphere. *Earth and Planetary Science Letters*, *242*(3-4), 302–319.

Portnyagin, M., Mironov, N., Botcharnikov, R., Gurenko, A., Almeev, R. R., Luft,

1226 C., & Holtz, F. (2019). Dehydration of melt inclusions in olivine and im-
1227 plications for the origin of silica-undersaturated island-arc melts. *Earth and*
1228 *Planetary Science Letters*, *517*, 95–105.

1229 Qin, Z., Lu, F., & Anderson, A. T. (1992). Diffusive reequilibration of melt and fluid
1230 inclusions. *American Mineralogist*, *77*(5-6), 565–576.

1231 Rae, A. S., Edmonds, M., Maclennan, J., Morgan, D., Houghton, B., Hartley, M. E.,
1232 & Sides, I. (2016). Time scales of magma transport and mixing at Kīlauea
1233 volcano, Hawai'i. *Geology*, *44*(6), 463–466.

1234 Rasmussen, D. J., Plank, T. A., Roman, D. C., Power, J. A., Bodnar, R. J., &
1235 Hauri, E. H. (2018). When does eruption run-up begin? Multidisciplinary
1236 insight from the 1999 eruption of Shishaldin volcano. *Earth and Planetary*
1237 *Science Letters*, *486*, 1–14.

1238 Rasmussen, D. J., Plank, T. A., Roman, D. C., & Zimmer, M. M. (2022). Mag-
1239 matic water content controls the pre-eruptive depth of arc magmas. *Science*,
1240 *375*(6585), 1169–1172.

1241 Rasmussen, D. J., Plank, T. A., Wallace, P. J., Newcombe, M. E., & Lowenstern,
1242 J. B. (2020). Vapor-bubble growth in olivine-hosted melt inclusions. *American*
1243 *Mineralogist: Journal of Earth and Planetary Materials*, *105*(12), 1898–1919.

1244 Roedder, E. (1979). Origin and significance of magmatic inclusions. *Bulletin de Min-*
1245 *eralogie*, *102*(5), 487–510.

1246 Russell, J. K., Giordano, D., Dingwell, D. B., & Hess, K.-U. (2002). Modelling the
1247 non-Arrhenian rheology of silicate melts: Numerical considerations. *European*
1248 *Journal of Mineralogy*, *14*(2), 417–427.

1249 Ruth, D., Costa, F., Bouvet de Maisonneuve, C., Franco, L., Cortés, J. A., &
1250 Calder, E. S. (2018). Crystal and melt inclusion timescales reveal the evo-
1251 lution of magma migration before eruption. *Nature Communications*, *9*(1),
1252 1–9.

1253 Schindelin, J., Arganda-Carreras, I., Frise, E., Kaynig, V., Longair, M., Pietzsch, T.,
1254 . . . others (2012). Fiji: an open-source platform for biological-image analysis.
1255 *Nature methods*, *9*(7), 676.

1256 Shea, T., Costa, F., Krimer, D., & Hammer, J. E. (2015). Accuracy of timescales re-
1257 trieved from diffusion modeling in olivine: A 3D perspective. *American Miner-*
1258 *alogist*, *100*(10), 2026–2042.

1259 Shea, T., Houghton, B. F., Gurioli, L., Cashman, K. V., Hammer, J. E., & Hobden,
1260 B. J. (2010). Textural studies of vesicles in volcanic rocks: an integrated
1261 methodology. *Journal of Volcanology and Geothermal Research*, *190*(3-4),
1262 271–289.

1263 Sobolev, A. V., & Chaussidon, M. (1996). H_2O concentrations in primary melts
1264 from supra-subduction zones and mid-ocean ridges: implications for H_2O
1265 storage and recycling in the mantle. *Earth and Planetary Science Letters*,
1266 *137*(1-4), 45–55.

1267 Steele-Macinnis, M., Esposito, R., & Bodnar, R. J. (2011). Thermodynamic model
1268 for the effect of post-entrapment crystallization on the H_2O–CO_2 systemat-
1269 ics of vapor-saturated, silicate melt inclusions. *Journal of Petrology*, *52*(12),
1270 2461–2482.

1271 Stock, M. J., Humphreys, M., Smith, V. C., Isaia, R., & Pyle, D. M. (2016). Late-
1272 stage volatile saturation as a potential trigger for explosive volcanic eruptions.
1273 *Nature Geoscience*, *9*(3), 249–254.

1274 Su, Y., & Huber, C. (2017). The effect of nonlinear decompression history on
1275 H_2O/CO_2 vesiculation in rhyolitic magmas. *Journal of Geophysical Research:*
1276 *Solid Earth*, *122*(4), 2712–2723.

1277 Sugawara, T. (2000). Empirical relationships between temperature, pressure, and
1278 MgO content in olivine and pyroxene saturated liquid. *Journal of Geophysical*
1279 *Research: Solid Earth*, *105*(B4), 8457–8472.

1280 Till, C. B., Grove, T. L., & Withers, A. C. (2012). The beginnings of hydrous

mantle wedge melting. *Contributions to Mineralogy and Petrology*, *163*(4), 669–688.

Tollan, P. M., O'Neill, H. S. C., & Hermann, J. (2018). The role of trace elements in controlling H incorporation in San Carlos olivine. *Contributions to mineralogy and petrology*, *173*(11), 1–23.

Towbin, W. H., Plank, T., Klein, E., & Hauri, E. (2023). Measuring h2o concentrations in olivine by secondary ion mass spectrometry: Challenges and paths forward. *American Mineralogist*, *108*(5), 928–940.

Vergniolle, S., & Jaupart, C. (1986). Separated two-phase flow and basaltic eruptions. *Journal of Geophysical Research: Solid Earth*, *91*(B12), 12842–12860.

Wallace, P. J., Plank, T., Bodnar, R. J., Gaetani, G. A., & Shea, T. (2021). Olivine-hosted melt inclusions: A microscopic perspective on a complex magmatic world. *Annual Review of Earth and Planetary Sciences*, *49*, 465–494.

Welsch, B., Faure, F., Famin, V., Baronnet, A., & Bachèlery, P. (2012). Dendritic crystallization: A single process for all the textures of olivine in basalts? *Journal of Petrology*, *54*(3), 539–574.

Welsch, B., Hammer, J., & Hellebrand, E. (2014). Phosphorus zoning reveals dendritic architecture of olivine. *Geology*, *42*(10), 867–870.

Wieser, P. E., Lamadrid, H., Maclennan, J., Edmonds, M., Matthews, S., Iacovino, K., ... others (2021). Reconstructing magma storage depths for the 2018 Kılauean eruption from melt inclusion co_2 contents: the importance of vapor bubbles. *Geochemistry, Geophysics, Geosystems*, *22*(2), e2020GC009364.

Zhang, Y. (2009). *Geochemical kinetics.* Princeton University Press.

Zimmer, M. M., Plank, T., Hauri, E. H., Yogodzinski, G. M., Stelling, P., Larsen, J., ... Nye, C. J. (2010). The role of water in generating the calc-alkaline trend: new volatile data for Aleutian magmas and a new tholeiitic index. *Journal of Petrology*, *51*(12), 2411–2444.

1308 # Tables

Table 1. Coefficient values for empirical correction shown in Equation (13). This transforms decompression rates estimated using 1D symmetric and asymmetric models into an equivalent 3D estimate.

Anisotropy	a_1	a_2	a_3	a_4
Symmetric 1D models				
3.0	1.06	9.85	1.09	-0.0214
15.6	1.31	7.02	1.72	0.0334
35.0	1.35	6.20	1.80	0.0973
Asymmetric 1D models				
3.0	0.522	11.4	0.734	0.00541
15.6	0.609	9.46	1.21	0.0727
35.0	0.596	9.02	1.30	0.134

1309 # Figures
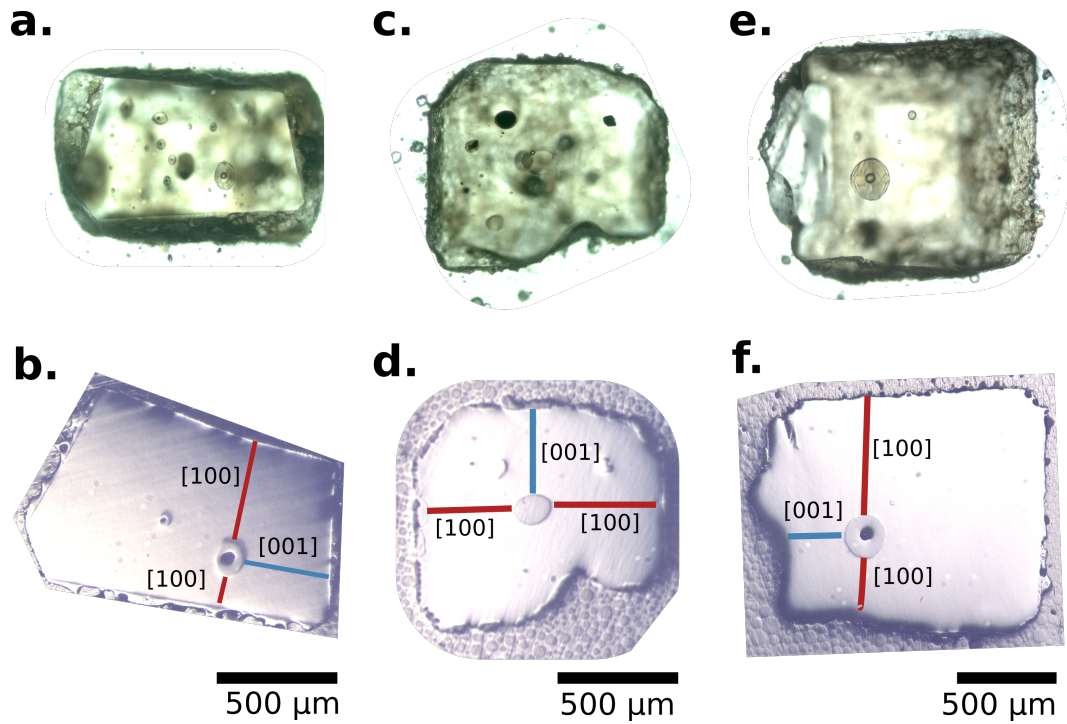
Figure 1. Transmitted light (a, c, e) and reflected light (b, d, f) photomicrographs of polished Seguam olivine crystals used in this study. (a, b) shows sample Seg1-MI1, (c, d) shows Seg4-MI1 and (e, f) shows Seg13-MI1. The location of measured SIMS profiles adjacent to the exposed melt inclusion are shown in the reflected light images. Profiles measured close to the [100] crystallographic direction are marked in red, whilst profiles measured close to [001] are shown in blue. Scale bars are shown next to the reflected light images.
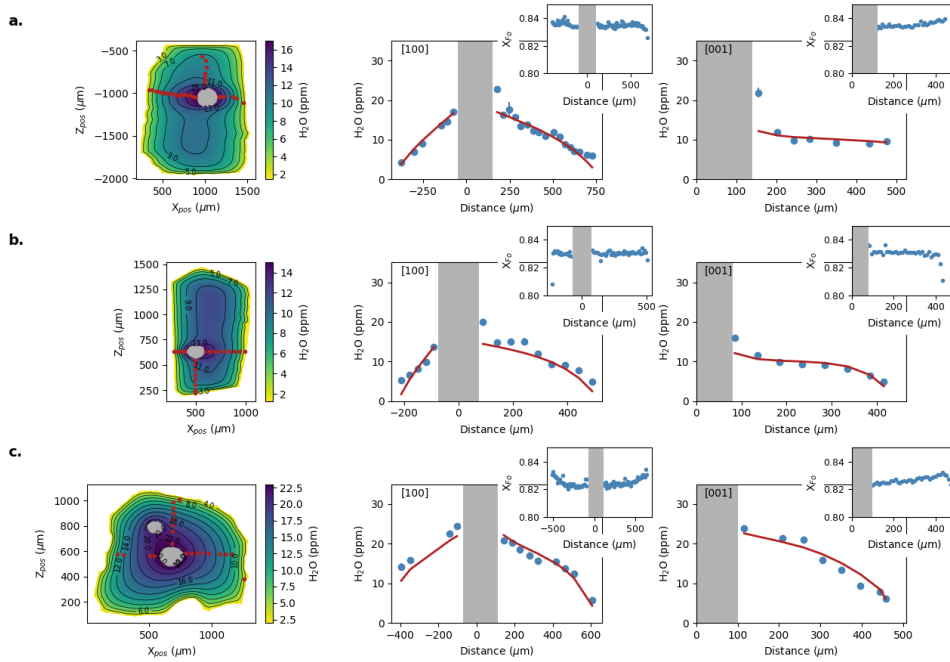
Figure 2. Measured water concentrations, major element contents and best fit Bayesian inversion models for Seg13-MI1 (a), Seg1-MI1 (b) and Seg4-MI1 (c). The first column shows colour maps and contours of 2D best-fit models for each crystal. The location of SIMS spots are shown in red. The second and third columns show SIMS water profile data measured along [100] and [001] respectively, with the best model curves shown in red. Error bars on SIMS data are shown and may be smaller than data symbols. Insets show forsterite profiles (X_{Fo}, mol fraction) measured in the same locations. Melt inclusions are represented by grey regions.
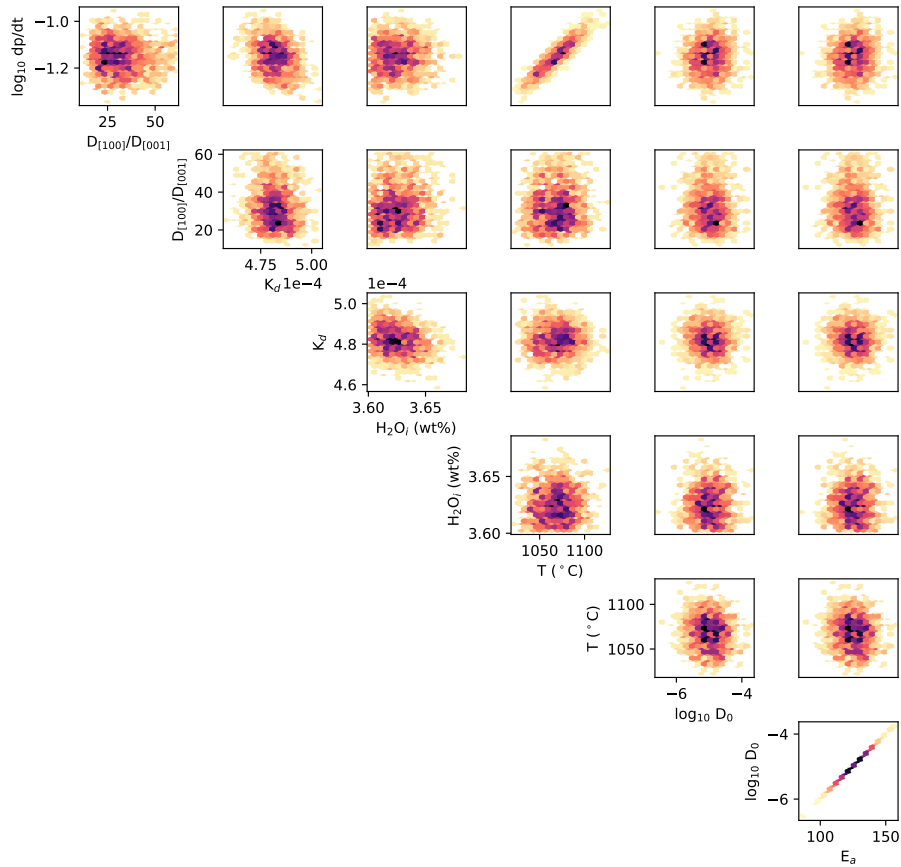
Figure 3. Density plots showing the posterior distributions of the 2D Bayesian inversion calculations performed on sample Seg13-MI1. Inverted parameters include log decompression rate ($\log_{10}$ dp/dt), the anisotropy of H^+ diffusion in olivine ($D_{[100]}/D_{[001]}$), the olivine-melt partition coefficient for water (K_d), initial water content (H_2O_i), temperature, $\log_{10} D_0$ and the activation energy (E_a) for the diffusion of H^+ in olivine. Prominent trade-offs between decompression rate, temperature, and the partition coefficient can be observed.
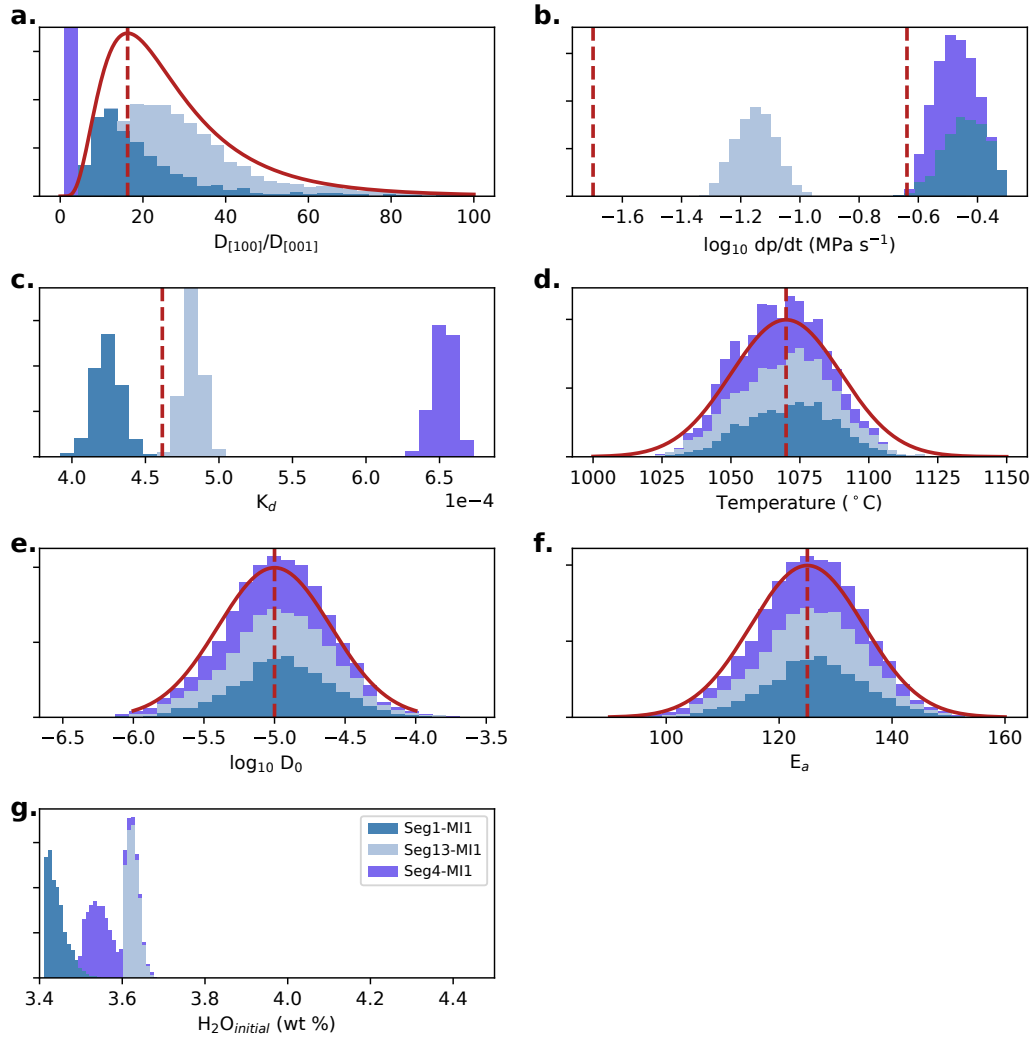
Figure 4. Stacked histograms showing the posterior distributions from the 2D Bayesian inversion calculations for Seguam olivine samples Seg1-MI1 (dark blue), Seg13-MI1 (light blue) and Seg4-MI1 (slate blue). Inverted parameters shown are diffusive anisotropy of H^+ in olivine (a), log decompression rate ($\log_{10}$ dp/dt) (b), partition coefficient (c), temperature (d), $\log_{10}$ D_0 (e), the activation energy (f), and initial water content (g). The red curve in (a) is a log normal distribution fitted to the total anisotropy distributions for Seg1-MI1 and Seg13-MI1. The red dashed red line show the modal value selected for further modelling. The red dashed lines shown in (b) show the upper and lower bounds of decompression rates estimated by Newcombe, Plank, Barth, et al. (2020). The red dashed line in (c) shows the median K_d estimated from the distributions of Seg1-MI1 and Seg13-MI1, which was then used in further modelling. The red curves in (d-f) show the Gaussian prior distributions with mean values marked by the dashed lines. These mean values were used in later models.
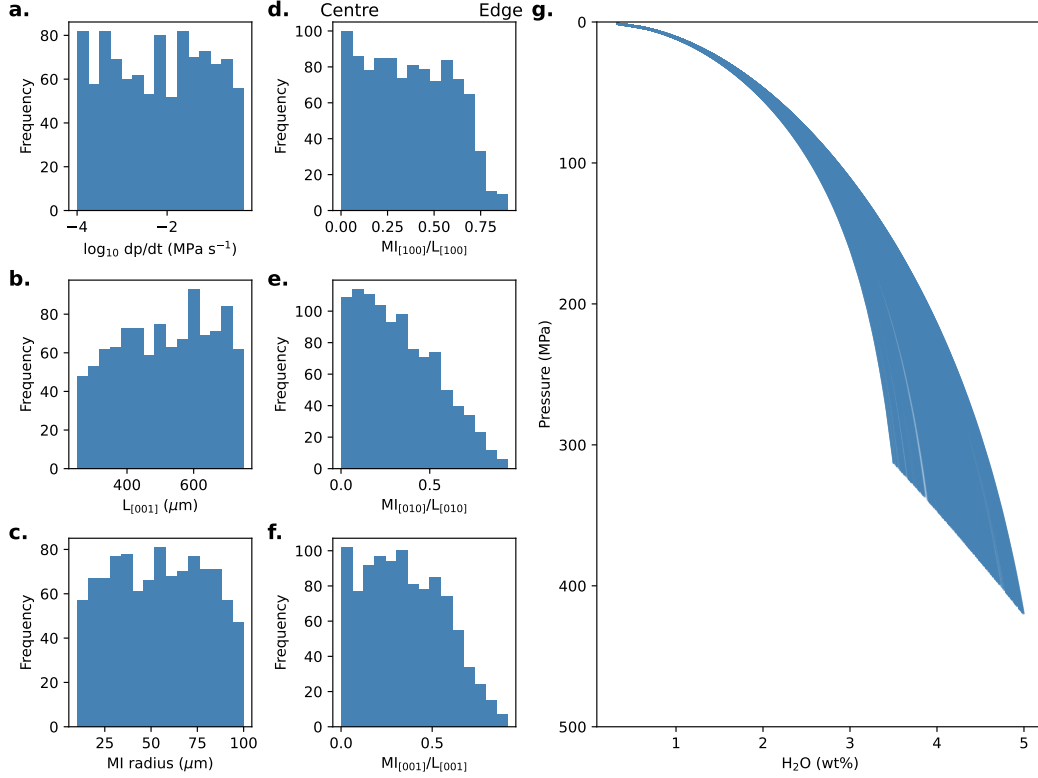
Figure 5. Distributions of the physical and geometrical parameters that were varied during the 3D Monte Carlo modelling for all of the partition coefficients that we used (K the compa $= 0.000459$, 0.001, and random subset between 0.0004 and 0.002). (a) shows the log of magma decompression rate ($\log_{10}$ dp/dt MPa s^{-1}). (b) shows crystal size which has been parameterised as the length of the [001] axes from the centre of the crystal (μm). (c) shows the melt inclusion size which has been parameterised as melt inclusion radius (μm). (d-f) show the location of the melt inclusion along the [100], [010] and [001] directions respectively. These position values have been normalised to the length of the corresponding axes. Values close to 0 are close to the centre, whilst values close to 1 are close to the crystal edge. (g) shows the distribution of water solubility curves that correspond to different initial water contents in the melt and starting pressures. These curves represent the equilibrium degassing pathways that were used in each model realisation, and thus relate to the exterior boundary condition. Solubility curves were calculated using VolatileCalc (Newman & Lowenstern, 2002)
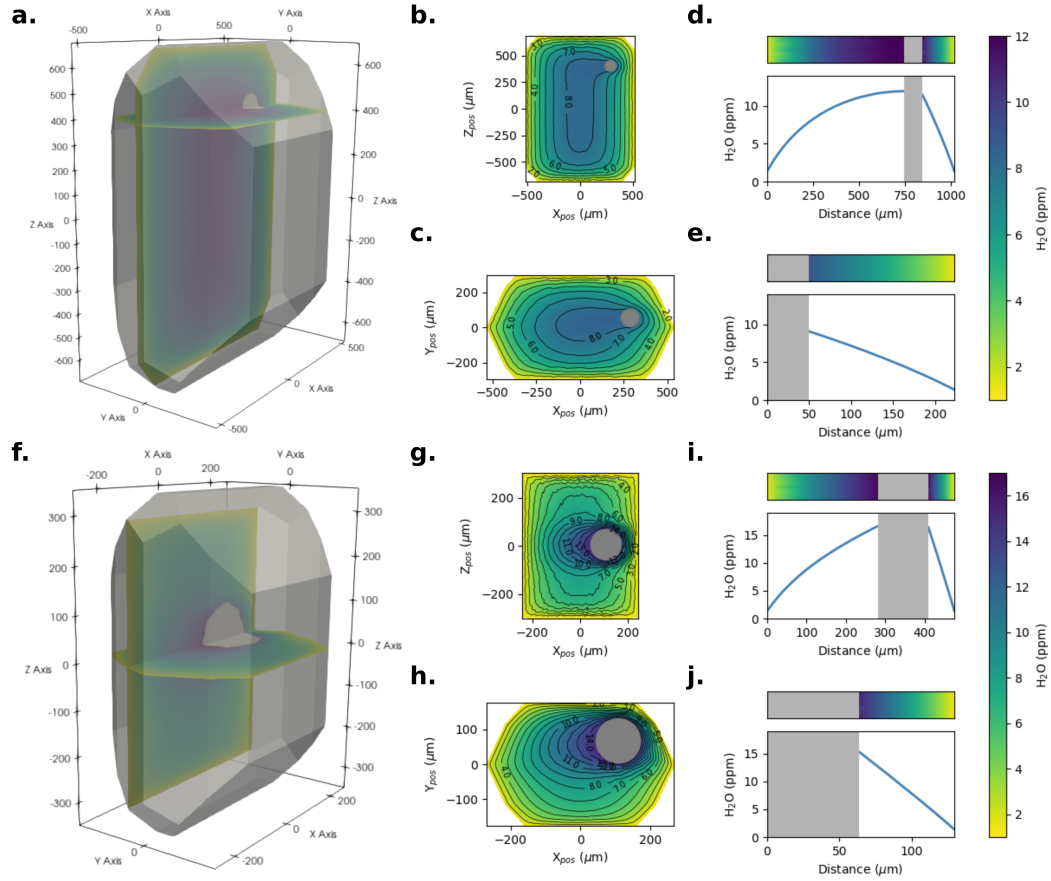
Figure 6. Example model configurations used in the Monte Carlo simulations. (a, f) show the initial 3D models, which have been sectioned along (010) and (001) through the centre of the melt inclusion. (b, g) show 2D models based on (010) sections through the centre of the melt inclusion. (c, h) show 2D models based on (001) sections through the centre of the melt inclusion. (d, i) show 1D models along the [100] axis that incorporate both edges of the crystal (termed asymmetric models here). (e, j) show 1D models with reflective boundary at the centre of melt inclusion and only incorporates the shortest direction along the [100] axis (termed symmetric models). Melt inclusions are represented by grey regions.
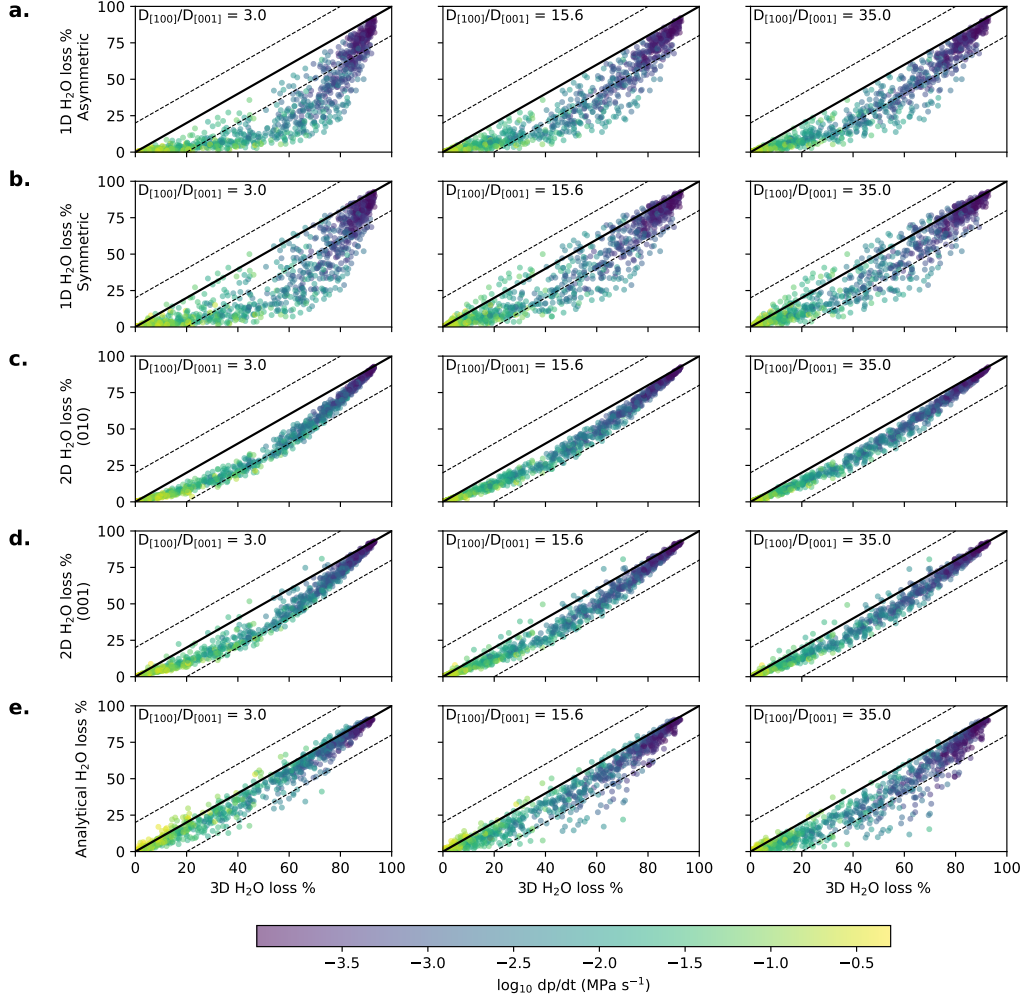
Figure 7. Results of the Monte Carlo modelling showing melt inclusion water loss for different model types and with different diffusive anisotropies ($D_{[100]}/D_{[001]}$). Comparisons are made between the 3D models and the 1D asymmetric models (a), 1D symmetric models (b), 2D models sectioned along (010) (c), 2D models sectioned along (001) (d), and the anisotropic analytical solution presented in Equation (14) (e). Each column shows model results using different diffusive anisotropies ($D_{[100]}/D_{[001]}$). 1:1 lines are shown in black with $\pm$ 20 % envelopes shown with dashed lines. Points have been colour-coded based on $\log_{10}$ decompression rate of the 3D models.
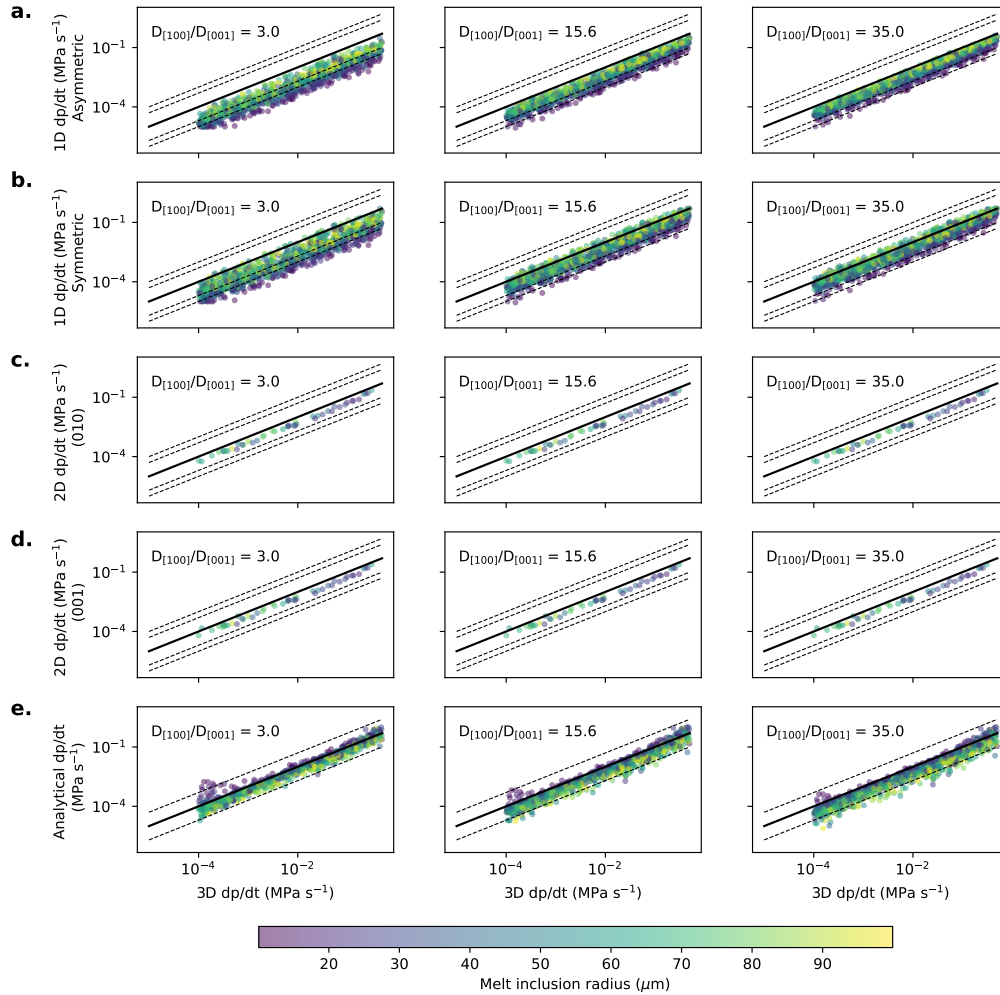
Figure 8. Comparison of 3D model decompression rates to inverted decompression rates obtained from 1D asymmetric models (a), 1D symmetric models (b), 2D models sectioned along (010) (c), 2D models sectioned along (001) (d), and the anisotropic analytical solution presented in Equation (14) (e). Each column shows model results using different diffusive anisotropies ($D_{[100]}/D_{[001]}$). 1:1 lines are shown in black with dashed lines marking points within a factor of 5. Points have been colour-coded based on melt inclusion radius.
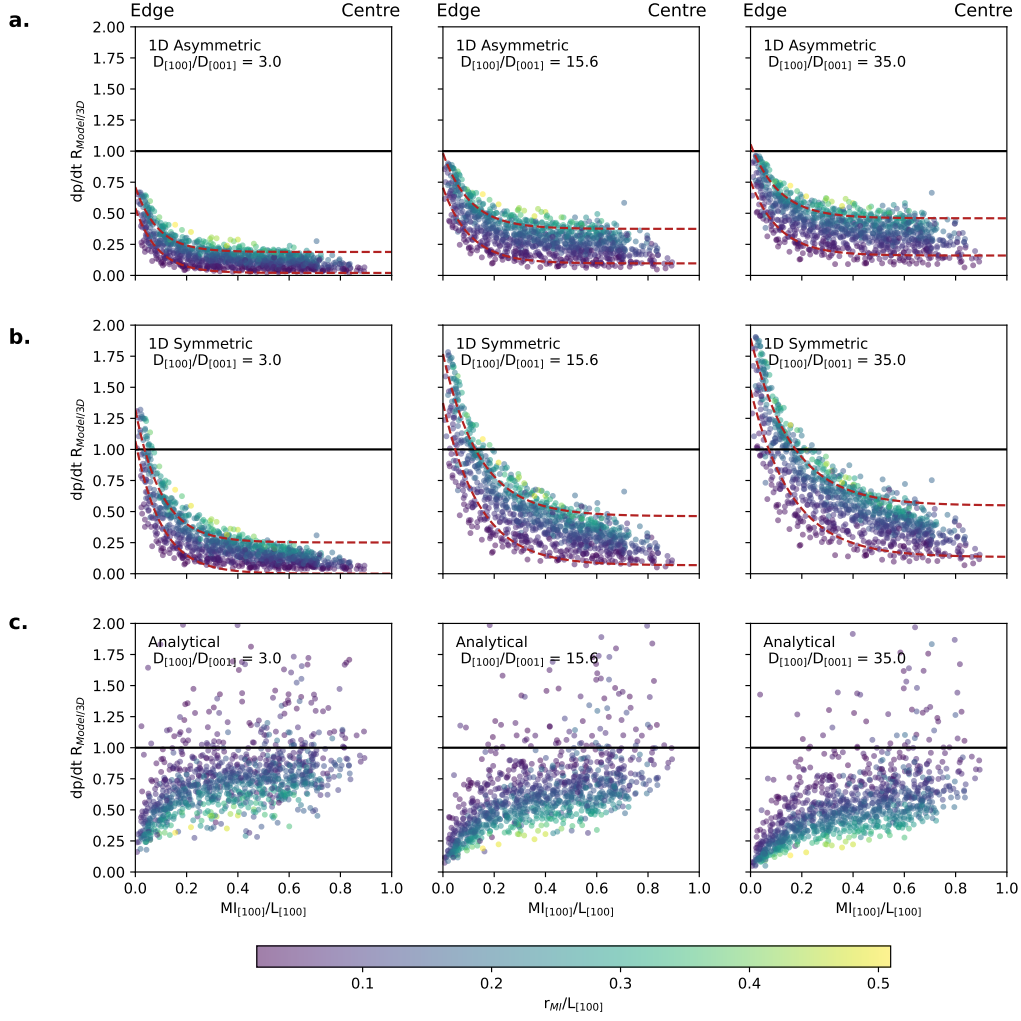
Figure 9. Geometrical controls on modelled decompression rates. Each panel shows how the position of the melt inclusion along the [100] axis affects the ratio of simplified model to 3D modelled inversion decompression rates (dp/dt $R_{model/3D}$). $MI_{[100]}$ is the distance from the nearest crystal edge to the edge of the melt inclusion along the [100] axis. $L_{[100]}$ is the distance between the crystal edge and the centre of the crystal along [100]. The melt inclusion is close to the edge when $MI_{[100]}/L_{[100]}$ is close to 0, and is close to the centre of the crystal when $MI_{[100]}/L_{[100]}$ is close to 1. Point have been coloured based on the size of the melt inclusion radius (r_{MI}) relative to the length of the [100] axis ($L_{[100]}$). The black line shows where 3D and 1D model inversions were equal (dp/dt $R_{1D/3D} = 1$). The red dashed lines show empirical model fits through the 1D model data. (a) shows results for 1D asymmetric models, (b) shows results for 1D symmetric models, and (c) shows results from the anisotropic analytical solution. Each column shows model results using different diffusive anisotropies ($D_{[100]}/D_{[001]}$).
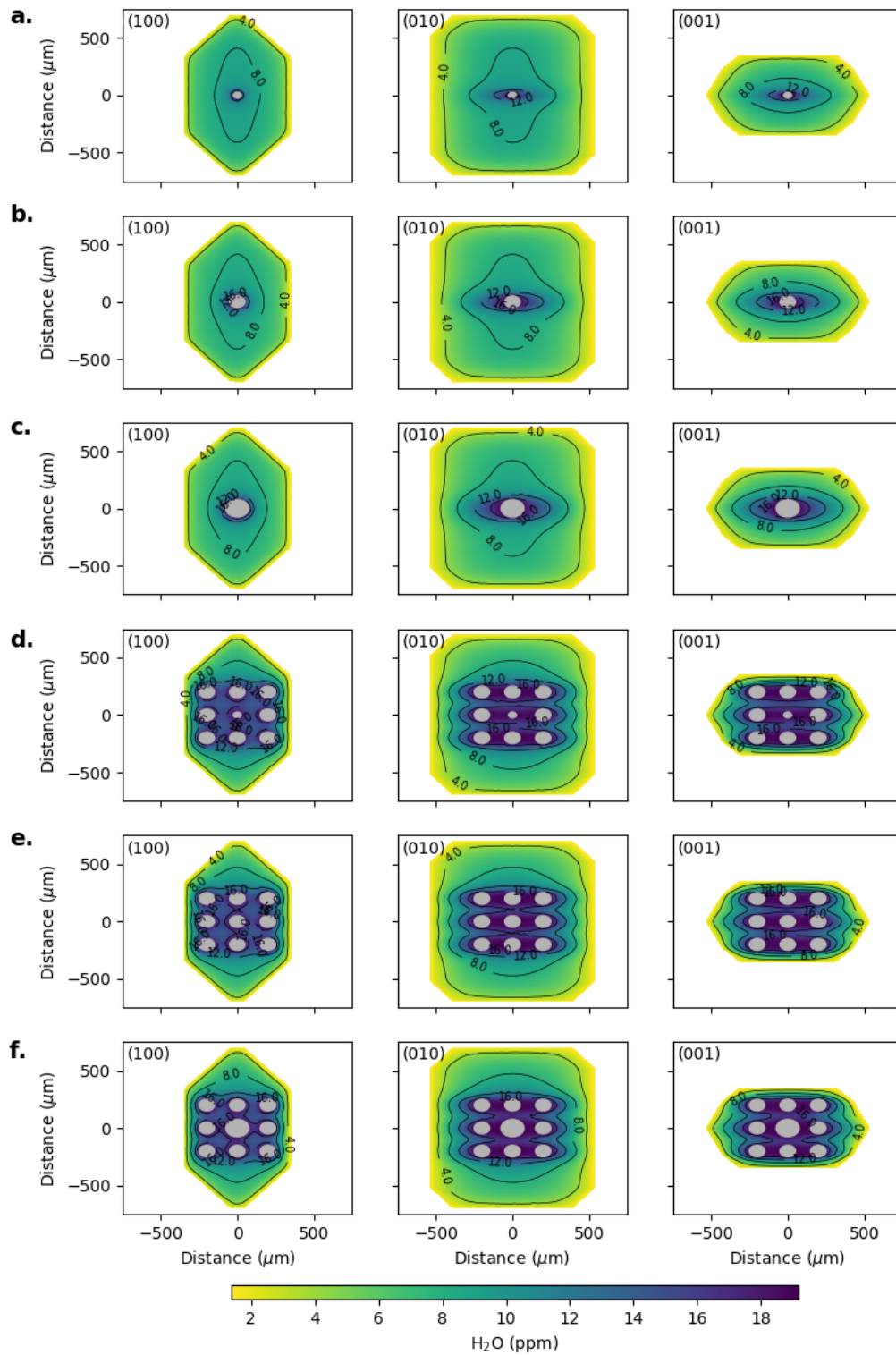
Figure 10. Configurations of 3D models that contain single and multiple melt inclusions. 2D sections through the centre of the crystal are shown perpendicular to the main crystallographic directions. Models with a single central melt inclusion with 25 μm, 50 μm and 75 μm radius are shown in (a), (b) and (c). Models with multiple melt inclusions with a central melt inclusion with 25 μm, 50 μm and 75 μm radius are shown in (d), (e) and (f). The surrounding melt inclusions in these models have 50 μm radius. All melt inclusions are represented by grey regions. Results of models for a decompression rate of 0.05 MPa s⁻¹ and a diffusive anisotropy of 15.6 are shown.
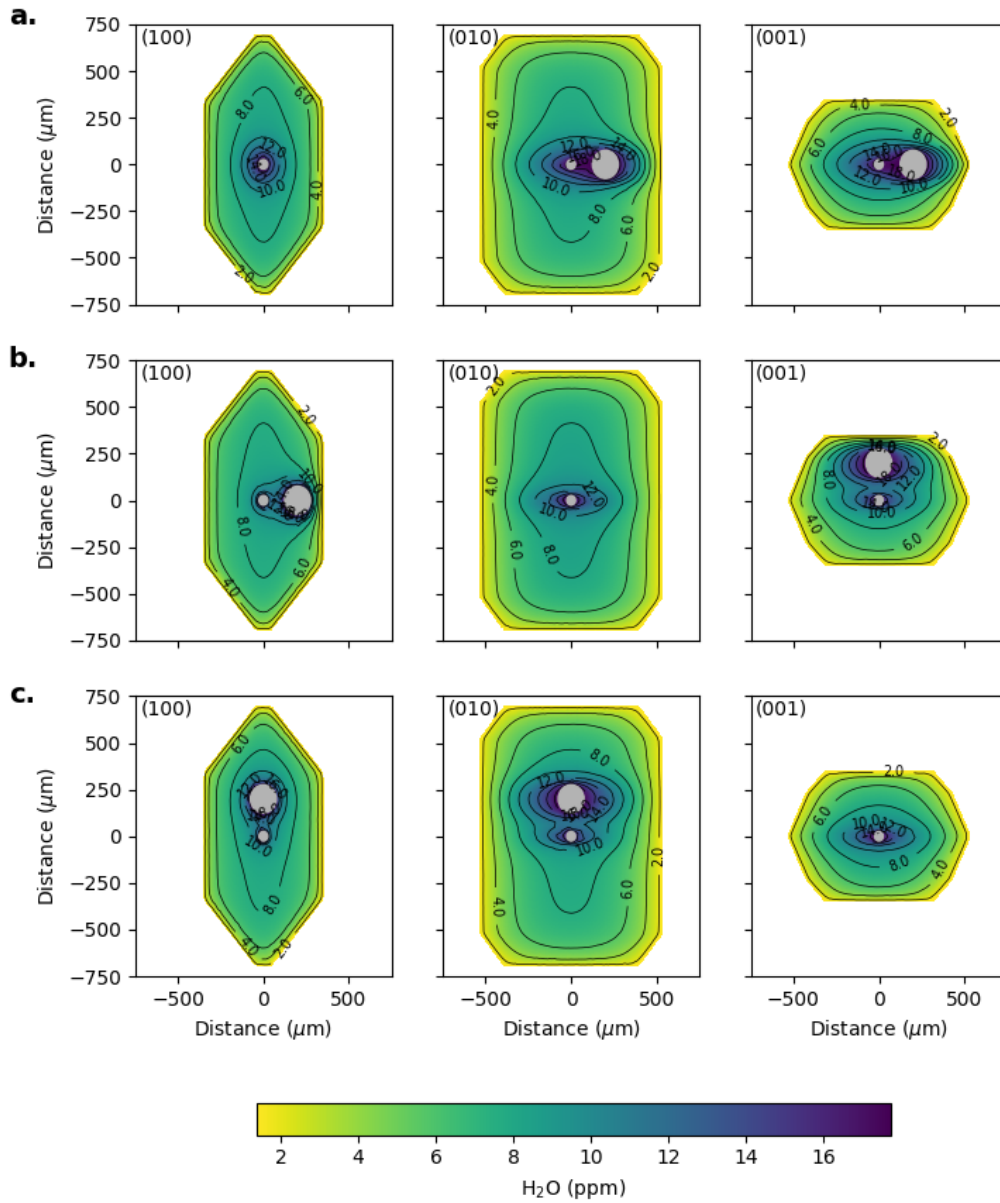
Figure 11. Model configurations of 3D models in which there are 2 melt inclusions: a 25 μm radius central inclusion and a 75 μm radius inclusion situated along one of the crystallographic axes. The large melt inclusion was placed along the [100] axis (a), the [010] axis (b), and the [001] axis (c) 250 μm from the central inclusion. All melt inclusions are represented by grey regions. Each column shows a 2D section through a 3D model. Results of models for a decompression rate of 0.05 MPa s^{-1} and a diffusive anisotropy of 15.6 are shown.
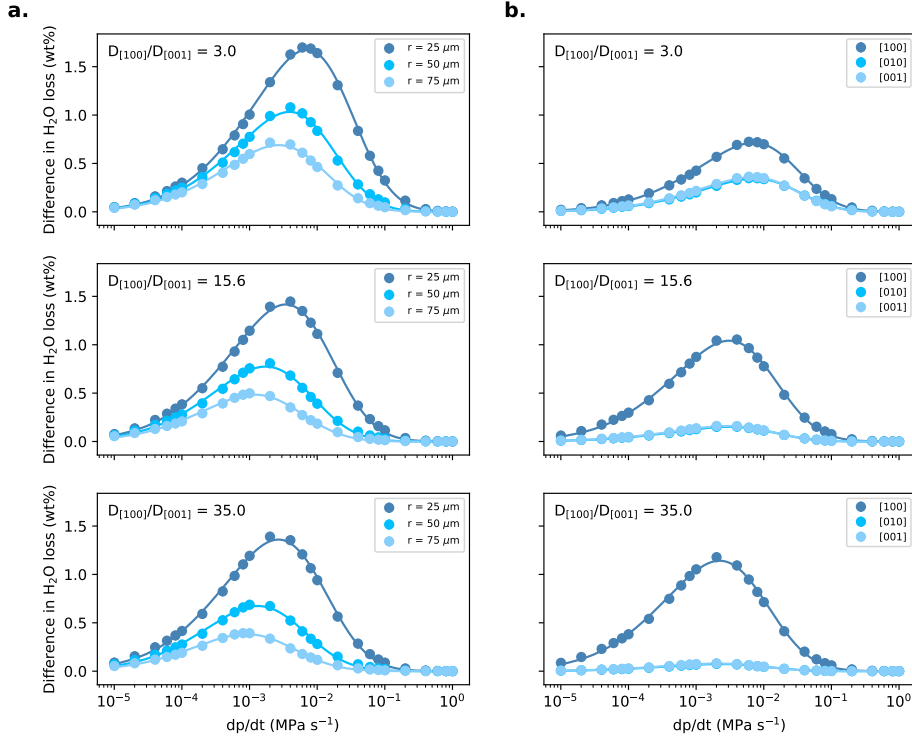
Figure 12. The role of multiple melt inclusions in controlling water loss during magma ascent. (a) Comparison of water loss from a central melt inclusion in models with a single melt inclusion (SMI) and models in which a central melt inclusion is surrounded by melt inclusions with 50 μm radius (MMI). See figure 10 for configurations. Each point shows shows the difference in water loss between the SMI models and MMI models at different decompression rates. The lines are skewed Gaussian peak fits to the data. The radius of the central melt inclusion was varied (r = 25, 50 and 75 μm), which is shown by the different shades of blue. Different panels show different model anisotropies (3, 15.6, 35) (b) Comparison of water loss from SMI models (radius of 25 μm) with models in which a 75 μm radius melt inclusion has been positioned along one of the principle crystallographic axes ([100], [010] and [001]), which corresponds to the different shades of blue. See Figure 11 for configurations. Different panels show different model anisotropies (3, 15.6, 35)

Supporting Information for 3D diffusion of water in melt inclusion-bearing olivine phenocrysts

Euan J. F. Mutch[1,2,3,4], Megan E. Newcombe[1], John F. Rudge[5]

[1]Department of Geology, University of Maryland, 8000 Regents Dr, College Park, Maryland, 20742, United States

[2]Lamont Doherty Earth Observatory, Columbia University, 61 Route 9W, Palisades, New York, 10964, United States

[3]Earth Observatory of Singapore, Nanyang Technological University, 50 Nanyang Avenue, Block N2-01A-15, 639798, Singapore

[4]Asian School of the Environment, Nanyang Technological University, 50 Nanyang Avenue, Block N2-01C-63, 639798, Singapore

[5]Bullard Laboratories, Department of Earth Sciences, University of Cambridge, Cambridge, UK

Contents of this file

1. Text S1

2. Figures S1 to S24

Additional Supporting Information (Files uploaded separately)

1. Captions for Datasets S1 to S2

Introduction

In this supplementary material we include additional information on:

- Derivation of the scaling used in the numerical models of this study.

- Comparison of numerical and analytical solutions.

- Testing for convergence of 3D numerical solutions.

- Derivation and application of the analytical solution for anisotropic equilibration of

a melt inclusion.

———————

November 21, 2023, 6:44am

Text S1.

1. Scaling for diffusion across two domains

Suppose we have two domains Ω_1 and Ω_2. In each domain we have standard diffusion equations

$$\rho_1 \frac{\partial C_1}{\partial t} = \nabla \cdot (\rho_1 D_1 \nabla C_1) \text{ in } \Omega_1 \tag{1}$$

$$\rho_2 \frac{\partial C_2}{\partial t} = \nabla \cdot (\rho_2 D_2 \nabla C_2) \text{ in } \Omega_2 \tag{2}$$

The two domains are separated by a boundary Γ. On this boundary we have the conditions

$$C_2 = KC_1 \tag{3}$$

$$-\rho_1 D_1 \frac{\partial C_1}{\partial n} = -\rho_2 D_2 \frac{\partial C_2}{\partial n} \tag{4}$$

where the first of these conditions represents the partitioning of an element with partition coefficient K, and the second represents conservation of mass across the interface.

Introduce the following rescaling

$$\tilde{C} = \begin{cases} C_1 & \text{in } \Omega_1 \\ \dfrac{C_2}{K} & \text{in } \Omega_2 \end{cases} \tag{5}$$

$$\tilde{D} = \begin{cases} D_1 & \text{in } \Omega_1 \\ D_2 & \text{in } \Omega_2 \end{cases} \tag{6}$$

$$\tilde{\rho} = \begin{cases} \rho_1 & \text{in } \Omega_1 \\ \rho_2 K & \text{in } \Omega_2 \end{cases} \tag{7}$$

With this scaling the system is represented by a single diffusion equation in both domains,

$$\tilde{\rho} \frac{\partial \tilde{C}}{\partial t} = \nabla \cdot \left(\tilde{\rho} \tilde{D} \nabla \tilde{C} \right) \tag{8}$$

with standard continuity relationships across the interface Γ,

$$\left[\tilde{C} \right]_-^+ = 0 \tag{9}$$

$$\left[-\tilde{\rho} \tilde{D} \frac{\partial \tilde{C}}{\partial n} \right]_-^+ = 0 \tag{10}$$

Hence we can just solve equation (8) by standard methods with a spatially varying $\tilde{\rho}$ and $\tilde{D}$, without needing to treat the interface in a special manner. Importantly we preserve the symmetry of the underlying operator.

2. Comparison of numerical and analytical solutions for 1D diffusion and partitioning between two phases

In this section we compare the results of 1D numerical models using our scaling for diffusion and partitioning between multiple domains with analytical solutions presented in Equations (3-44a) and (3-44b) from Zhang (2009). The analytical solutions take the following form:

$$C^L = C^L_\infty + \frac{\gamma(C^R_\infty - KC^L_\infty)}{1 + K_\gamma}\text{erfc}\frac{|x|}{2\sqrt{D^L t}}, \text{ for } x < 0 \tag{11}$$

$$C^R = C^R_\infty + \frac{KC^L_\infty - C^R_\infty}{1 + K\gamma}\text{erfc}\frac{|x|}{2\sqrt{D^R t}}, \text{ for } x > 0 \tag{12}$$

where $\gamma = (\rho^R/\rho^L)(D^R/D^L)^{1/2}$, C^L and C^R are the concentrations in the left and right domains. C^L_∞ and C^R_∞ are concentrations at infinite distance in the left and right domains. D^L and D^R are the diffusivities in the left and right domains, ρ^L and ρ^R are the densities in the left and right domains. K is the partition coefficient at the boundary ($x = 0$).

For the comparison between the analytical and numerical solutions we used two domains. The left domain extended from -1 to 0. We assigned a density (ρ^L) of 1.0, a diffusivity (D^L) of 0.01, and an initial concentration and boundary concentration(C^L_∞) of 7.5. The right domain extended from 0 to 1. We assigned a density (ρ^R) of 1.2, a diffusivity (D^R) of 0.005, and an initial concentration and boundary concentration(C^R_∞) of 10.0. The partition coefficient ($K = C^R/C_L$) is equal to 2.0. We made the comparison using two different timescales; 2 units of time and 10 units of time. In the 1D numerical model, we divided

the domain into 1000 mesh points, and used 2000 time steps in each simulation. Figure S1 shows there is excellent agreement between the analytical and numerical solutions, which gives us confidence that our numerical formulation is a good approximation that can be used in future analysis.

3. Testing for convergence of the 3D numerical solution

The accuracy of finite element analysis towards the true solution of the partial differential equation can depend on the mesh resolution and sampling across the physical domain. In general, the higher the mesh resolution, the more accurate the solution as the behaviour of the system is better sampled across the domain. However, as the mesh resolution is increased the computational run time also increases. In order to obtain the optimal balance between accuracy and runtime, we performed a convergence analysis. We generated an olivine mesh with a [001] axis length of $500\,\mu m$ from the centre, and with a $30\,\mu m$ radius melt inclusion in the centre of the crystal. The model configuration can be seen in Figures S5 and S6. In each simulation we refined the olivine mesh from $30\,\mu m$ down to $4\,\mu m$. The melt inclusion mesh resolution in each simulation was set to half of the olivine resolution (i.e., $2 - 15\,\mu m$). In each simulation, we kept the decompression rate (0.02 MPa s^{-1}), initial water content (4.2 wt%), final water content (0.3 wt%), temperature ($1070\,°C$), anisotropy (17.3), partition coefficient (0.000461) and degassing parameters (initial CO_2 content of 900 ppm, with closed system degassing with 2wt% excess CO_2) constant. We tracked the concentration of water at the centre of the melt inclusion at the end of each simulation in order to assess convergence. We used two different timesteps, 36 and 180 seconds, as an additional means to compare accuracy. Figure S2 shows that coarser meshes tend to overestimate water loss, and the solution starts to converge at finer resolutions. Over the olivine mesh resolutions that we employ in our 3D models (4 –

12 μm, shown by the grey region in Figure S2), we can see that the solutions are typically within 0.05 wt% of the converged 'True' solution. This corresponds to approximately 6 % of the total water loss, which could be considered the uncertainty of the 3D models.

4.   Analytical solution for anisotropic equilibration of a melt inclusion

In this section we describe the derivation of a analytical solution for the anisotropic equilibration of a spherical melt inclusion. The final set of solutions are presented as Equations (14) – (16) in the main text. We then compare the output of the analytical solutions to eigenfunctions from an example of a 3D numerical model. Finally, we look at the evolution of melt inclusion composition over time during magma decompression.

4.1. Equilibration of an ellipsoidal inclusion

Suppose we have two domains Ω_1 and Ω_2 with an interface Γ between them. Ω_2 (the inclusion) is a ellipsoid with principal semi-axes a, b, and c. Suppose the domain Ω_1 is unbounded. Work in the limit where diffusion is sufficiently fast in the inclusion domain Ω_2 that the concentration is uniform. Inside Ω_2 we have the mass balance

$$\frac{\mathrm{d}}{\mathrm{d}t}\left(\rho_2 V_2 C(t)\right) = -Q(t) \tag{13}$$

where $Q(t)$ is the net flux out of the inclusion and V_2 is the volume of the inclusion. Outside the inclusion assume steady-state diffusion, namely

$$\nabla^2 C = 0 \text{ in } \Omega_1 \tag{14}$$

The two equations above are linked by conservation of flux

$$Q = \int_\Gamma -\rho_1 D_1 \frac{\partial C}{\partial n} \, \mathrm{d}S \tag{15}$$

November 21, 2023, 6:44am

:

For an ellipsoidal inclusion there is a neat result that the surfaces of constant C are ellipsoids given by

$$\frac{x^2}{a^2 + \lambda} + \frac{y^2}{b^2 + \lambda} + \frac{z^2}{c^2 + \lambda} = 1 \tag{16}$$

for $\lambda \geq 0$ (see `https://dlmf.nist.gov/19.33`). The concentration field in Ω_1 is

$$C(\lambda, t) = A(t) R_F \left(a^2 + \lambda, b^2 + \lambda, c^2 + \lambda\right) \tag{17}$$

where R_F is a Carlson completely-symmetric elliptic integral of the first kind (`scipy.special.elliprf`). For large distances away from the inclusion, $\lambda \sim r^2$ and $C \sim A(t)/r$. Thus $Q(t) = 4\pi \rho_1 D_1 A(t)$ and the time evolution of the inclusion is

$$\frac{\mathrm{d}}{\mathrm{d}t} \left(\rho_2 V_2 C(t)\right) = -\frac{4\pi \rho_1 D_1}{R_F(a^2, b^2, c^2)} C(t) \tag{18}$$

The volume of the ellipsoid is $V_2 = 4\pi abc/3$. Thus we have exponential decay on a time scale

$$\tau = \frac{\rho_2 abc R_F(a^2, b^2, c^2)}{3\rho_1 D_1} \tag{19}$$

In the case of a sphere $a = b = c$, $R_F(a^2, b^2, c^2) = 1/a$ and thus

$$\tau = \frac{\rho_2 a^2}{3\rho_1 D_1} \tag{20}$$

4.2. Spherical inclusion in an anisotropic medium

The above solution is useful for working out the decay time for a spherical inclusion in an anisotropic medium. Suppose now that the diffusivity in the domain Ω_1 is now anisotropic, with principal diffusivities D_x, D_y and D_z aligned with the coordinate axes. The governing equation in Ω_1 is

$$\nabla \cdot (\mathsf{D} \cdot \nabla C) = 0 \tag{21}$$

where D is the second-rank diffusivity tensor. Introduce a scaling of the spatial coordinates in the form

$$\tilde{x} = \frac{x}{\sqrt{D_x}}, \quad \tilde{y} = \frac{y}{\sqrt{D_y}}, \quad \tilde{z} = \frac{z}{\sqrt{D_z}} \tag{22}$$

In the scaled spatial coordinates the governing equation is now a standard Laplace's equation

$$\tilde{\nabla}^2 C = 0 \tag{23}$$

but now the inclusion is an ellipsoidal shape. We can thus write down the equilibration time scale using the previous analysis that lead to equation (19)

$$\tau = \frac{\rho_2 a^3 R_F \left(\frac{a^2}{D_x}, \frac{a^2}{D_y}, \frac{a^2}{D_z} \right)}{3\rho_1 \sqrt{D_x D_y D_z}} \tag{24}$$

which can be rewritten as

$$\tau = \frac{\rho_2 a^2 R_F \left(D_x^{-1}, D_y^{-1}, D_z^{-1} \right)}{3\rho_1 \sqrt{D_x D_y D_z}} \tag{25}$$

4.2.1. Special cases

Suppose we have anisotropy of the form $D_z = D_y = D_x/f$, with $f > 1$. Then one can write the Carlson elliptic function in terms of standard functions as

$$\frac{R_F \left(D_x^{-1}, D_y^{-1}, D_z^{-1} \right)}{\sqrt{D_x D_y D_z}} = \frac{1}{D_x} g(f) \tag{26}$$

where

$$g(f) = \frac{f}{\sqrt{f-1}} \cos^{-1} f^{-1/2} \tag{27}$$

so

$$\tau = \frac{\rho_2 a^2}{3\rho_1 D_x} g(f) \tag{28}$$

4.2.2. Some example numbers

Suppose we have a melt inclusion of radius $a = 30 \ \mu$m, $D_x = 1.32 \times 10^{-10} \ \text{m}^2 \ \text{s}^{-1}$, $f = 17.3$, $\rho_2/\rho_1 = 1.0/(1.2 \times 0.000461) = 1808$ (the above analysis used scaled densities,

including the partition coefficient factor of 0.000461). Then $g(f) = 5.69$ and the time scale $\tau = 23,000$ s $= 6.5$ hours. If the ascent time is less than this, then we expect to keep water in the inclusion. Figure S3 shows the concentration field of the analytical solution in either the (010) or (001) plane which looks similar to the shape of the lowest eigenmode calculated for the 3D numerical model shown in Figure S5. Figure S4 shows the shape of the analytical solution along the [100] direction and [001] direction at conditions similar to those experienced by Seg13-MI1.

4.3. Numerical eigenfunctions

The eigenfunctions and eigenvalues can also be calculated numerically for the full 3D mesh. The lowest two modes are shown in Figure S5 and Figure S6. The two modes have quite different response times. The lowest one has $\tau = 18,000$ s which compares well to the $\tau = 23,000$ s time scale for an inclusion in an infinite crystal. The shorter equilibration time for the numerical eigenfunction is presumably because of the finite crystal size. The numerical and analytical eigenmodes are also clearly very similar. The second mode has $\tau = 300$ s, around 60 times faster. This is presumably associated with the time scale for solid-state diffusion across the crystal. Roughly speaking, we'd expect this time scale to be $d^2/(\pi^2 D)$ for d a typical radius of the crystal and D an effective diffusivity. If we take D to be the same kind of average diffusivity as in Equation (25), $D = 2.3 \times 10^{-11}$ m s^{-2}, and $d = 250\mu$m, then we'd estimate $\tau = 270$ s.

4.4. Evolution of melt inclusion concentration

We can use the estimate of equilibration time scale to approximate the behaviour of melt inclusion when the boundary conditions change over time. If C_i is the melt inclusion concentration and C_0 is the concentration of the surrounding melt, the equilibration on a

time scale τ can be represented by the simple ode

$$\frac{\mathrm{d}C_i(t)}{\mathrm{d}t} = \frac{C_0(t) - C_i(t)}{\tau} \tag{29}$$

If $C_0(t)$ were constant, this would just be straight exponential decay. The solution of the above ode can be written in integral form as

$$C_i(t) = \mathrm{e}^{-t/\tau} \left(C_i(0) + \int_0^t C_0(s) \frac{\mathrm{e}^{s/\tau}}{\tau} \, \mathrm{d}s \right) \tag{30}$$

and the integral can be approximated by the trapezoidal rule if $C_0(t)$ is given. If $C_0(t)$ can be approximated by a particular functional form then the integral may even be solved analytically. Figure S7 compares the analytical solution and 3D numerical model (Figure S5) for equilibration time of 23,000 seconds over the decompression pathway. In this instance, the analytical solution and 3D numerical model compare well. Figure S8 shows the forcing timescale caused by the changing boundary conditions over the decompression pathway. At shallow depths the concentration at the boundary changes so rapidly that diffusion may not propagate to the central melt inclusion.

References

Newman, S., & Lowenstern, J. B. (2002). VolatileCalc: a silicate melt–H_2O–CO_2 solution model written in Visual Basic for excel. *Computers & Geosciences*, *28*(5), 597–604.

Zhang, Y. (2009). *Geochemical kinetics*. Princeton University Press.

Data Set S1. Secondary Ion Mass Spectrometry (SIMS) data of water concentrations in olivine crystals from the 1977 Seguam eruption used in this study. Electron probe microanalyser (EPMA) data of major elements and crystal orientations from electron backscatter diffraction (EBSD) are also included.

Data Set S2. Model inputs and outputs for the Monte Carlo diffusion modelling used in this study for water loss from a melt inclusion during magma decompression. Spreadsheet includes water loss estimated by 3D, 2D and 1D numerical models in addition to the anisotropic analytical solution. It also includes the inverted decompression rates from the 2D, 1D and analytical models.
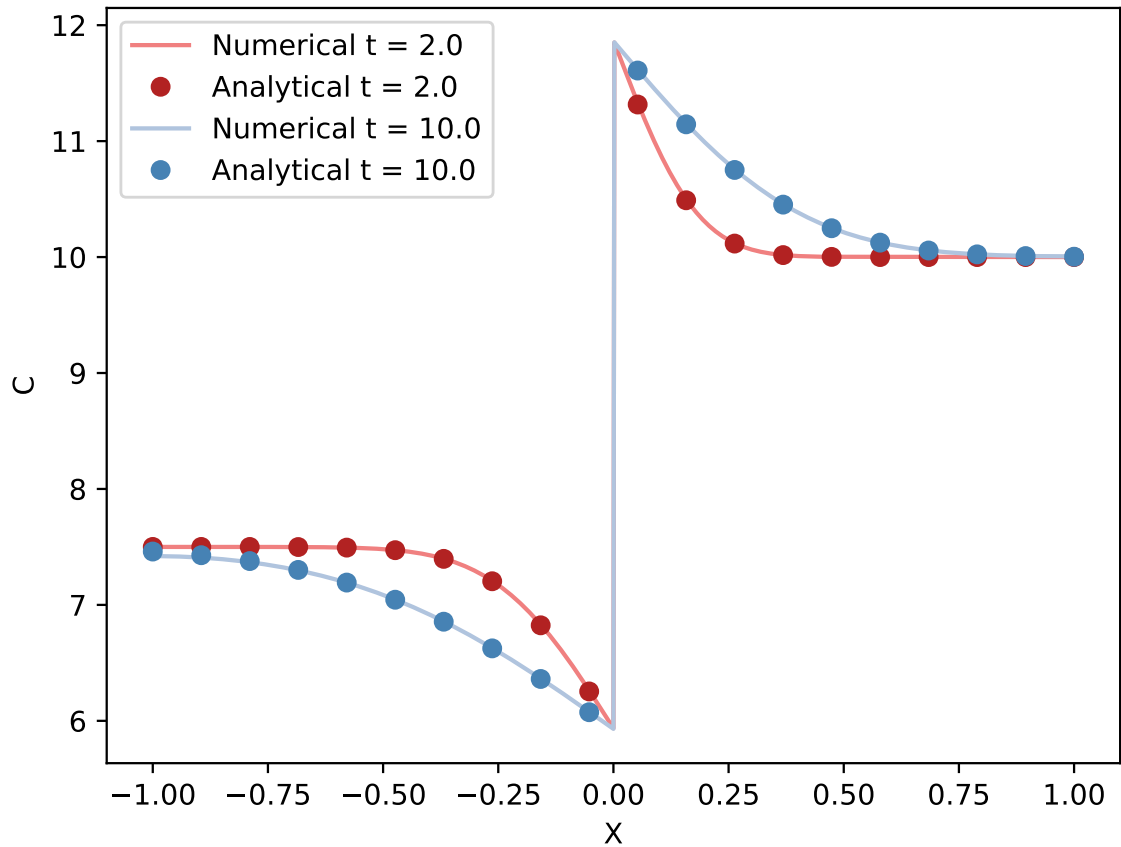
Figure S1. Comparison of a 1D multiphase numerical model with the analytical solutions for 1D diffusion and partitioning between two phases as presented in Zhang (2009). The plot shows distance verses composition. Numerical solutions are plotted as lines and the analytical solutions are plotted as points. Solutions for a 2 units and 10 units of time are shown in red and blue respectively. The analytical and numerical solutions show excellent agreement. Details of the models are discussed in the text.

November 21, 2023, 6:44am

:
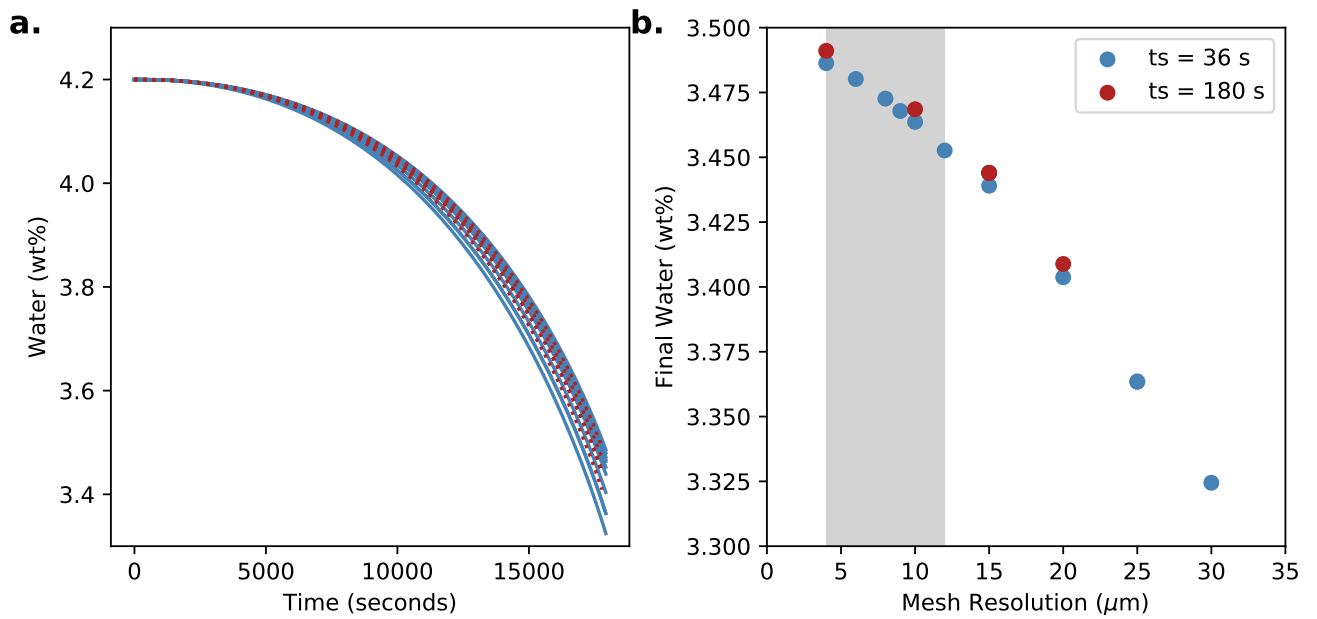
Figure S2. Testing the convergence of the 3D numerical models. Details of the modelling are discussed in the main text. (a) shows water loss from the centre of the melt inclusion over time. (b) shows the final water content of the melt inclusion with respect to the olivine mesh resolution. The melt inclusion mesh resolution is half of the olivine resolution. The grey region shows the olivine mesh resolutions that were used in the 3D Monte Carlo modelling. Solutions that used a timestep of 36 seconds are shown in blue, whilst solutions that used a timestep of 180 seconds are shown in red.
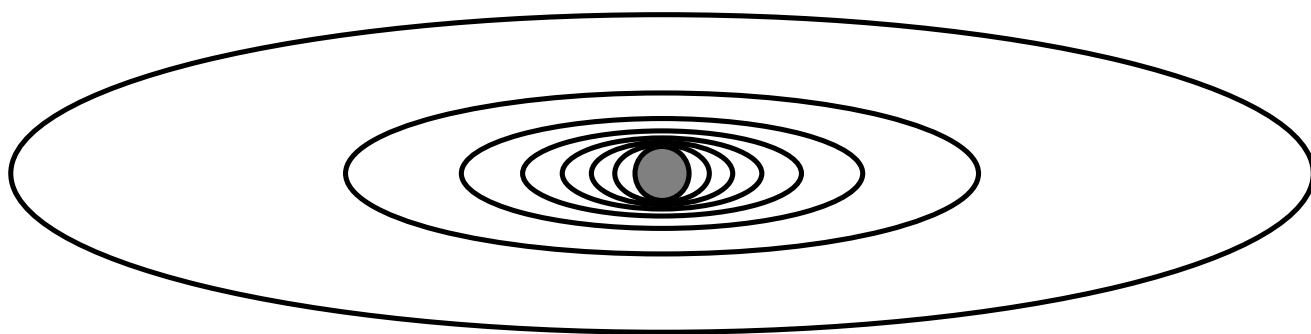
Figure S3. Contour plot of the concentration field for $f = 17.3$. Slice showing (001) $x - y$ or (010) $x - z$ plane.

:
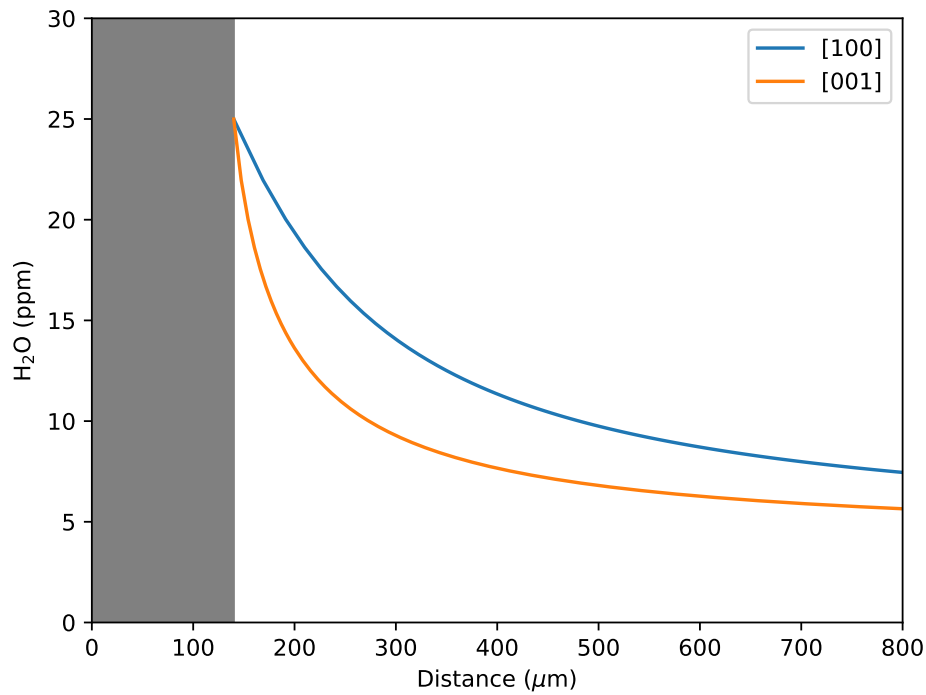
Figure S4. Profiles of the analytical solution with parameters chosen to roughly look like Seg13-MI1. Here $f = 4.5$, the inclusion radius is 70μm, the concentration at the MI boundary is 25 ppm, and that in the far field is 4 ppm. If the system reaches quasi-steady state all we are likely to get from the data is the strength of anisotropy and the concentrations in the inclusion and the far field. With Seg1-MI1 there looks to be a notable boundary layer at the crystal rim that might provide some additional timing information.
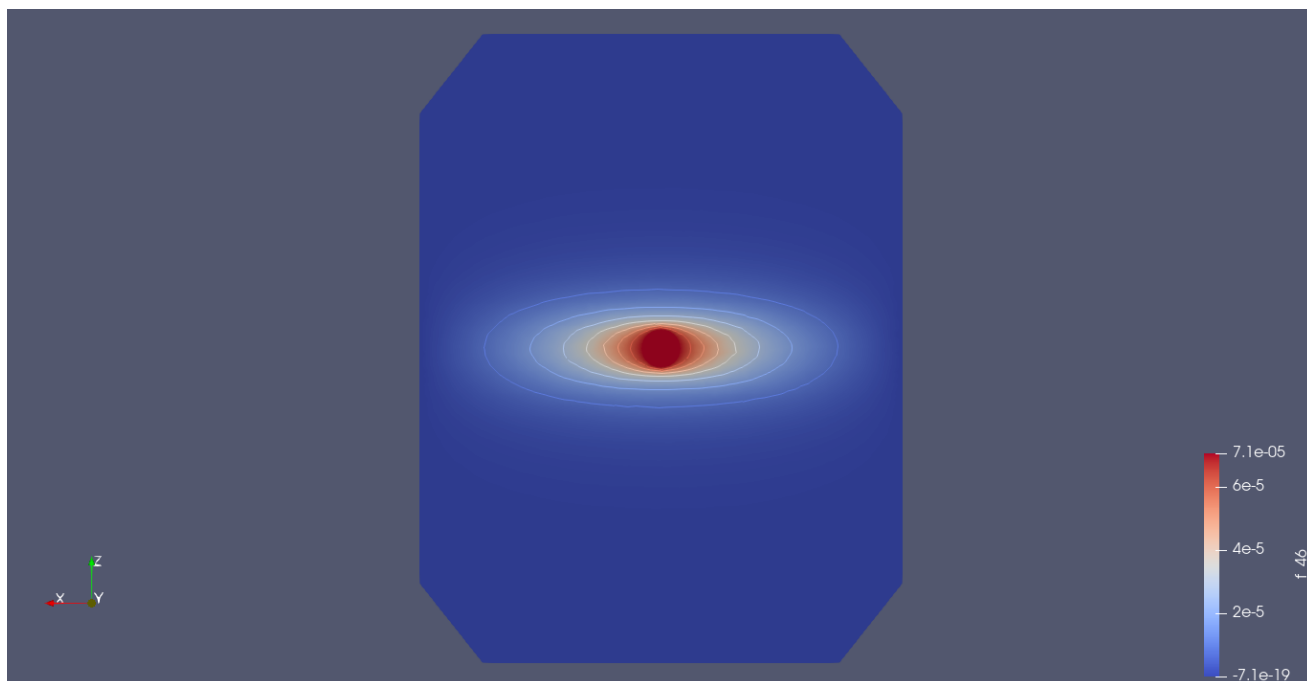
Figure S5. Contour plot of the numerically-calculated lowest eigenmode. It is very similar to the analytical solution plotted in Figure S3.
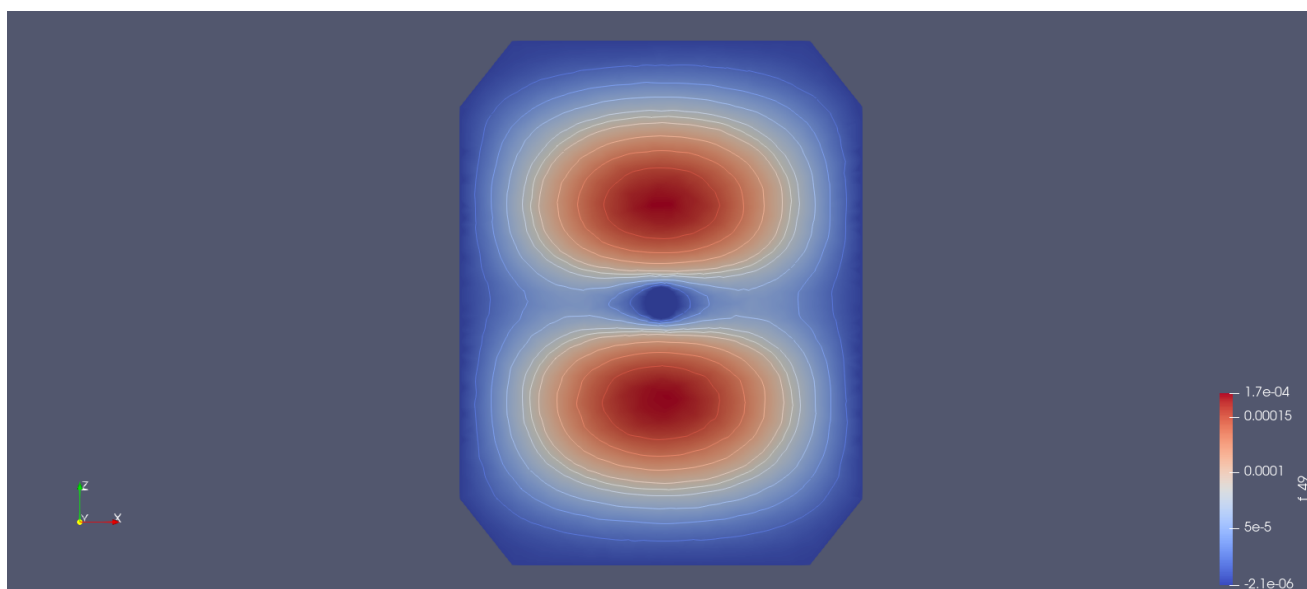
Figure S6. Contour plot of the numerically-calculated second eigenmode.
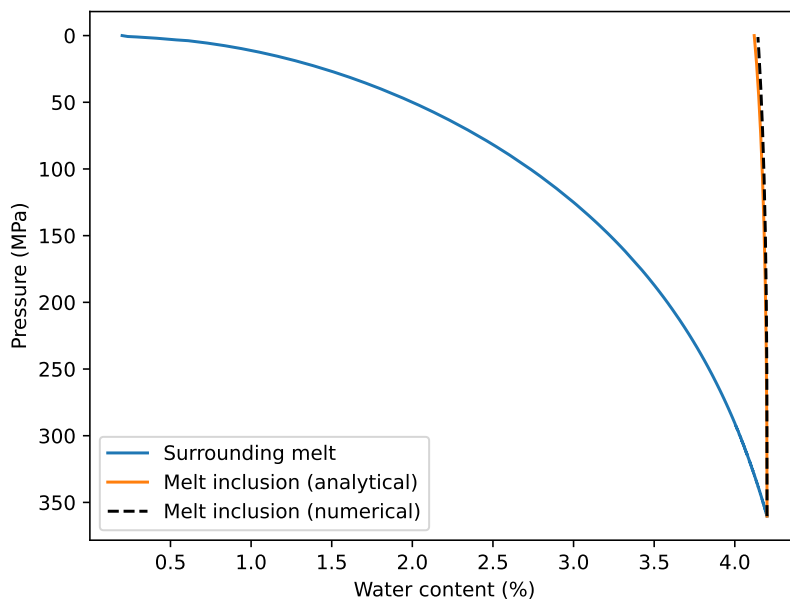
Figure S7. Evolution of melt inclusion concentration with pressure. Comparison between the full 3D numerics, and a 0D ode solve with an equilibration time of 23,000 s.
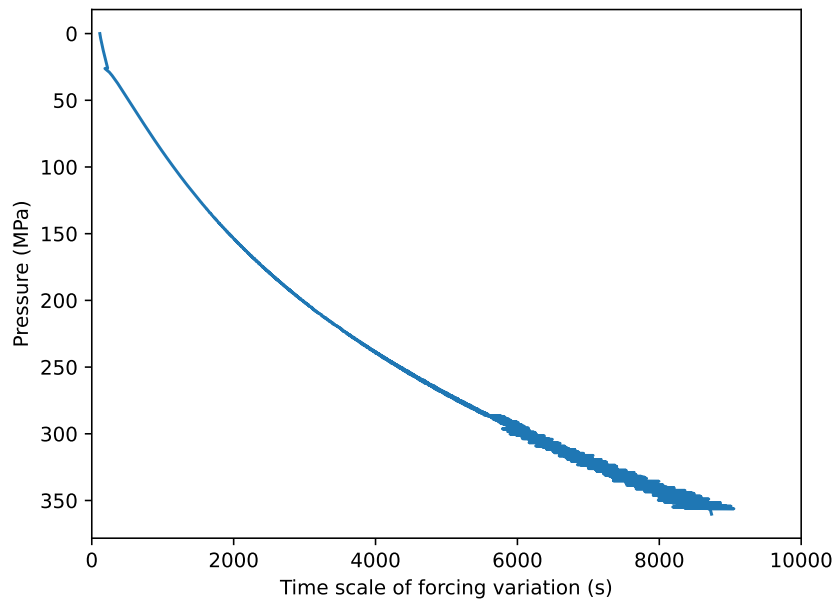
Figure S8. Plot of forcing timescale $-\mathrm{d}t/\mathrm{d}\ln C_0(t)$ against pressure. At shallow depths the concentration is so rapidly varying that there may not be time for diffusion to propagate the boundary signal to the melt inclusion. Estimate of the diffusion time $d^2/(\pi^2 D)$ along x or [100] is 114 s, in y or [010] is 830 s, and in z or [001] is 3300 s. Particularly in y and z we expect a notable boundary layer.
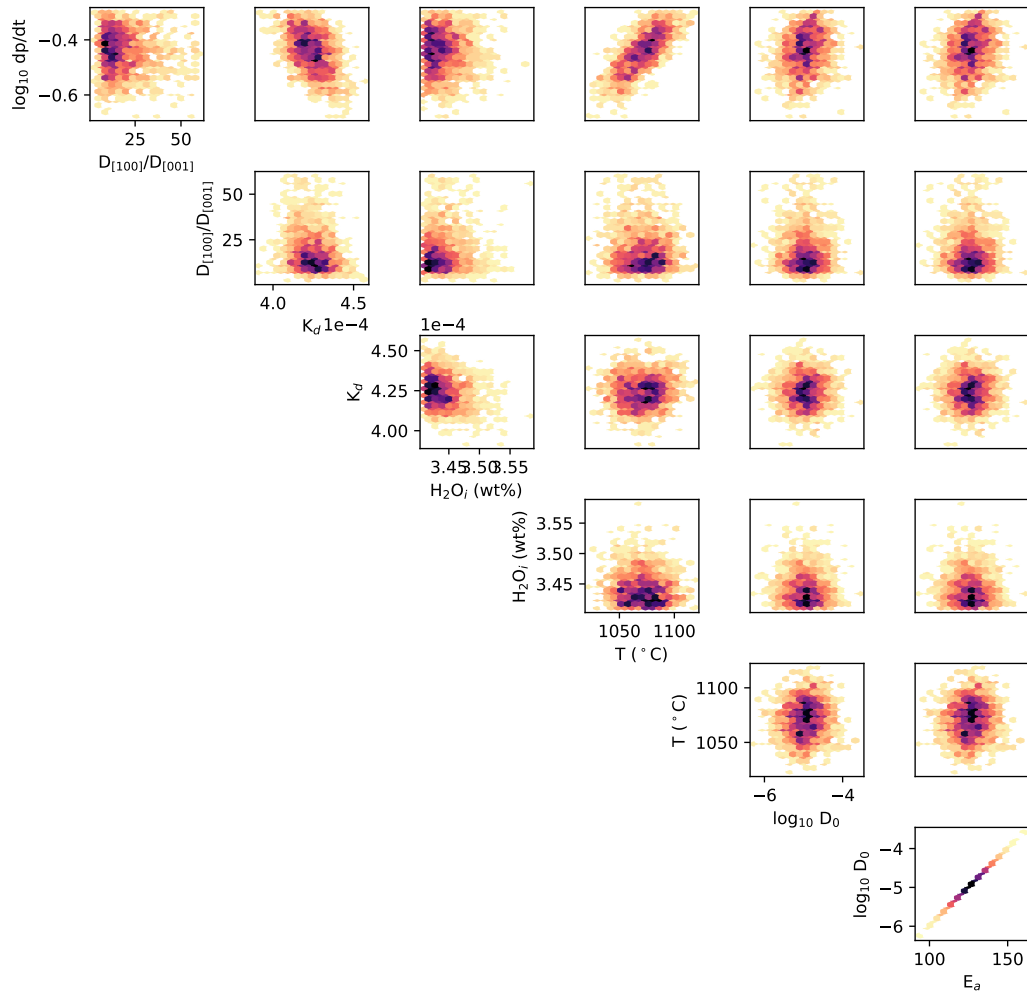
Figure S9. Density plots showing the posterior distributions of the 2D Bayesian inversion calculations performed on sample Seg1-MI1. Inverted parameters include log decompression rate ($\log_{10}$ dp/dt), the anisotropy of H^+ diffusion in olivine ($D_{[100]}/D_{[001]}$), the olivine-melt partition coefficient for water (K_d), initial water content (H_2O_i), temperature, $\log_{10} D_0$ and the activation energy (E_a) for the diffusion of H^+ in olivine.
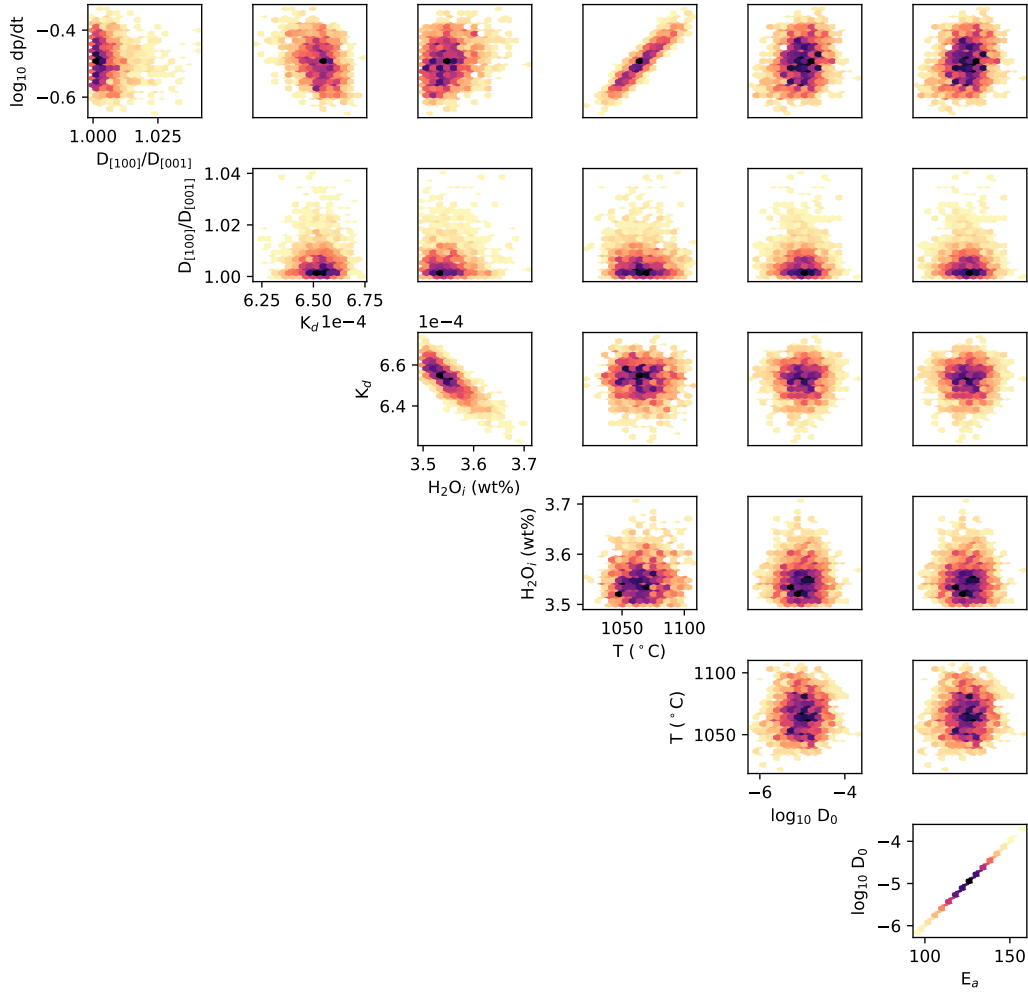
Figure S10. Density plots showing the posterior distributions of the 2D Bayesian inversion calculations performed on sample Seg4-MI1. Inverted parameters include log decompression rate ($\log_{10}$ dp/dt), the anisotropy of H^+ diffusion in olivine ($D_{[100]}/D_{[001]}$), the olivine-melt partition coefficient for water (K_d), initial water content (H_2O_i), temperature, $\log_{10} D_0$ and the activation energy (E_a) for the diffusion of H^+ in olivine.
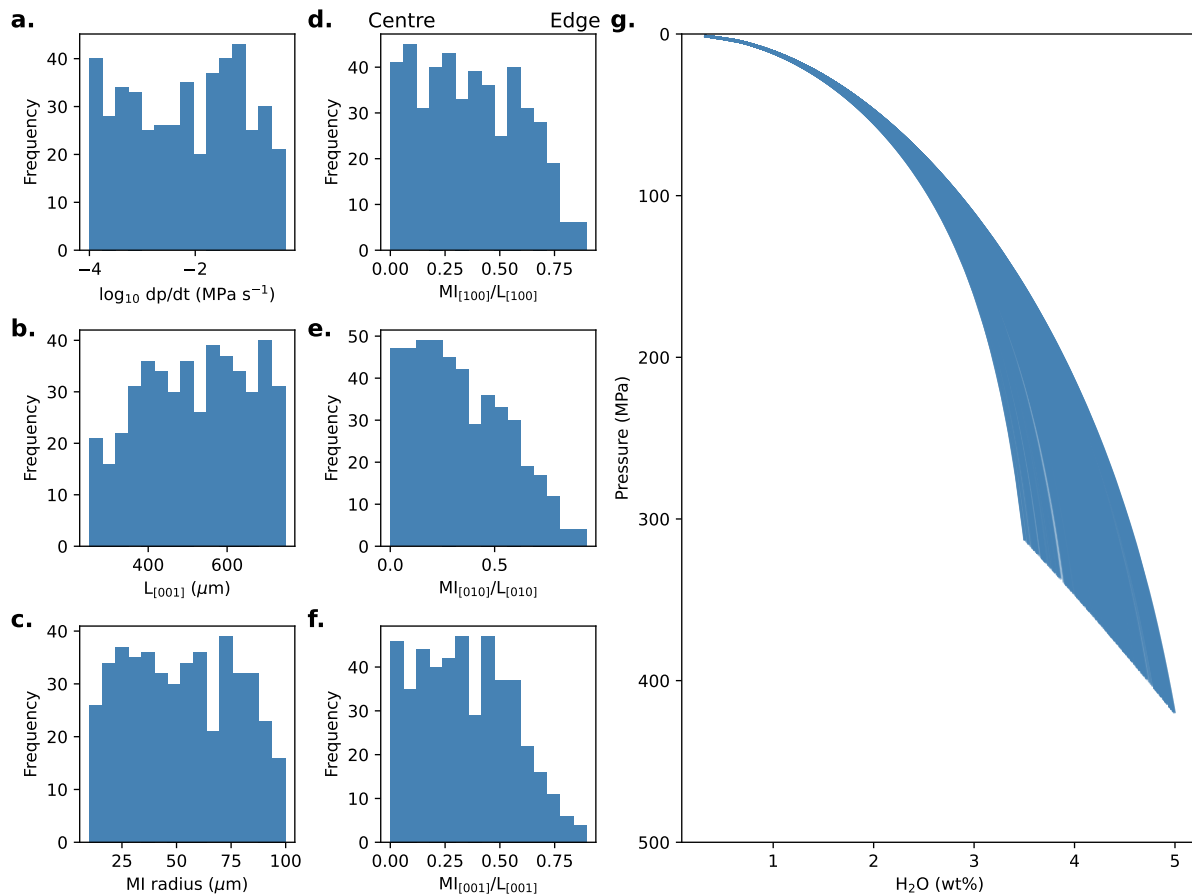
Figure S11. Distributions of the physical and geometrical parameters that were varied during the 3D Monte Carlo modelling models that used a partition coefficient of 0.000459. (a) shows the log of magma decompression rate ($\log_{10}$ dp/dt MPa s^{-1}). (b) shows crystal size which has been parameterised as the length of the [001] axes from the centre of the crystal (μm). (c) shows the melt inclusion size which has been parameterised as melt inclusion radius (μm). (d-f) show the location of the melt inclusion along the [100], [010] and [001] directions respectively. (g) shows the distribution of water solubility curves that correspond to different initial water contents in the melt and starting pressures. Solubility curves were calculated using VolatileCalc (Newman & Lowenstern, 2002)
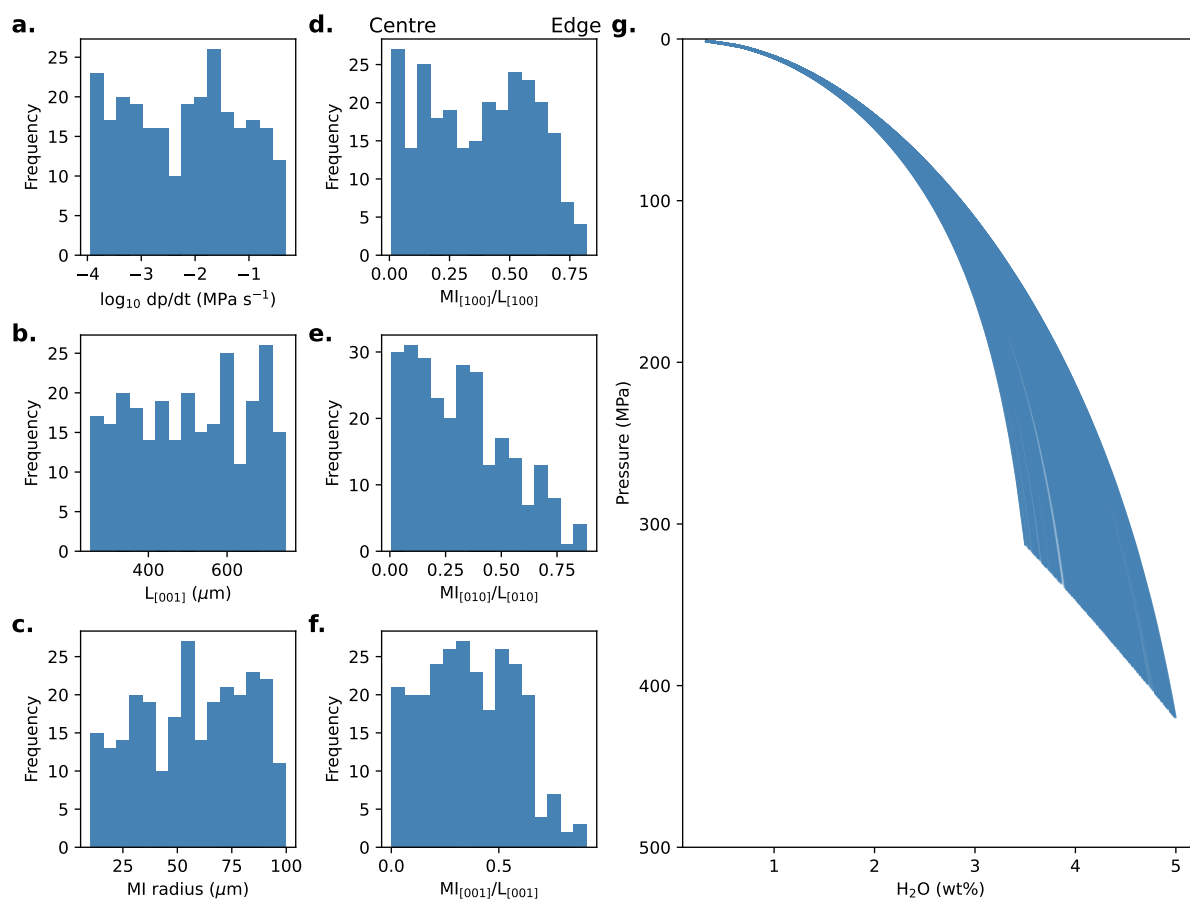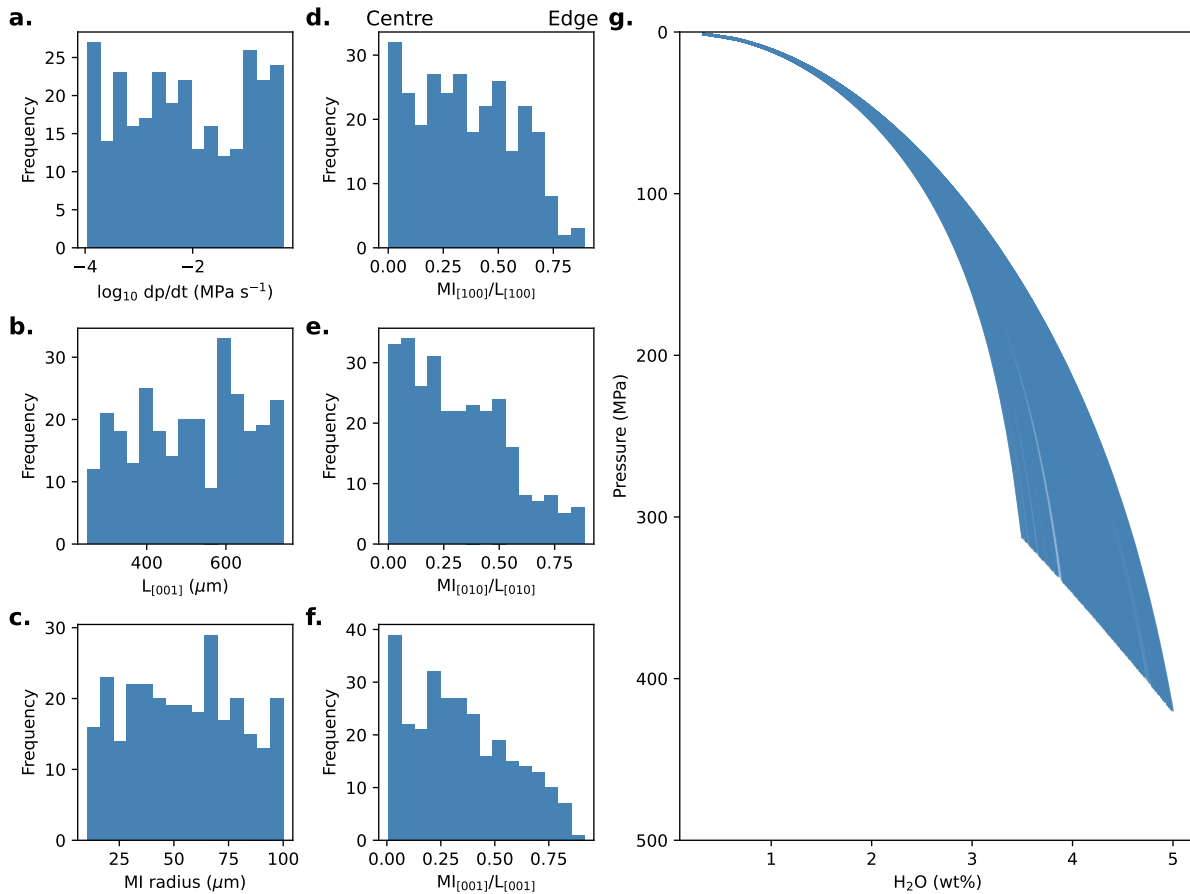
Figure S12. Distributions of the physical and geometrical parameters that were varied during the 3D Monte Carlo modelling models that used a partition coefficient of 0.001. (a) shows the log of magma decompression rate ($\log_{10}$ dp/dt MPa s^{-1}). (b) shows crystal size which has been parameterised as the length of the [001] axes from the centre of the crystal (μm). (c) shows the melt inclusion size which has been parameterised as melt inclusion radius (μm). (d-f) show the location of the melt inclusion along the [100], [010] and [001] directions respectively. (g) shows the distribution of water solubility curves that correspond to different initial water contents in the melt and starting pressures. Solubility curves were calculated using VolatileCalc (Newman & Lowenstern, 2002)

November 21, 2023, 6:44am

Figure S13. Distributions of the physical and geometrical parameters that were varied during the 3D Monte Carlo modelling models that used a random subset of partition coefficients from 0.0004 and 0.002. (a) shows the log of magma decompression rate ($\log_{10}$ dp/dt MPa s^{-1}). (b) shows crystal size which has been parameterised as the length of the [001] axes from the centre of the crystal (μm). (c) shows the melt inclusion size which has been parameterised as melt inclusion radius (μm). (d-f) show the location of the melt inclusion along the [100], [010] and [001] directions respectively. (g) shows the distribution of water solubility curves that correspond to different initial water contents in the melt and starting pressures. Solubility curves were calculated using VolatileCalc (Newman & Lowenstern, 2002)
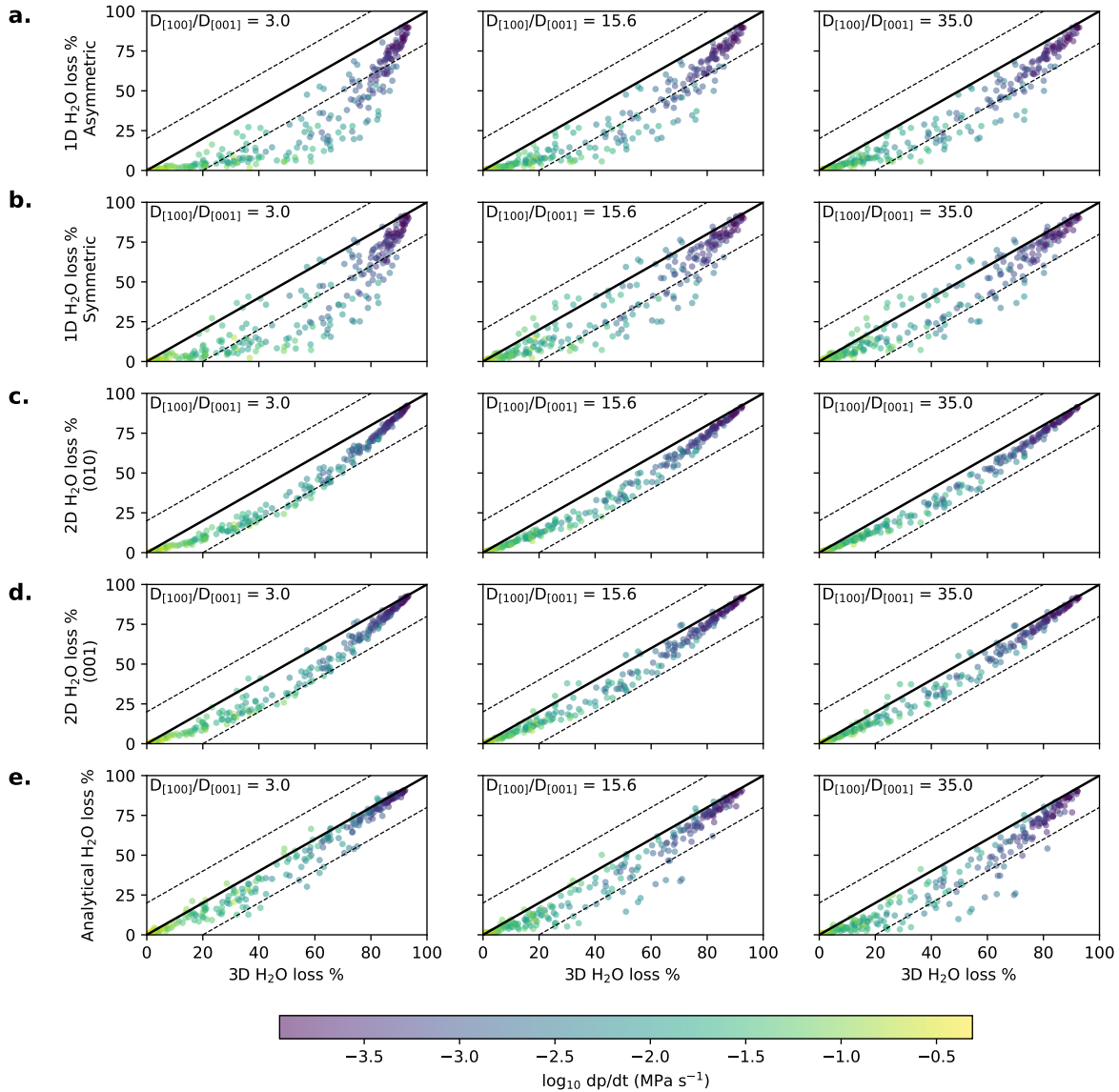
November 21, 2023, 6:44am
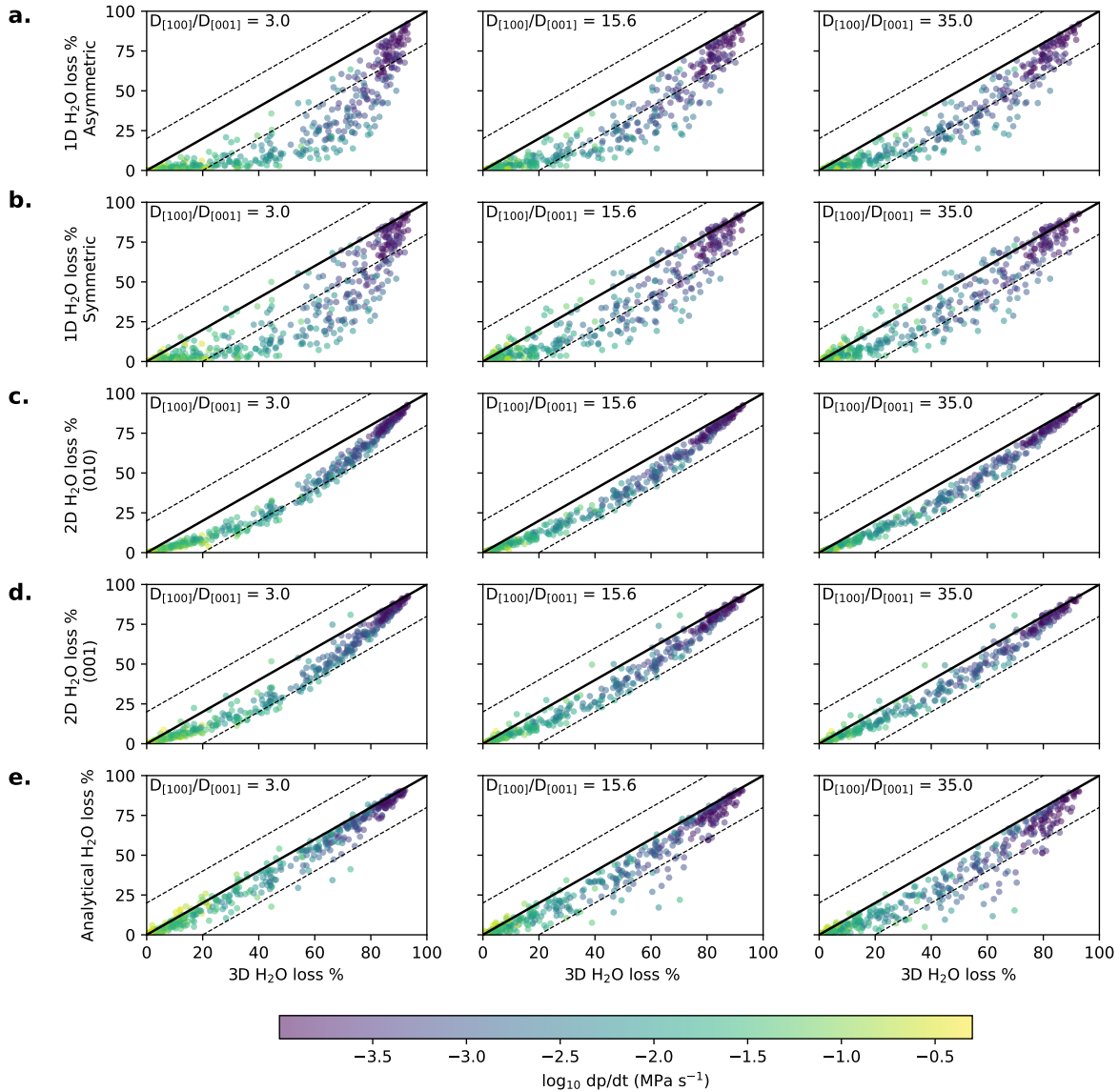
Figure S14. Results of the Monte Carlo modelling showing melt inclusion water loss for different model types and with different diffusive anisotropies ($D_{[100]}/D_{[001]}$) and using a partition coefficient of 0.000459. Comparisons are made between the 3D models and the 1D asymmetric models (a), 1D symmetric models (b), 2D models sectioned along (010) (c), 2D models sectioned along (001) (d), and the anisotropic analytical solution (e). Each column shows model results using different diffusive anisotropies ($D_{[100]}/D_{[001]}$). 1:1 lines are shown in black with $\pm$ 20 % envelopes shown with dashed lines. Points have been colour-coded based on $\log_{10}$ decompression rate of the 3D models.
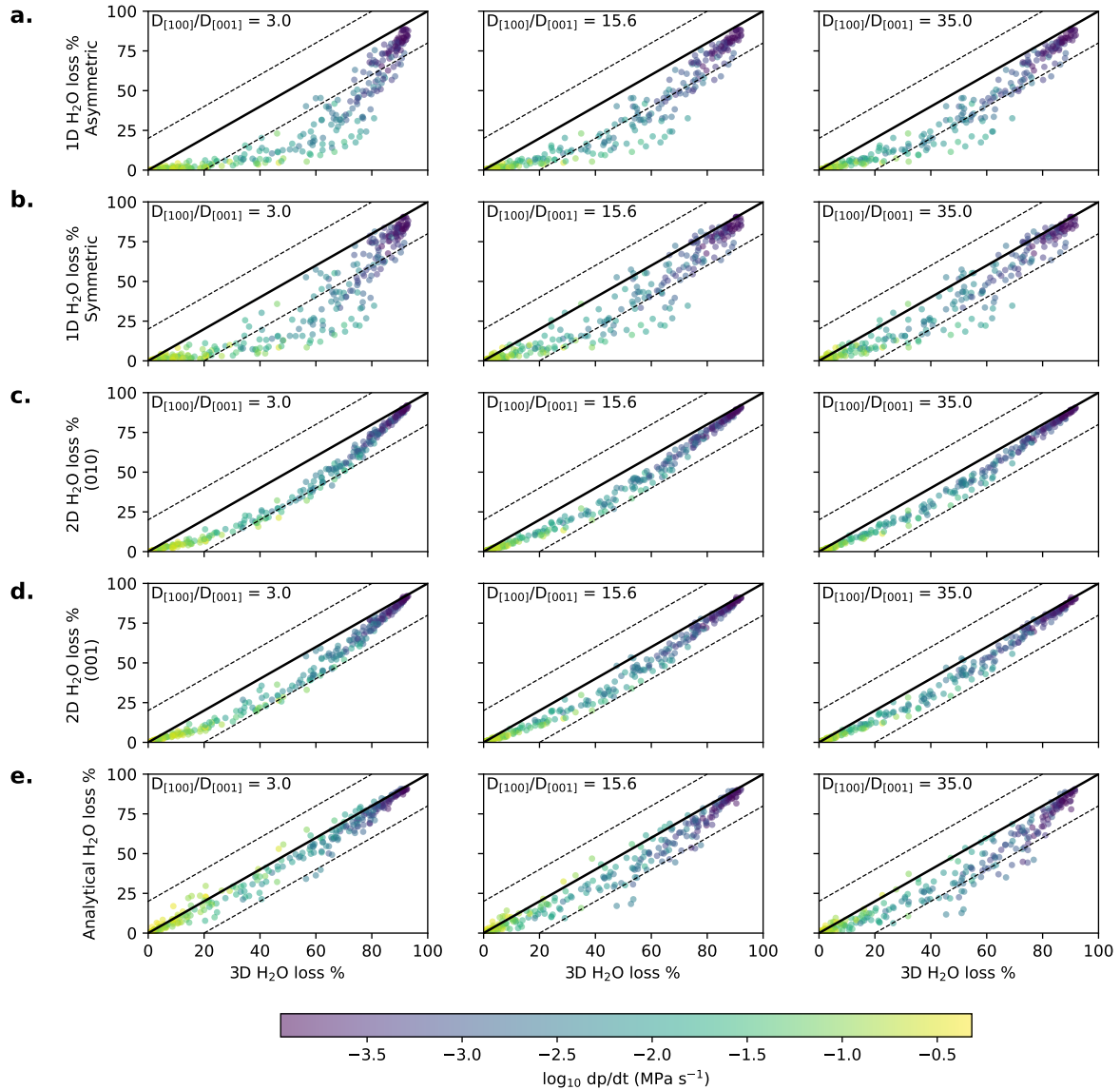
Figure S15. Results of the Monte Carlo modelling showing melt inclusion water loss for different model types and with different diffusive anisotropies ($D_{[100]}/D_{[001]}$) and using a partition coefficient of 0.000459. Comparisons are made between the 3D models and the 1D asymmetric models (a), 1D symmetric models (b), 2D models sectioned along (010) (c), 2D models sectioned along (001) (d), and the anisotropic analytical solution (e). Each column shows model results using different diffusive anisotropies ($D_{[100]}/D_{[001]}$). 1:1 lines are shown in black with $\pm$ 20 % envelopes shown with dashed lines. Points have been colour-coded based on $\log_{10}$ decompression rate of the 3D models.

Figure S16. Results of the Monte Carlo modelling showing melt inclusion water loss for different model types and with different diffusive anisotropies $(D_{[100]}/D_{[001]})$ and using random partition coefficients ranging from 0.0004 to 0.002. Comparisons are made between the 3D models and the 1D asymmetric models (a), 1D symmetric models (b), 2D models sectioned along (010) (c), 2D models sectioned along (001) (d), and the anisotropic analytical solution (e). Each column shows model results using different diffusive anisotropies $(D_{[100]}/D_{[001]})$. 1:1 lines are shown in black with $\pm$ 20 % envelopes shown with dashed lines. Points have been colour-coded based on $\log_{10}$ decompression rate of the 3D models.

November 21, 2023, 6:44am
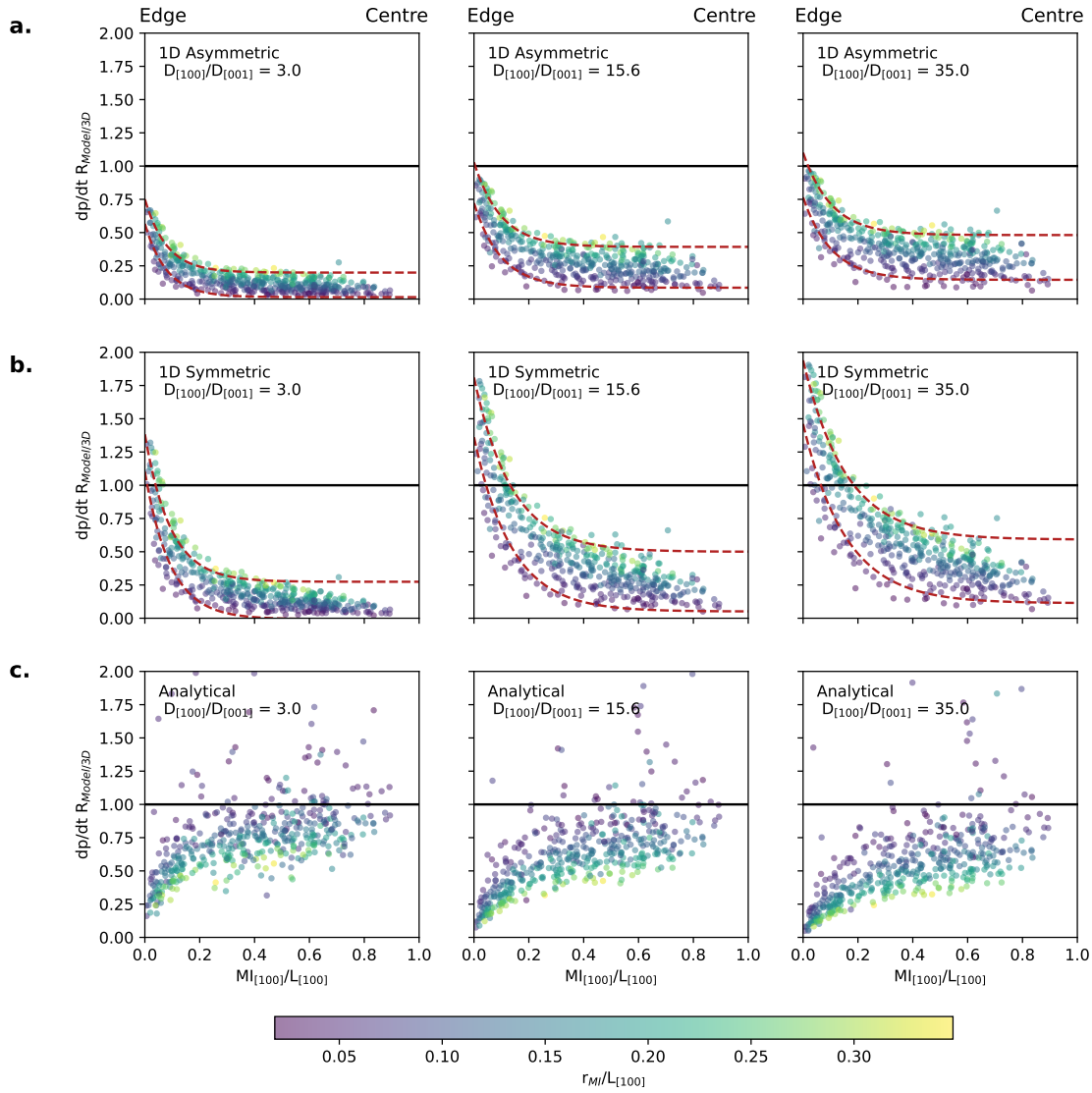
Figure S17. Geometrical controls on modelled decompression rates for models with a partition coefficient of 0.000459. $MI_{[100]}$ is the distance from the nearest crystal edge to the edge of the melt inclusion along the [100] axis. $L_{[100]}$ is the distance between the crystal edge and the centre of the crystal along [100]. Points have been coloured based on the size of the melt inclusion radius (r_{MI}) relative to $L_{[100]}$. The black line shows where 3D and 1D model inversions were equal (dp/dt $R_{1D/3D} = 1$). The red dashed lines show empirical model fits through the 1D model data. (a) shows results for 1D asymmetric models, (b) shows results for 1D symmetric models, and (c) shows results from the anisotropic analytical solution. Each column shows model results using different diffusive anisotropies ($D_{[100]}/D_{[001]}$).
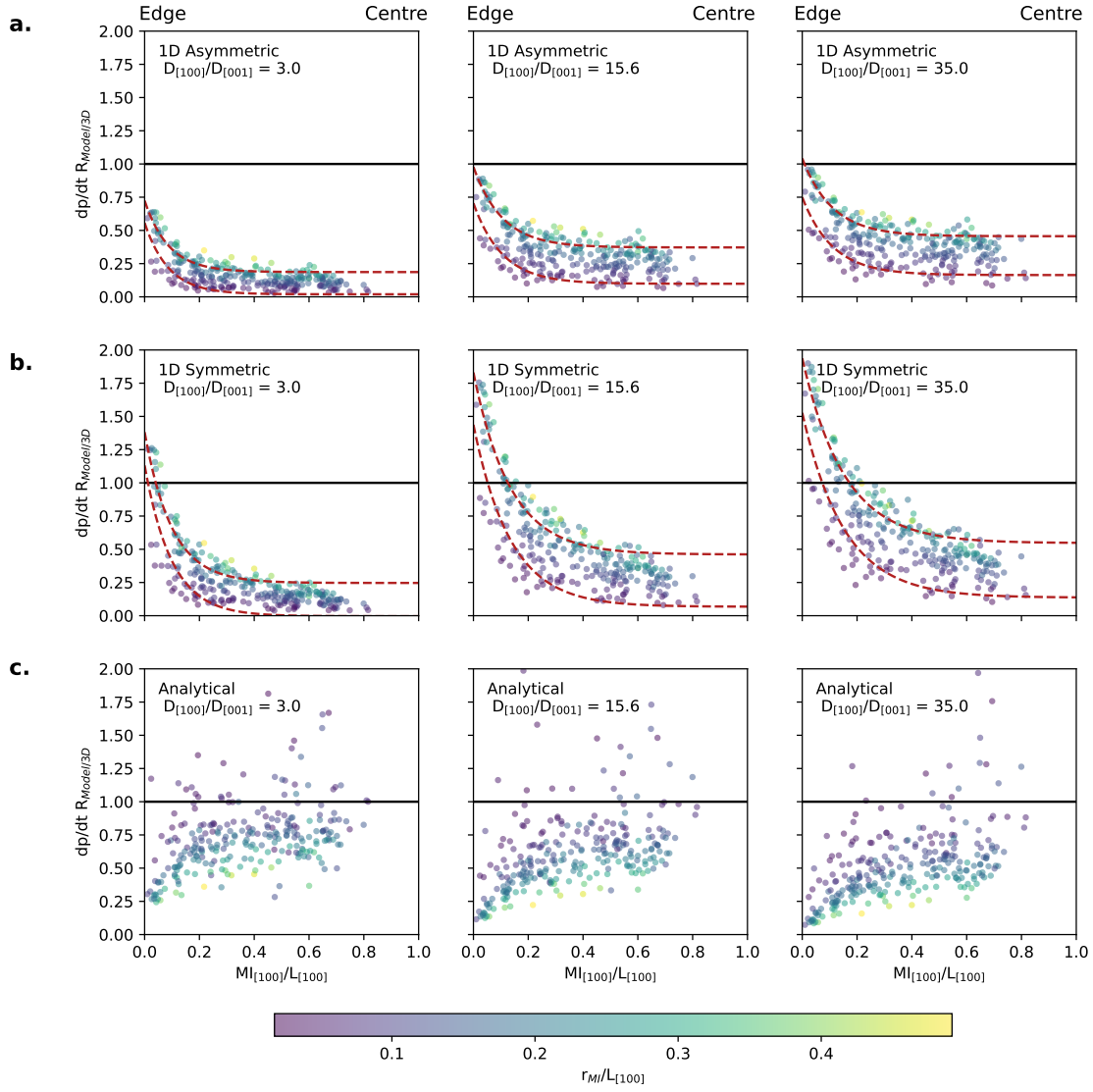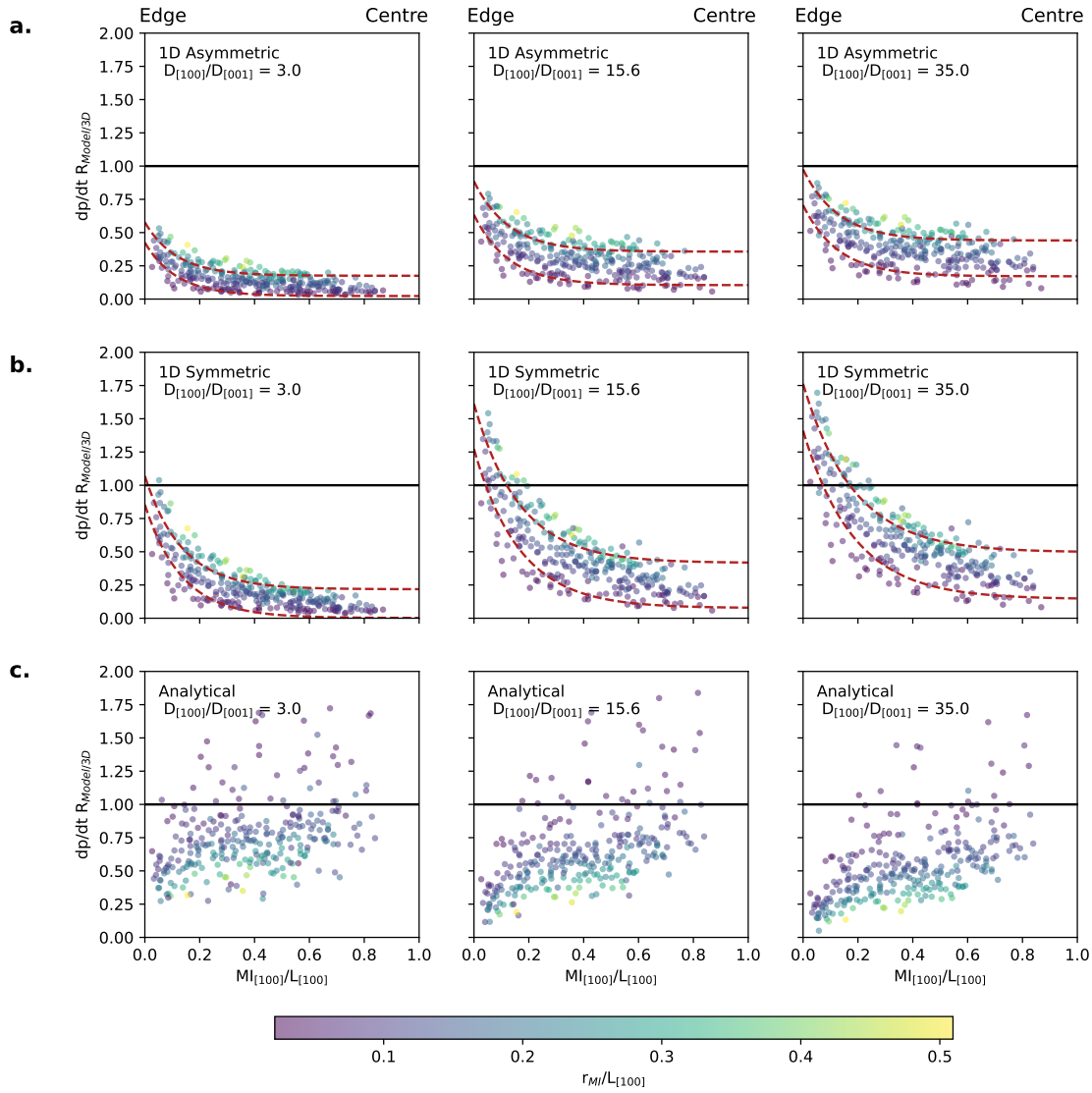
November 21, 2023, 6:44am

Figure S18. Geometrical controls on modelled decompression rates for models with a partition coefficient of 0.001. $MI_{[100]}$ is the distance from the nearest crystal edge to the edge of the melt inclusion along the [100] axis. $L_{[100]}$ is the distance between the crystal edge and the centre of the crystal along [100]. Points have been coloured based on the size of the melt inclusion radius (r_{MI}) relative to $L_{[100]}$. The black line shows where 3D and 1D model inversions were equal ($dp/dt\ R_{1D/3D} = 1$). The red dashed lines show empirical model fits through the 1D model data. (a) shows results for 1D asymmetric models, (b) shows results for 1D symmetric models, and (c) shows results from the anisotropic analytical solution. Each column shows model results using different diffusive anisotropies ($D_{[100]}/D_{[001]}$).
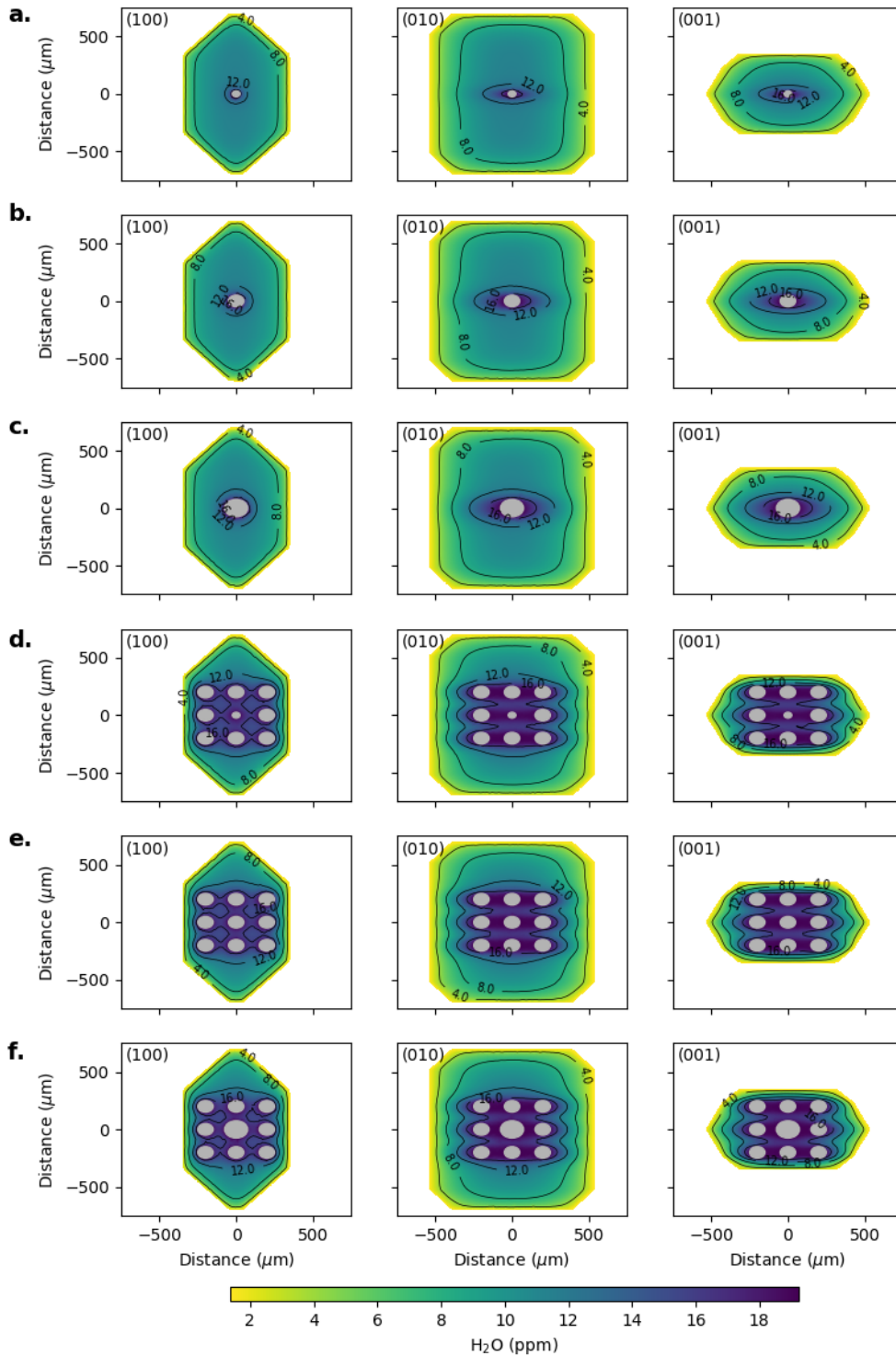
November 21, 2023, 6:44am

Figure S19. Geometrical controls on modelled decompression rates for models with a randomly selected partition coefficient between 0.0004 and 0.002. $MI_{[100]}$ is the distance from the nearest crystal edge to the edge of the melt inclusion along the [100] axis. $L_{[100]}$ is the distance between the crystal edge and the centre of the crystal along [100]. Points have been coloured based on the size of the melt inclusion radius (r_{MI}) relative to $L_{[100]}$. The black line shows where 3D and 1D model inversions were equal ($dp/dt\ R_{1D/3D} = 1$). The red dashed lines show empirical model fits through the 1D model data. (a) shows results for 1D asymmetric models, (b) shows results for 1D symmetric models, and (c) shows results from the anisotropic analytical solution. Each column shows model results using different diffusive anisotropies ($D_{[100]}/D_{[001]}$).

Figure S20. Sectioned 3D models that contain single and multiple melt inclusions (grey regions) for 0.1 MPa s^{-1} and anisotropy of 15.6. Single melt inclusion with 25 µm, 50 µm and 75 µm radius are shown in (a), (b) and (c). Multiple melt inclusions with a central melt inclusion with 25 µm, 50 µm and 75 µm radius are shown in (d), (e) and (f). The surrounding melt inclusions in these models have 50 µm radius.
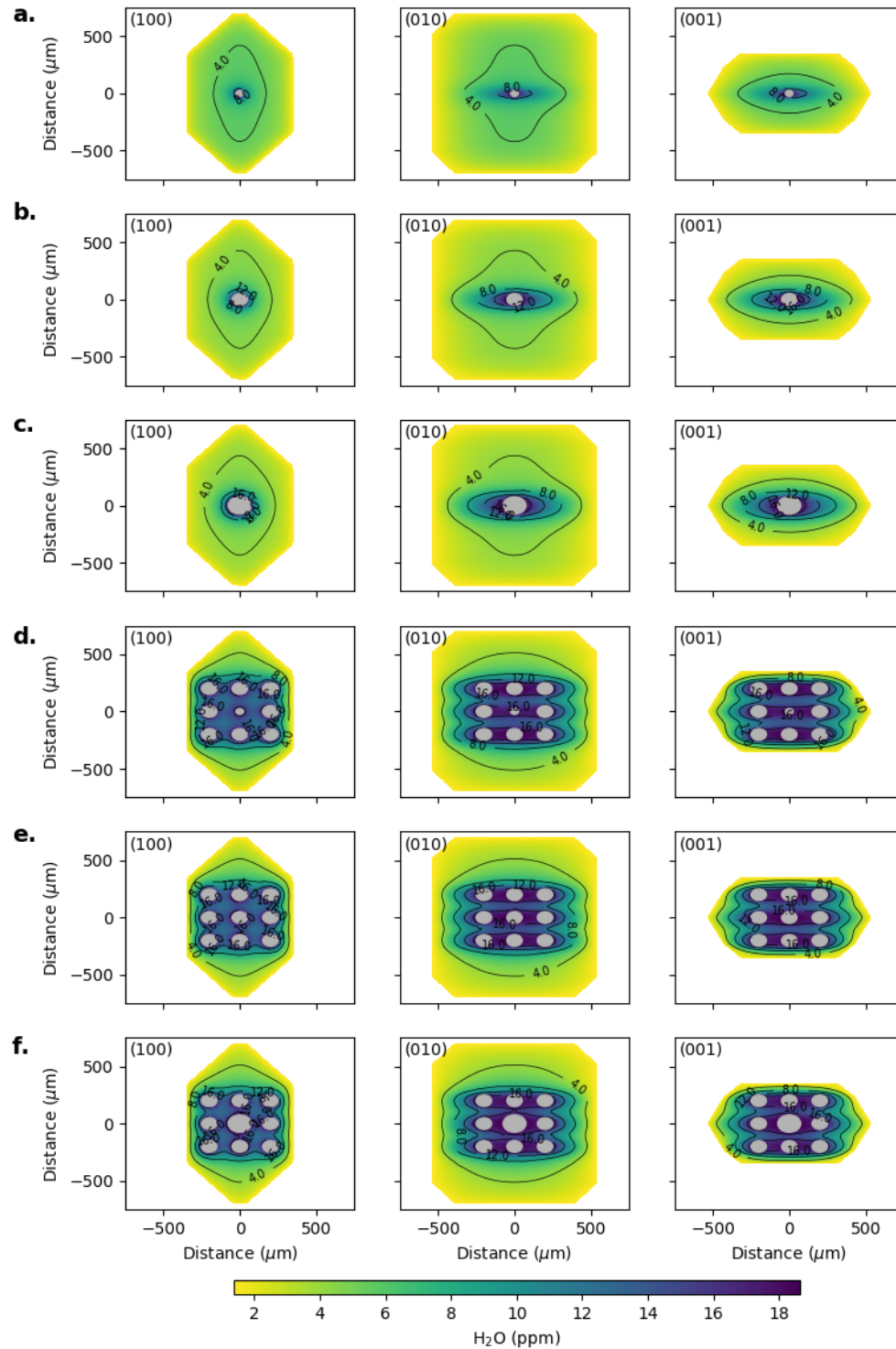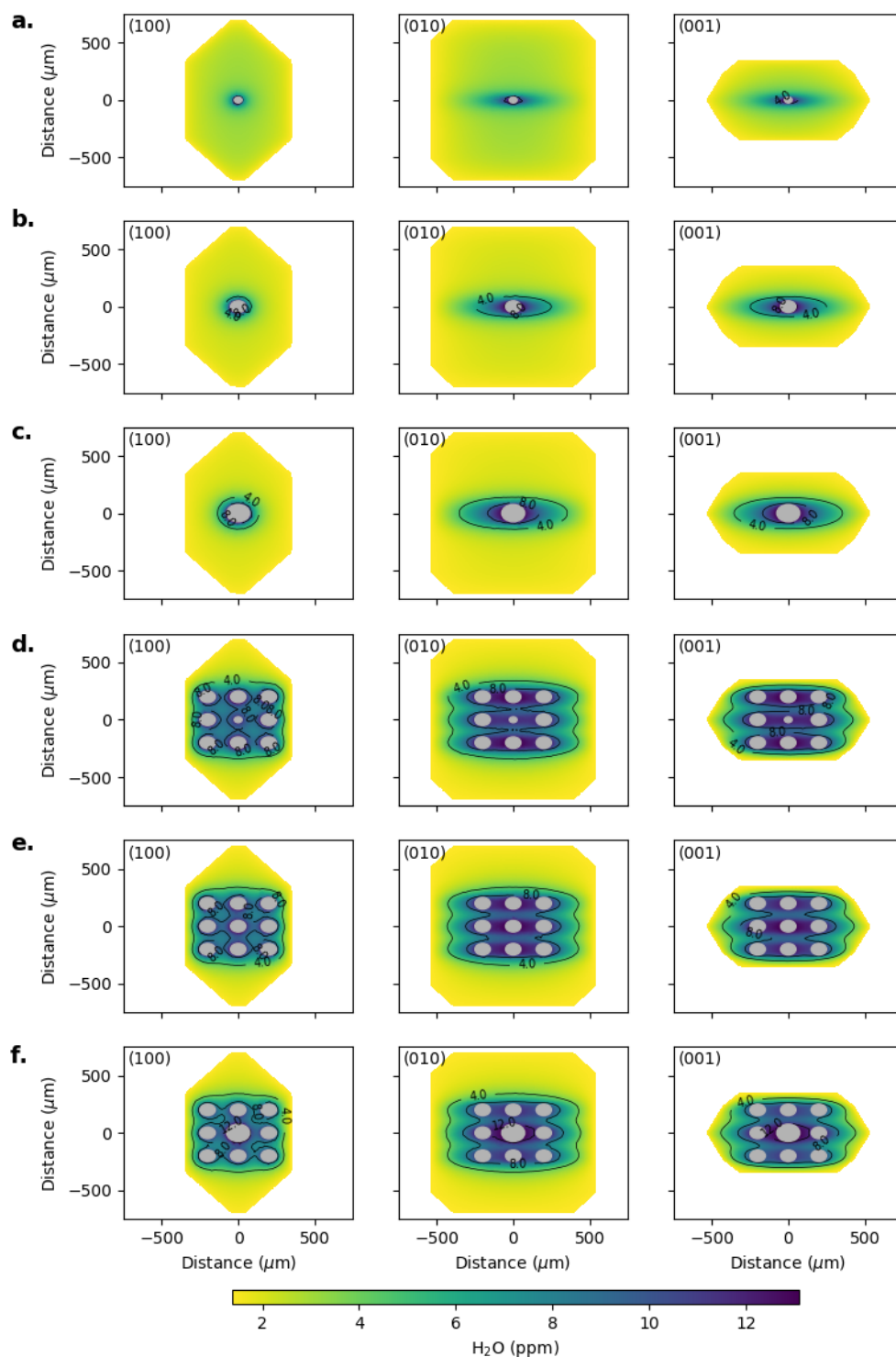
Figure S21. Sectioned 3D models that contain single and multiple melt inclusions (grey regions) for 0.01 MPa s^{-1} and anisotropy of 15.6. Single melt inclusion with 25 µm, 50 µm and 75 µm radius are shown in (a), (b) and (c). Multiple melt inclusions with a central melt inclusion with 25 µm, 50 µm and 75 µm radius are shown in (d), (e) and (f). The surrounding melt inclusions in these models have 50 µm radius.

Figure S22. Sectioned 3D models that contain single and multiple melt inclusions (grey regions) for $0.001\,\text{MPa s}^{-1}$ and anisotropy of 15.6. Single melt inclusion with $25\,\mu\text{m}$, $50\,\mu\text{m}$ and $75\,\mu\text{m}$ radius are shown in (a), (b) and (c). Multiple melt inclusions with a central melt inclusion with $25\,\mu\text{m}$, $50\,\mu\text{m}$ and $75\,\mu\text{m}$ radius are shown in (d), (e) and (f). The surrounding melt inclusions in these models have $50\,\mu\text{m}$ radius.
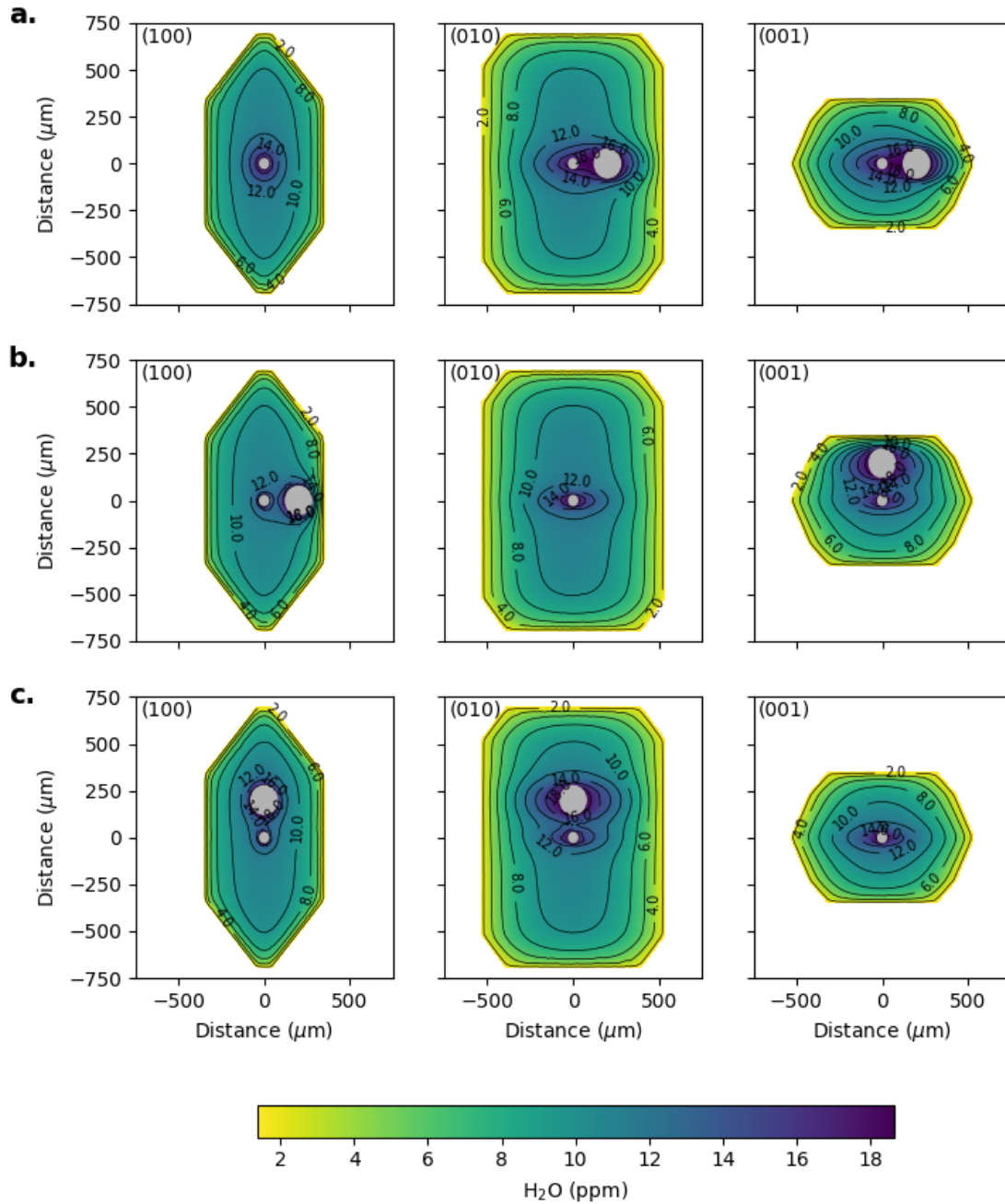
Figure S23. Model configurations of 3D models in which there are 2 melt inclusions: a 25 µm radius central inclusion and a 75 µm radius inclusion situated along one of the crystallographic axes. The large melt inclusion was placed along the [100] axis (a), the [010] axis (b), and the [001] axis (c) 250 µm from the central inclusion. All melt inclusions are represented by grey regions. Each column shows a 2D section through a 3D model. Results of models for a decompression rate of 0.1 MPa s^{-1} and a diffusive anisotropy of 15.6 are shown.
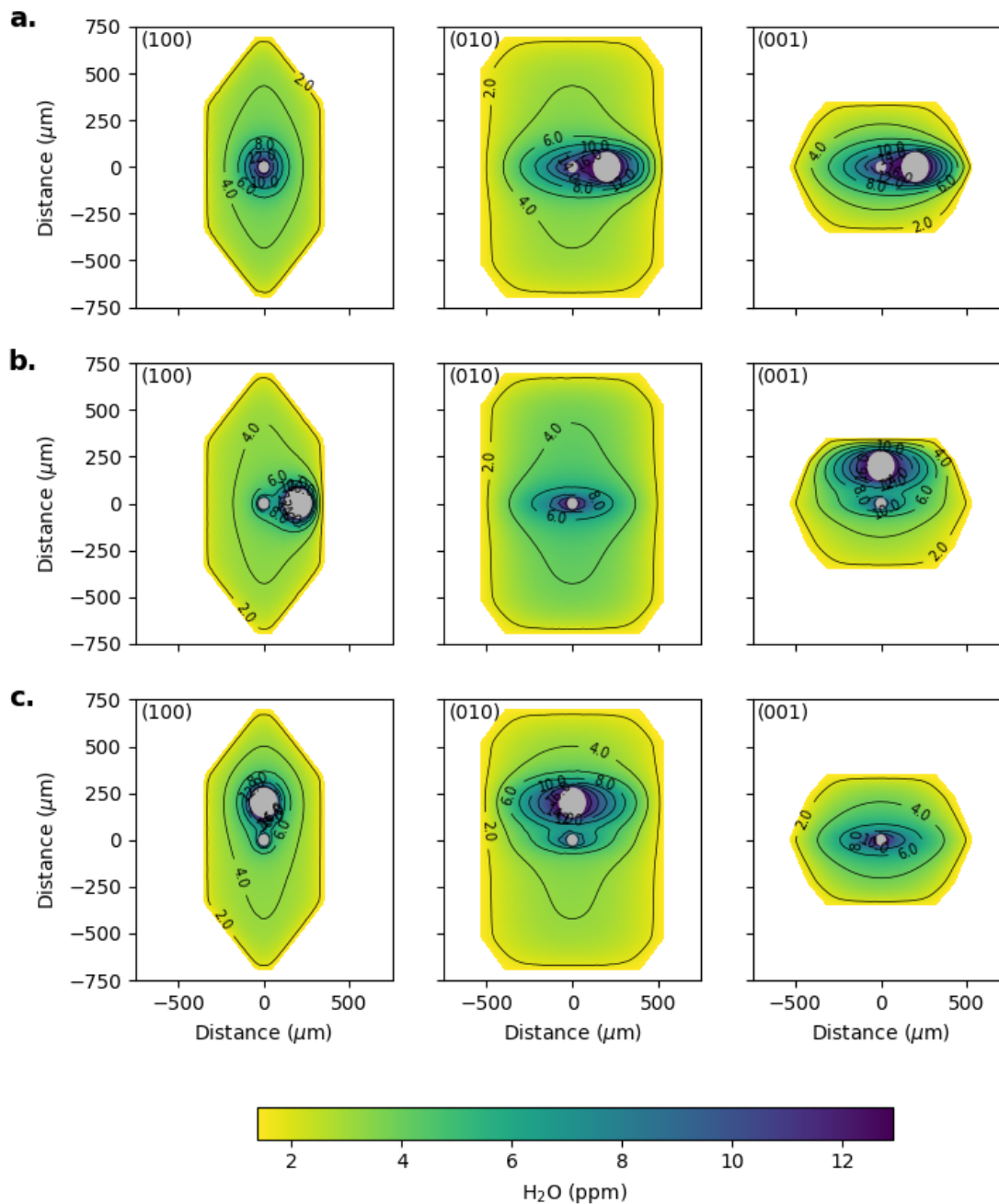
Figure S24. Model configurations of 3D models in which there are 2 melt inclusions: a 25 μm radius central inclusion and a 75 μm radius inclusion situated along one of the crystallographic axes. The large melt inclusion was placed along the [100] axis (a), the [010] axis (b), and the [001] axis (c) 250 μm from the central inclusion. All melt inclusions are represented by grey regions. Each column shows a 2D section through a 3D model. Results of models for a decompression rate of 0.01 MPa s^{-1} and a diffusive anisotropy of 15.6 are shown.
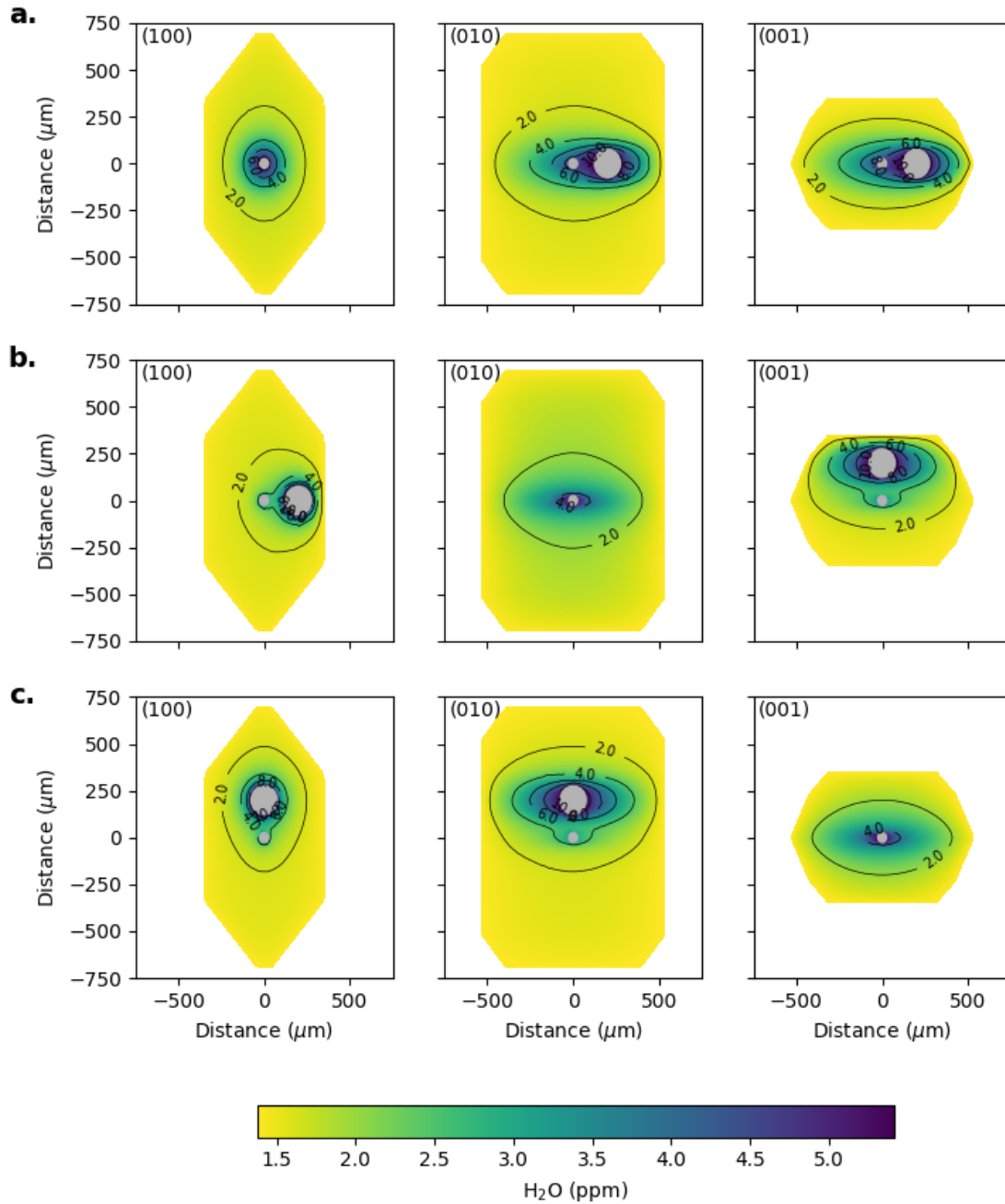
Figure S25. Model configurations of 3D models in which there are 2 melt inclusions: a 25 μm radius central inclusion and a 75 μm radius inclusion situated along one of the crystallographic axes. The large melt inclusion was placed along the [100] axis (a), the [010] axis (b), and the [001] axis (c) 250 μm from the central inclusion. All melt inclusions are represented by grey regions. Each column shows a 2D section through a 3D model. Results of models for a decompression rate of 0.001 MPa s^{-1} and a diffusive anisotropy of 15.6 are shown.